

2013

Fundamental Characterization Studies of Advanced Photocatalytic Materials

Somphonh Peter Phivilay
Lehigh University

Follow this and additional works at: <http://preserve.lehigh.edu/etd>

Recommended Citation

Phivilay, Somphonh Peter, "Fundamental Characterization Studies of Advanced Photocatalytic Materials" (2013). *Theses and Dissertations*. Paper 1204.

This Dissertation is brought to you for free and open access by Lehigh Preserve. It has been accepted for inclusion in Theses and Dissertations by an authorized administrator of Lehigh Preserve. For more information, please contact preserve@lehigh.edu.

Fundamental Characterization Studies of Advanced Photocatalytic Materials

by

Somphonh Peter Phivilay

A Dissertation
Presented to the Graduate and Research Committee
of Lehigh University
in Candidacy for the Degree of
Doctor of Philosophy

in

Chemical Engineering

Lehigh University

January 2013

Copyright © 2013 by Somphonh Peter Phivilay

CERTIFICATE OF APPROVAL

Approved and recommended for acceptance as a dissertation in partial fulfillment of the requirements for the degree of Doctor of Philosophy.

Date

Accepted Date

Dissertation Advisor:

Dr. Israel E. Wachs
Lehigh University

Committee Members:

Dr. Christopher J. Kiely
Lehigh University

Dr. Bruce E. Koel
Princeton University

Dr. Mark A. Snyder
Lehigh University

Acknowledgements

I would like to give special thanks to my advisor Professor Israel Wachs for giving me the opportunity to join his lab group and for his guidance throughout my years in graduate school. His passionate attitude and knowledge about his research field was inspirational and has opened my eyes to how research needs to be approached and conducted. I am very fortunate and thankful that he gave me the special chance to go travel to Japan since my dissertation would not have been possible without that collaborative work and living in a different country was an experience I will never forget.

I would like to thank all the members in my lab group for their help and support throughout the years: Liz Ross, Kamalakanta Routray, Chip Roberts, Kevin Doura, Julie Molinari, Chris Keterakis, Jih Mirn Jehng, Mike Ford, Soe Lwin, Yadan Tang and Mingui Zhu.

This dissertation wouldn't have been possible without the help from my collaborators. I would like to thank Prof. Domen and his lab group for letting me work in their lab and helping me to learn about photocatalysis research. I would like to thank Alexander Puretsky at Oak Ridge National Laboratory for help in obtaining photoluminescence spectroscopy data along with Chip Roberts. I would like to thank Al Miller and Rob Pafchek at Lehigh University for help in obtaining HR-XPS and HS-LEISS data.

Most of all I would like to thank my friends and family for their loving support, always encouraging and motivating me to do my best. Without my parents and the rest of my family, I would not have accomplished as much as I have in my life. This work is dedicated to them and I am thankful for everything that they have given me.

TABLE OF CONTENTS

ACKNOWLEDGEMENTS	iv
TABLE OF CONTENTS	vi
LIST OF TABLES	xi
LIST OF FIGURES	xiii
ABSTRACT	1
CHAPTER 1	3
Overview of Heterogeneous Photocatalyst Literature for Water Splitting	
1.1. Introduction	3
1.2. Basic Principle of Photocatalytic Water Splitting	5
1.3. Semiconductor Materials for Photocatalytic Water Splitting	7
1.4. Overview of Characterization Techniques Utilized for Heterogeneous Mixed Oxide Photocatalyst Systems for Water Splitting	14
1.4.1 X-ray Diffraction (XRD)	15
1.4.2 X-ray Absorption Spectroscopy (XANES and EXAFS)	16
1.4.3 Electron Microscopy	17
1.4.4 Infrared (IR) spectroscopy	19
1.5 Approach and Outline of This Thesis	20
1.5.1 Raman Spectroscopy	21
1.5.2 Ultraviolet-visible (UV-vis) Diffuse Reflectance Spectroscopy (DRS)	22
1.5.3 Photoluminescence (PL) Spectroscopy	23
1.5.4 High-Resolution X-ray Photoemission Spectroscopy (HR-XPS)	24
1.5.5 High Sensitivity Low Energy Ion Scattering Spectroscopy (HS-LEISS)	25
1.5.6 Photocatalytic Reactor for Water Splitting	27
1.5.7 Dissertation Outline	27
References	29
Figures	43
CHAPTER 2	46
Nature of Catalytic Active Sites Present on the Surface of Advanced Bulk Tantalum Mixed Oxide Photocatalysts	

Abstract	46
2.1 Introduction	47
2.2. Experimental	50
2.2.1 Photocatalyst Synthesis	50
2.2.2 <i>In Situ</i> Raman Spectroscopy	51
2.2.3 <i>In Situ</i> UV-Vis Diffuse Reflectance Spectroscopy	51
2.2.4 Photoluminescence Spectroscopy and Lifetime Emissions Decay	52
2.2.5 High Resolution X-ray Photoelectron Spectroscopy (HR-XPS)	54
2.2.6 High Sensitivity Low Energy Ion Scattering (HS-LEIS) Spectroscopy	54
2.3 Results	55
2.3.1 In Situ Raman Spectroscopy	55
2.3.2 UV-Vis Diffuse Reflectance Spectroscopy	56
2.3.3 Photoluminescence Spectroscopy and PL lifetime decay	56
2.3.4 High Resolution X-ray Photoelectron Spectroscopy	58
2.3.5 High Sensitivity-Low Energy Ion Scattering Spectroscopy	58
2.4 Discussion	60
2.4.1 Bulk Molecular and Electronic Structures of NaTaO ₃ Photocatalysts	60
2.4.2 Surface Composition of Promoted NaTaO ₃ Photocatalyst	60
2.4.3 Bulk and Surface Structures of the Promoted NaTaO ₃ :La Photocatalyst	62
2.4.4 Generation of Excited Electron/Hole Pairs and Their Lifetimes	62
2.4.5 Structure-Activity Relationships for Splitting of H ₂ O by NaTaO ₃ Photocatalysts	64
2.5 Conclusions	65
Acknowledgements	66
References	67
Tables	72
Figures	76

CHAPTER 3 83

Fundamental Bulk/Surface Structure – Photoactivity Relationships of Supported (Rh_{2-y}Cr_yO₃)/GaN Photocatalysts

Abstract	83
3.1 Introduction	84
3.2. Experimental	85

3.2.1 Catalyst Synthesis	85
3.2.2 Raman Spectroscopy	86
3.2.3 UV-Vis NIR Diffuse Reflectance Spectroscopy (DRS)	86
3.2.4 Photoluminescence Spectroscopy and Photoluminescent Decay	87
3.2.5 High Resolution X-ray Photoelectron Spectroscopy (HR-XPS)	88
3.2.6 High Sensitivity Low Energy Ion Scattering (HS-LEIS) Spectroscopy	89
3.3 Results and Discussion	89
3.3.1 Bulk Characteristics of GaN Photocatalysts	90
3.3.1.1 Bulk Molecular Structure	90
3.3.1.2 Bulk Electronic Structure	90
3.3.2 Surface Composition of GaN photocatalysts	91
3.3.2.1 Atomic Composition and Chemical State of the Surface Region (~1-3 nm)	91
3.3.2.2 Outermost Atomic Layer Composition (~0.3 nm)	91
3.3.3 Electron/Hole Generation and Recombination	93
3.3.4 Bulk/Surface – Photoactivity Relationships of GaN Photocatalysts	95
3.4 Conclusions	96
Acknowledgements	96
References	98
Tables	104
Figures	106
CHAPTER 4	116
Nature of Catalytic Active Surface Sites Present on Bulk (Ga_{1-x}Zn_x)(N_{1-x}O_x) Photocatalysts	
Abstract	116
4.1 Introduction	117
4.2. Experimental	121
4.2.1 Catalyst Synthesis	121
4.2.2 Raman Spectroscopy	122
4.2.3 UV-Vis NIR Diffuse Reflectance Spectroscopy (DRS)	123
4.2.4 High Resolution X-ray Photoelectron (HR-XPS) Spectroscopy	124
4.2.5 High Sensitivity Low Energy Ion Scattering (HS-LEISS) Spectroscopy	124
4.2.6 Photoluminescence Spectroscopy and Photoluminescent Decay	125

4.2.7 Photocatalytic Water Splitting	126
4.3 Results	127
4.3.1 Bulk Molecular Structures	127
4.3.2 Bulk Electronic Structures	128
4.3.3 Atomic Composition of Surface Region (~1-3nm)	129
4.3.4 Atomic Composition of Outermost Surface Layer (~0.3nm)	131
4.3.5 Dynamics of Photoexcited Electrons and Holes	134
4.3.6 Photocatalytic Water Splitting	136
4.4 Discussion	136
4.4.1 Bulk and Electronic Structures of the $(\text{Ga}_{1-x}\text{Zn}_x)(\text{N}_{1-x}\text{O}_x)$ Oxynitride Support	137
4.4.2 Atomic Distribution of the Surface Region of Supported $(\text{Ga}_{1-x}\text{Zn}_x)(\text{N}_{1-x}\text{O}_x)$ Photocatalysts	137
4.4.2.1 Model of the Supported $(\text{Rh}_{2-y}\text{Cr}_y\text{O}_3)/(\text{Ga}_{1-x}\text{Zn}_x)(\text{N}_{1-x}\text{O}_x)$ Mixed Oxide Photocatalyst	137
4.4.2.2 Model of the Supported $(\text{Rh}/\text{Cr}_2\text{O}_3)/(\text{Ga}_{1-x}\text{Zn}_x)(\text{N}_{1-x}\text{O}_x)$ Core/Shell Photocatalyst	139
4.4.3 Generation of Excited Electron/Hole Pairs and Their Lifetimes	140
4.4.4 Structure-Photoactivity Relationships for Splitting of H_2O by $(\text{Ga}_{1-x}\text{Zn}_x)(\text{N}_{1-x}\text{O}_x)$ Photocatalysts	142
4.4.4.1 Supported $(\text{Rh}_{2-y}\text{Cr}_y\text{O}_3)/(\text{Ga}_{1-x}\text{Zn}_x)(\text{N}_{1-x}\text{O}_x)$ Photocatalyst	142
4.4.4.2 Supported $(\text{Rh}/\text{Cr}_2\text{O}_3)/(\text{Ga}_{1-x}\text{Zn}_x)(\text{N}_{1-x}\text{O}_x)$ Core/Shell Photocatalyst	143
4.5 Conclusions	144
Acknowledgements	145
References	146
Tables	153
Figures	157
CHAPTER 5	177
Investigating the Surface Nature of TaON Photocatalysts	
Abstract	177
5.1 Introduction	178
5.2. Experimental	179
5.2.1 Catalyst Synthesis	180
5.2.2 Raman Spectroscopy	180
5.2.3 UV-Vis NIR Diffuse Reflectance Spectroscopy (DRS)	180
5.2.4 High Sensitivity-Low Energy Ion Scattering (HS-LEISS) Spectroscopy	181

5.2.5 High Resolution X-ray Photoelectron (HR-XPS) Spectroscopy	182
5.3 Results and Discussion	182
5.3.1 Bulk Characteristics of TaON Photocatalysts	182
5.3.1.1 Bulk Molecular Structure	182
5.3.1.2 Bulk Electronic Structure	183
5.3.2 Surface Atomic Composition of TaON photocatalysts	184
5.3.2.1 Outermost Surface Layer (~0.3 nm)	184
5.3.2.2 Surface Region (~1-3 nm)	185
5.3.2.3 Surface Nature of TaON Photocatalysts	186
5.3.3 Structure-Photoactivity Relationships	187
5.4 Conclusions	188
Acknowledgements	188
References	189
Tables	195
Figures	197
CHAPTER 6	205
Conclusions and Future Studies	
6.1 Conclusions	205
6.2 Future Studies	208

LIST OF TABLES

Chapter 2

Table 2.1: Edge Energy Values from UV-Vis DRS.	72
Table 2.2: Photoluminescence decay fit parameters for catalysts at 267 nm excitation.	73
Table 2.3: XPS surface region atomic concentration of promoted 0.2%NiO/NaTaO ₃ :2%La photocatalyst.	74
Table 2.4: Photoactivity of Tantalum Oxide Photocatalysts for Water Splitting with UV Excitation (>270 nm).	75

Chapter 3

Table 3.1: Eg values from UV-vis DRS, and peak emission wavelengths from PL spectroscopy of the GaN photocatalysts at 400 nm excitation.	104
Table 3.2: HR-XPS surface region atomic composition (~1-3nm) of GaN photocatalysts.	105

Chapter 4

Table 4.1: Eg values, peak emission wavelengths, and decay fit parameters of the catalysts at 400 nm excitation. The decay parameters displayed are those found in the PL spectra taken in the emission range of the peak value.	153
Table 4.2: XPS surface region atomic composition (~1-3nm) of (Ga _{1-x} Zn _x)(N _{1-x} O _x).	154
Table 4.3: XPS surface region atomic composition (~1-3nm) of fresh and used (Rh _{2-y} Cr _y O ₃)/(Ga _{1-x} Zn _x)(N _{1-x} O _x) mixed oxide photocatalysts.	155
Table 4.4: HR-XPS surface region atomic composition (~1-3nm) of fresh and used (Rh/Cr ₂ O ₃)/(Ga _{1-x} Zn _x)(N _{1-x} O _x) core/shell photocatalysts.	156

Chapter 5

Table 5.1: Uv-vis DRS Edge Energy Values for Tantalum-based Photocatalysts.	195
--	-----

Table 5.2: HR-XPS Surface Region Atomic Composition of TaON Photocatalysts.

196

LIST OF FIGURES

Chapter 1

Figure 1.1: Basic Principles of Photocatalytic Water Splitting. 43

Figure 1.2: Schematic Energy Diagram of photocatalytic water-splitting systems: (a) conventional one-step system and (b) two-step “Z-Scheme” system. 44

Figure 1.3: Schematic of Photocatalytic Reactor Designs. 45

Chapter 2

Figure 2.1: Raman Spectra of Tantalum-based Photocatalysts. 76

Figure 2.2: Photoluminescence Spectra at 267 nm Excitation for Tantalum-based Photocatalysts. 77

Figure 2.3: Photoluminescence Emissions Decay Curves for Tantalum-based Photocatalysts. 78

Figure 2.4: XPS survey spectrum of surface region for 0.2%NiO/NaTaO₃:2%La promoted photocatalyst. 79

Figure 2.5: HS-LEIS spectra for 0.2%NiO/NaTaO₃:2%La promoted photocatalyst using (a) He⁺ ion gas and (b) Ne⁺ ion gas. 80

Figure 2.6: HS-LEIS Depth Profile for 0.2%NiO/NaTaO₃:2%La promoted photocatalyst using (a) He⁺ ion gas and (b) Ne⁺ ion gas. 81

Figure 2.7: Schematic Diagram of the Bulk and Surface of the Promoted 0.2%NiO/NaTaO₃:2%La Photocatalyst. 82

Chapter 3

Figure 3.1: Raman spectra for GaN photocatalysts (532 nm). 106

Figure 3.2: XPS survey spectra of (a) GaN and (b) supported (Rh_{2-y}Cr_yO₃)/GaN photocatalysts. 107

Figure 3.3: HR-XPS spectra of (a) Cr 2p and (b) Rh 3d regions of the supported (Rh/Cr ₂ O ₃)/GaN photocatalyst.	108
Figure 3.4: HS-LEIS Depth Profile for GaN photocatalyst using He ⁺ ion gas.	109
Figure 3.5: HS-LEIS spectra of untreated and atomic O treated supported (Rh _{2-y} Cr _y O ₃)/GaN photocatalyst.	110
Figure 3.6: HS-LEIS depth profile for the supported (Rh _{2-y} Cr _y O ₃)/GaN photocatalyst using (a) He ⁺ ion gas and (b) Ne ⁺ ion gas.	111
Figure 3.7: HS-LEIS Depth Profile of Cr and Rh for supported (Rh _{2-y} Cr _y O ₃)/GaN photocatalyst using Ne ⁺ ion gas.	112
Figure 3.8: PL emissions spectra for GaN photocatalysts (400 nm excitation).	113
Figure 3.9: PL lifetimes spectra for (a) GaN and (b) (Rh _{2-y} Cr _y O ₃)/GaN photocatalysts at different emissions wavelengths (400 nm excitation).	114
Figure 3.10: Schematic of (Rh _{2-y} Cr _y O ₃)/GaN photocatalysts.	115
 Chapter 4	
Figure 4.1: Raman Spectra of β-Ga ₂ O ₃ and ZnO precursors (532 nm) under ambient conditions.	157
Figure 4.2: Raman Spectra of (Ga _{1-x} Zn _x)(N _{1-x} O _x) and (Rh _{2-y} Cr _y O ₃)/(Ga _{1-x} Zn _x)(N _{1-x} O _x) (432 nm) under ambient conditions.	158
Figure 4.3: XPS Survey spectra of (a) fresh and (b) used (Rh _{2-y} Cr _y O ₃)/(Ga _{1-x} Zn _x)(N _{1-x} O _x) photocatalysts.	159
Figure 4.4: HR-XPS spectra of Cr 2p and Rh 3d regions of (a) fresh and (b) used supported (Rh _{2-y} Cr _y O ₃)/(Ga _{1-x} Zn _x)(N _{1-x} O _x) mixed oxide photocatalysts.	160
Figure 4.5: HR-XPS spectra of Cr 2p and Rh 3d regions of (a) fresh and (b) used (Rh/Cr ₂ O ₃)/(Ga _{1-x} Zn _x)(N _{1-x} O _x) photocatalysts.	161
Figure 4.6: HS-LEIS spectra for (Ga _{1-x} Zn _x)(N _{1-x} O _x) photocatalyst using (a) He ⁺ ion gas and (b) Ne ⁺ ion gas.	162

Figure 4.7: HS-LEIS Depth Profile for the fresh $(\text{Rh}_{2-y}\text{Cr}_y\text{O}_3)/(\text{Ga}_{1-x}\text{Zn}_x)(\text{N}_{1-x}\text{O}_x)$ photocatalyst using (a) He^+ ion gas and (b) Ne^+ ion gas.	163
Figure 4.8: HS-LEIS depth profile intensity ratios of elements/oxygen for the fresh $(\text{Rh}_{2-y}\text{Cr}_y\text{O}_3)/(\text{Ga}_{1-x}\text{Zn}_x)(\text{N}_{1-x}\text{O}_x)$ photocatalyst using He^+ ion gas.	164
Figure 4.9: HS-LEIS Depth Profile of Cr and Rh for the fresh $(\text{Rh}_{2-y}\text{Cr}_y\text{O}_3)/(\text{Ga}_{1-x}\text{Zn}_x)(\text{N}_{1-x}\text{O}_x)$ photocatalyst using Ne^+ ion gas.	165
Figure 4.10: HS-LEIS Depth Profile for the used supported $(\text{Rh}_{2-y}\text{Cr}_y\text{O}_3)/(\text{Ga}_{1-x}\text{Zn}_x)(\text{N}_{1-x}\text{O}_x)$ photocatalyst using (a) He^+ ion gas and (b) Ne^+ ion gas.	166
Figure 4.11: HS-LEIS Depth Profile of Cr and Rh for used supported $(\text{Rh}_{2-y}\text{Cr}_y\text{O}_3)/(\text{Ga}_{1-x}\text{Zn}_x)(\text{N}_{1-x}\text{O}_x)$ photocatalyst using Ne^+ ion gas.	167
Figure 4.12: HS-LEIS Depth Profile for the fresh supported $(\text{Rh}/\text{Cr}_2\text{O}_3)/(\text{Ga}_{1-x}\text{Zn}_x)(\text{N}_{1-x}\text{O}_x)$ core/shell photocatalyst using (a) He^+ ion gas and (b) Ne^+ ion gas.	168
Figure 4.13: HS-LEIS Depth Profiles of Cr and Rh for the fresh supported $(\text{Rh}/\text{Cr}_2\text{O}_3)/(\text{Ga}_{1-x}\text{Zn}_x)(\text{N}_{1-x}\text{O}_x)$ core/shell photocatalyst using Ne^+ ion gas.	169
Figure 4.14: HS-LEIS Depth Profile for the used supported $(\text{Rh}/\text{Cr}_2\text{O}_3)/(\text{Ga}_{1-x}\text{Zn}_x)(\text{N}_{1-x}\text{O}_x)$ core/shell photocatalyst using (a) He^+ ion gas and (b) Ne^+ ion gas.	170
Figure 4.15: HS-LEIS Depth Profiles for Cr and Rh for the used supported $(\text{Rh}/\text{Cr}_2\text{O}_3)/(\text{Ga}_{1-x}\text{Zn}_x)(\text{N}_{1-x}\text{O}_x)$ core/shell photocatalyst using Ne^+ ion gas.	171
Figure 4.16: PL spectra of bulk $\beta\text{-Ga}_2\text{O}_3$, ZnO and oxynitride catalysts at 400 nm excitation.	172
Figure 4.17: PL decay curves for the photocatalysts.	173
Figure 4.18: Comparison of Photocatalytic Water Splitting Activity ($\lambda > 400$ nm).	174
Figure 4.19: Schematic Model of Rh-Cr NPs for Co-Impregnation Synthesis Method.	175
Figure 4.20: Schematic Model of Rh-Cr NPs for Photodeposition Synthesis Method.	176

Chapter 5

Figure 5.1: Raman Spectra of Tantalum-based Photocatalysts (532 nm).	197
Figure 5.2: HS-LEIS Depth Profile of the Bulk TaON Photocatalyst.	198
Figure 5.3: HS-LEIS spectra of Bulk TaON Photocatalyst Before and After Atomic O Pretreatment.	199
Figure 5.4: HS-LEIS Depth Profile of the Supported RuO ₂ /TaON Photocatalyst.	200
Figure 5.5: XPS Survey Spectra of Bulk TaON.	201
Figure 5.6: HR-XPS surface analysis of Rh 3d region for supported 0.5%RuO ₂ /TaON photocatalysts.	202
Figure 5.7: HR-XPS surface analysis of Ta 4f region for supported 0.5%RuO ₂ /TaON photocatalysts.	203
Figure 5.8: Schematic Model for the Surface Region of the Supported 0.5%RuO ₂ /TaON photocatalyst.	204

Abstract

Fundamental Characterization Studies of Advanced Photocatalytic Materials

Solar powered photocatalytic water splitting has been proposed as a method for the production of sustainable, non-carbon hydrogen fuel. Although much technological progress has been achieved in recent years in the discovery of advanced photocatalytic materials, the progress in the fundamental scientific understanding of such novel, complex mixed oxide and oxynitride photocatalysts has significantly lagged. One of the major reasons for this slow scientific progress is the limited number of reported surface characterization studies of the complex bulk mixed oxide and oxynitride photocatalyst systems. Although photocatalytic splitting of water by bulk mixed oxide and oxynitride materials involves both bulk (generation of excited electrons and holes) and surface phenomena (reaction of H₂O with excited electrons and holes at the surface), the photocatalysis community has almost completely ignored the surface characteristics of such complex bulk photocatalysts and correlates the photocatalytic properties with bulk properties.

Some of the most promising photocatalyst systems (NaTaO₃, GaN, (Ga_{1-x}Zn_x)(N_{1-x}O_x) and TaON) were investigated to establish fundamental bulk/surface structure photoactivity relationships. The bulk molecular and electronic structures of

the photocatalysts were determined with Raman and UV-vis spectroscopy. Photoluminescence (PL) and transient PL spectroscopy were provided insight into how recombination of photogenerated electrons is related to the photocatalysis activity. The chemical states and atomic compositions of the surface region of the photocatalysts were determined with high resolution X-ray photoelectron spectroscopy (~1-3 nm) and high sensitivity-low energy ion scattering spectroscopy (~0.3 nm).

The new insights obtained from surface characterization clarified the role of La and Ni promoters species for the NaTaO₃ photocatalyst system. The La₂O₃ additive was found to be a structural promoter that stabilizes small NaTaO₃ nanoparticles (NPs) and increases the surface area, but not affecting the specific photoactivity. Only the NiO additive was found to enhance the photoactivity due to the ability of surface NiO_x species to trap photogenerated electrons. The supported Rh-Cr NPs on GaN and (Ga_{1-x}Zn_x)(N_{1-x}O_x) photocatalysts consist of Rh⁺³ which is the catalytic photoactive sites for H₂ along with Cr⁺³, GaZnO or at their contact points being possible sites for O₂ production. The RuO₂ promoted TaON photocatalyst system was found to consist of dissolved Ru⁺⁴ cations in the TaO_x thin film and not as RuO₂ NPs as previously proposed.

In summary, these current studies for the first time revealed the surface nature of mixed oxide and oxynitride photocatalysts and stress the importance of establishing fundamental bulk/surface structure–photoactivity relationships for complex, multicomponent photocatalyst systems.

CHAPTER 1

Overview of Heterogeneous Photocatalyst Literature for Water Splitting

1.1 Introduction

One of the great challenges facing society today is finding alternative renewable energy resources to help alleviate our reliance upon fossil fuels for energy. Hydrogen from non-carbon sources is considered to be one of the potential candidates for replacing fossil fuels for our energy needs. The use of sustainable hydrogen will help to address the depletion of the fossil fuel supply and the environmental problems associated with its use. However, there are still considerable barriers that need to be overcome before hydrogen can be considered a viable energy source such as constructing infrastructure for production, storage and use of hydrogen fuel and finding ways to make sustainable hydrogen economically competitive against other sources of energy [1]. There needs to be a strong emphasize on the research front so that technology can be developed that can overcome these challenging entry barriers. This critical research work needs to be accomplished before the dream of a hydrogen

economy can become a reality. Replacing fossil fuels with hydrogen for our energy use is an ineffectual endeavor unless it can be derived from renewable resources.

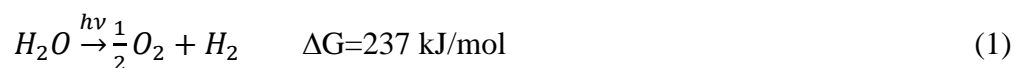
Naturally abundant water and solar energy can be the renewable resources that have the potential to produce hydrogen fuel. The sun produces over 1000 W/m^2 on the earth's surface that far exceeds all of our energy needs [2, 3]. This vision for a renewable hydrogen economy is inspired from biological processes found in nature that have been using sunlight to convert water and carbon dioxide into glucose and oxygen. The photosynthesis process is directly responsible for sustaining all forms of life on Earth. Mimicking this process for production of hydrogen fuel will help to sustain our ever growing energy needs for our society. In this regard, photocatalytic water splitting for hydrogen production is viewed as a form of artificial photosynthesis where a catalyst material can utilize solar energy to convert water into H_2 and O_2 . Solar hydrogen fuel generated from water can be the ultimate in sustainable green energy due to the use of inexpensive naturally abundant H_2O reactants and lack of environmentally damaging byproducts being formed in the reaction. Because of this it is considered one of the "Holy Grails" of chemistry [4] and can be the basis of our hydrogen economy in the future.

Photocatalytic water splitting was first brought to attention by the pioneering work of Fujishima and Honda in 1972 which showed that UV light irradiation of a TiO_2 photoelectrode and a Pt photoelectrode in an aqueous solution led to the production of H_2 and O_2 when a small voltage was applied [5]. The system in this study is considered to be the first photoelectrochemical (PEC) cell designed for water

splitting. Since then, much progress has been made and many PEC cells have been developed which can utilize visible light energy [6]. The designs of these PEC systems are rather complicated due to photoelectrode instability that necessitates the use of multi-component materials in the PEC system, i.e. integrated multilayers and tandem systems [7-9]. The discovery of the Honda-Fujishima effect has provided the inspiration for the utilization of heterogeneous semiconductor materials for photocatalytic water splitting. Unlike PEC cells, the use of heterogeneous semiconductor materials allows for greater simplicity in design for photocatalytic water splitting systems. These systems can be utilized using only the semiconductor powder photocatalyst, water and sunlight which is advantageous since it does not require an external bias or voltage source like PEC cells. The simplicity in design makes photocatalytic water splitting by heterogeneous semiconductors viable for implementation of solar hydrogen production on a large scale. Although photocatalytic water splitting is still in the research phase at this time, there is great promise that this technology can be used to help solve our global energy problem.

1.2 Basic Principle of Photocatalytic Water Splitting

The basic reaction for photocatalytic water splitting given below in equation 1 is considered an uphill reaction due to the large Gibbs free energy involved.



The schematic of the three step photocatalytic water splitting process is shown in Figure 1. The first step of the process involves the absorption of photons in the bulk of the photocatalyst system to form electron/hole pairs caused by the excitation of the electrons from the valence band to the conduction band with the holes being left in the valence band. The photo-generation of electron/hole pairs takes place on the time scale of femtoseconds [10, 11]. The minimum theoretical energy needed is 1.23 eV for the photocatalyst that requires light with wavelength of about 1010 nm, but greater energy is needed to overcome the activation barrier. The bulk band gap energy of the photocatalyst helps to determine the energy of the light source needed to form the electron/hole pairs. The second step of the photocatalytic process deals with charge separation of the generated electron and hole pairs followed by migration to the surface reaction sites. A great challenge to the photocatalytic process is to minimize the immediate recombination of electron/hole pairs before the charge separation occurs. Transient photoluminescence spectroscopy has determined that about 90% or more of the photogenerated electron/hole pairs recombine within 10 ns of excitation, which limits the effective quantum yield to 10% or less on TiO_2 photocatalysts [12]. Defects in the crystal structure can act as recombination centers in the photocatalyst so highly ordered crystalline materials are desired [13]. Particle size also has a great effect on charge transfer since smaller particles lead to shorter migration distances and a lower probability of electron/hole recombination [13]. After the electron/hole pairs migrate to the surface of the photocatalysts, the third and final step of the process is the coupled surface chemical reactions at the catalytic active sites where the excited

electrons react with H^+ to form H_2 at one catalytic active site and excited holes help to oxidize water into O_2 at a different catalytic active site as depicted in Figure 1.

A “co-catalyst”, which is commonly used terminology in the literature, is typically deposited on the photocatalyst that makes the photocatalyst active or significantly increases the activity of the photocatalyst. It is not always clear which component in a multi-component photocatalyst system is the catalytic active site so it is not appropriate to call one component “the photocatalyst” and another component the “co-catalyst”. In order to discern the functions of the different components in the photocatalyst system, it is more appropriate to view the bulk component as the electron/hole generator and the active surface components as the catalytic active sites in a photocatalytic system, which is analogous to supported metal oxide catalysts where the catalytic active component is deposited on a high surface area support [14, 15]. This would help to clarify the role of each component in the photocatalyst system. One of the main difficulties of finding appropriate component materials for photocatalytic water splitting is the balance between finding suitable bulk molecular/electronic properties and surface molecular/electronic properties of a photocatalytic system.

1.3 Semiconductor Materials for Photocatalytic Water Splitting

Since TiO_2 was first used by Fujishima and Honda for their PEC cell for water splitting, it has become the most widely studied photocatalyst to date [16]. The main difficulty with using TiO_2 for photocatalytic water splitting is the low activity of H_2

production and the undetectable amounts of O_2 evolution attributed to adsorbed O_2 species on the TiO_2 [3, 17]. Only with the addition of another catalyst component such as Pt [18] or in the presence of alkali carbonates [19] has stoichiometric amounts of H_2 and O_2 been produced using TiO_2 as the bulk electron/hole generator. TiO_2 photocatalyst applications have focused more on environmental applications such as photocatalytic oxidation of organic toxins in water and for air purification [16].

Over the years, many other metal oxide semiconductor materials have been discovered (>130) which are much more efficient for photocatalytic water splitting compared to TiO_2 [3, 13, 20, 21]. From all of the discovered materials for photocatalytic water splitting, only certain semiconductor materials possess suitable bulk band gap structures which can generate electron/hole pairs that can be used for photocatalytic water splitting. These semiconductor photocatalysts have been found to have either empty d orbitals (defined as having d^0 configuration) or filled d orbitals (defined as having d^{10} configuration) [20]. Materials with partially filled d orbitals do not possess a suitable electronic structure due to the partially filled d orbitals that act as recombination centers for electron/hole pairs. Transition metal oxides that satisfy the former criteria are those that contain Ti^{4+} , Zr^{4+} , Nb^{5+} , Ta^{5+} , and W^{6+} and main group metal oxides that satisfy the latter criteria are those that contain Ga^{3+} , In^{3+} , Ge^{4+} , Sn^{4+} , and Sb^{5+} . Photocatalytic studies for water splitting under UV light excitation have shown that trends in H_2/O_2 production follow the size of the transition metal oxide band gap where the larger band gaps reflect an increasing thermodynamic driving force for water splitting [3]. Tungstates (WO_3 , 2.8 eV) are less active than

titanates (TiO_2 , 3.0-3.1 eV) and are generally less active than niobates (Nb_2O_5 , 3.1-3.5 eV), which in turn are generally less active than tantalates (Ta_2O_5 , 4.0-4.6 eV). Pure ZrO_2 (5.0 eV) with its large band gap is able to photocatalytically split water [22-24] but other zirconia-based photocatalysts have not been discovered like the other d^0 transition metal oxides possibly due to poor absorption ($< 248 \text{ nm}$) with commonly used Xe and Hg light sources [3]. There have not been as many d^{10} main group metal oxide photocatalysts which have been discovered compared to d^0 transition metal oxides and the d^{10} metal oxide photocatalyst are generally less active compared to d^0 metal oxide photocatalyst. Some of the effective photocatalysts consist of the bulk mixed oxides of SrTiO_3 [25], Ta_2O_5 [26], $\text{K}_2\text{La}_2\text{Ti}_3\text{O}_{10}$ [27], $\text{Sr}_2\text{Nb}_2\text{O}_7$ [28], $\text{K}_3\text{Ta}_3\text{Si}_2\text{O}_{13}$ [29], NaTaO_3 [30], $\text{NaTaO}_3\text{:La}$ [31], RbTaWO_6 [32], ZnGa_2O_4 [33], CaIn_2O_4 [34], ZnGeO_4 [35], Sr_2SnO_4 [36] and NaSbO_3 [36]. Like TiO_2 -based photocatalysts, the activity of these bulk mixed oxide photocatalysts have been shown to be greatly enhanced by the presence of another catalyst component such as Pt, Rh_2O_3 , NiO and RuO_2 .

Out of all of these photocatalytic materials that are activated by UV illumination, tantalum-based photocatalysts have shown great promise for photocatalytic water splitting. Kudo's group has demonstrated that tantalum-based photocatalysts such as Ta_2O_5 [23, 26], NaTaO_3 [30], $\text{K}_3\text{Ta}_3\text{Si}_2\text{O}_{13}$ [29], $\text{K}_2\text{PrTa}_5\text{O}_{15}$ [37], $\text{Sr}_2\text{Ta}_2\text{O}_7$ [38] and $\text{NiO/NaTaO}_3\text{:La}$ [31, 39] are among the most active photocatalysts under UV-irradiation for the photocatalytic conversion of H_2O into H_2/O_2 . The $\text{NiO/NaTaO}_3\text{:La}$ photocatalyst system is the most active photocatalyst

discovered to date with an apparent quantum efficiency (number of reacted electrons/ number of incident photons) of 56% using UV excitation with $\lambda > 270$ nm [31, 39]. The bulk NaTaO_3 forms a perovskite crystal structure after calcination and is able to photocatalytically split water into H_2 and O_2 . The activity of the bare NaTaO_3 was improved by 2.6x by the addition of La, 12.8x by addition of NiO and 116.5x with the simultaneous addition of both La and NiO. Transmission electron microscopy (TEM) showed that the $\text{NaTaO}_3\text{:La}$ particles are smaller than the unmodified NaTaO_3 and contain characteristic ordered nanostep structures not found in the NaTaO_3 . It was proposed that well-dispersed NiO deposited on the edges of the nanostep structures are the catalytic active site for H_2 production and O_2 was produced at the grooves of the nanostep structures. The proposed model, however, was established with only bulk characterization techniques (XRD, TEM, XANES, and XAFS) and no surface characterization methods were employed to directly confirm the conclusions on the nature of the surface catalytic active sites.

Although there are a large number of semiconductor metal oxide materials that can perform photocatalytic water splitting using UV-irradiation, the large band gap energies of these semiconductors hinders their ability to utilize visible light energy. Only NiO/InTaO_4 (Q.E. = 0.7%) [40], $\text{RuO}_2\text{/InTaO}_4$ (Q.E. = 0.4%) [41] and $\text{RuO}_2\text{/YBiWO}_6$ (Q.E. = 0.2%) [42] have been found to be able to perform the water splitting reaction under visible light excitation, but with very low quantum efficiencies. Metal oxynitride catalysts $((\text{Ga}_{1-x}\text{Zn}_x)(\text{N}_{1-x}\text{O}_x))$ and $(\text{Zn}_{1+x}\text{Ge})(\text{N}_2\text{O}_x)$ discovered by Domen's group synthesized from metal oxides calcined under NH_3 flow

have been shown to be able to overcome band gap limitations of semiconductor metal oxides and can perform visible light water splitting [20, 43, 44]. DFT calculations have theorized that there is a strong p-d repulsive force between N2p and Zn3d orbitals in the valance band of these materials that shifts the valence band position upwards without affecting the conduction band position [45, 46]. This narrowing of the band gap is responsible for the visible light absorption for these metal oxynitride photocatalysts. The $(\text{Rh}_{2-y}\text{Cr}_y\text{O}_3)/(\text{Ga}_{1-x}\text{Zn}_x)(\text{N}_{1-x}\text{O}_x)$ catalyst is the most active of all the oxynitride photocatalysts under visible light water splitting ($\lambda > 400\text{nm}$) with an optimized apparent quantum efficiency of 5.9% [47-50]. The bulk structure of the $(\text{Ga}_{1-x}\text{Zn}_x)(\text{N}_{1-x}\text{O}_x)$ has been shown to have a wurtzite solid solution crystal structure. The supported $(\text{Rh}_{2-y}\text{Cr}_y\text{O}_3)$ mixed oxide nanoparticles are proposed to be the active site for H_2 production while the $(\text{Ga}_{1-x}\text{Zn}_x)(\text{N}_{1-x}\text{O}_x)$ support provides the active sites for O_2 production. As in the other studies on photocatalyst systems, only bulk characterization techniques were applied and no surface characterization methods were employed. Thus, further work needs to be performed to fully understand the surface aspects of this novel photocatalyst system and especially the nature of the catalytic active sites at the surface.

All of the photocatalyst systems mentioned above are conventional one-step systems for photocatalytic water splitting where H_2 and O_2 are produced on the surface of the photocatalyst. There is a new class of materials being developed which utilize a two-step process for photocatalytic water splitting which are called “Z-Scheme” photocatalyst systems. In the two-step Z-Scheme process, one catalyst is used for H_2

evolution while another catalyst is used for O₂ evolution. A shuttle redox couple (Red/Ox) in solution is used to transfer electrons between the two catalysts. A schematic energy diagram comparing the two types of photocatalytic water splitting systems is shown in figure 2. On the H₂ evolution catalyst, excited electrons are used to reduce water into H₂ while holes in the valance band are used to oxidize the reductant (Red) to an oxidant (Ox). On the O₂ evolution catalyst, excited electrons are used to reduce the Ox into the Red while holes in the valance band are used to oxidize water into O₂. The advantage of using a Z-Scheme system is that the band gap requirement for water splitting is less restrictive compared to a one-step system [51]. This allows for visible light irradiation to be more easily attainable since the band gap positioning of the H₂ evolution catalysts only needs to oxidize the reductant to an oxidant and the O₂ evolution catalyst only needs to be able to reduce the oxidant to the reductant that are less energetic compared to the one-step system. The Z-scheme systems which have been discovered involve combining Pt/SrTiO₃:Rh with BiVO₄, Bi₂MoO₆, or WO₃ using Fe^{3+/2+} as the shuttle redox couple [52], combining Pt/TaON or Pt/ZrO₂/TaON with RuO₂/TaON or Pt/WO₃ using IO₃⁻/I⁻ as the shuttle redox couple [53-55]. Although Z-Scheme photocatalyst systems are a more recent discovery compared to one-step photocatalyst systems, the most active Z-scheme photocatalyst system (Pt/ZrO₂/TaON with Pt/WO₃) has a quantum yield of 6.3% at $\lambda > 420$ nm [55], which is higher than the most active one-step system ((Rh_{2-y}Cr_yO₃)/ (Ga_{1-x}Zn_x)(N_{1-x}O_x)) at 5.9% at $\lambda > 400$ nm. Not much research work has been devoted to Z-scheme photocatalyst systems since it is a more recently developed system so there is potential

for new materials to be discovered that can greatly improve the photoactivity for Z-scheme systems.

Metal sulfide materials have also attracted a good deal of attention for photocatalytic water splitting due to their small band gap that allows for visible light absorption [3, 13]. The valence band for these materials usually consist of S 3p orbitals which are at a higher potential than O 2p orbitals typical of metal oxides. The main disadvantage of using metal sulfides is that photocorrosion occurs readily and the use of sacrificial reagents (Na_2SO_3 , K_2SO_3 , and Na_2S) is required for stability and to act as electron donors. In the presence of H_2O , sulfide species rather than H_2O are oxidized by the photogenerated holes causing catalyst instability and preventing O_2 evolution for these photocatalysts. With the use of sacrificial reagents the apparent quantum efficiency of metal sulfide photocatalysts can reach 25% at 440 nm (Rh/AgGaS_2) [56] and 7.4% at 520 nm ($\text{Ru}/\text{Cu}_{0.25}\text{Ag}_{0.25}\text{In}_{0.5}\text{ZnS}_2$) [57, 58] for the production of hydrogen without any oxygen products formed in the reaction. These materials are currently able to absorb light up to 650 nm for hydrogen production. Although metal sulfide photocatalysts act only as hydrogen evolution catalysts and do not stoichiometrically produce H_2 and O_2 for overall water splitting, metal sulfide photocatalysts have the potential to become important if abundant sulfur compounds from chemical plants or nature can be found that can be used as electron donors for this reaction.

This review of photocatalyst systems for water splitting has shown that many advanced photocatalytic materials have been discovered over the past 40 years that

can perform the water splitting reaction. The efficiency of these photocatalyst systems, however, is still below the desired target of 30% quantum efficiency at 600 nm excitation that corresponds to about 5% solar energy conversion [13]. It is at this point where photocatalyst systems start to become more economically viable for use on a large-scale. Development of more efficient photocatalytic materials is currently limited due to the lack of fundamental knowledge of their photocatalytic mechanisms. Most of these studies have focused on using bulk characterization techniques to propose photocatalyst models and are lacking in surface characterization of the catalytically active sites, surface reaction intermediate species and interfacial electronic mechanisms of the complex, coupled reactions involved in water splitting. Combining both bulk and surface characterization is essential for determining the role of each component in the system. This becomes even more critical since future photocatalyst systems will most likely have an increased number of components and verifying the role of each component in the system will help to establish fundamental structure-photoactivity relationships for the complex photocatalyst systems.

1.4 Overview of Characterization Techniques Utilized for Heterogeneous Mixed Oxide Photocatalyst Systems for Water Splitting

Most of the studies in the literature on the heterogeneous photocatalytic systems for water splitting have primarily focused on correlating bulk properties with photoactivity. In the past, the main focus of photocatalytic water splitting research has been finding suitable bulk mixed oxide materials that can act as electron/hole

generators for the photocatalyst system. Subsequently, bulk characterization techniques have been primarily employed to investigate these active photocatalyst systems. The characterization techniques primarily focused on: X-ray Diffraction (XRD), ultraviolet-visible diffuse reflectance spectroscopy (UV-vis DRS), X-ray absorption near edge spectroscopy (XANES), extended X-ray absorption fine spectroscopy (EXAFS), electron microscopy (EM), inductively coupled plasma atomic emission spectroscopy (ICP-AES), photoluminescence (PL) spectroscopy, Brunauer-Emmett-Teller (BET) surface area, attenuated total reflectance infrared (ATR-IR) spectroscopy, and X-ray photoelectron spectroscopy (XPS) to give insights into the properties of the photocatalyst systems. These characterization techniques, however, provide only bulk structural and electronic information about the photocatalyst systems, with the exception of BET, ATR-IR, and XPS that can give some limited surface information about the photocatalyst systems. The different characterization techniques will be discussed in this section and the strengths and weaknesses of each technique for studying photocatalytic systems will be highlighted.

1.4.1 X-ray Diffraction (XRD)

XRD involves focusing beams of X-rays which scatter from lattices in the sample forming diffraction patterns. At certain angles, scattered X-rays are combined constructively and are measured as a function of diffraction angle, 2θ . The diffraction patterns formed can be used as identifiers for crystal lattices found in the material. This allows for the determination of the crystalline phase, quantitative composition of multi-component systems, lattice parameters, crystalline size and shape, bulk defect

types and concentration (micro-strains) and the presence of doping elements in the crystal lattices of the photocatalyst system [59]. The disadvantages of XRD is that it only provides analysis of bulk crystalline phases and is unable to provide surface information, detect amorphous phases or detect crystalline particles smaller than 3 nm due to peak broadening. XRD is, therefore, only limited to providing bulk structural information about large particles (> 3 nm) that tend to be the supports that are responsible for generating excited electron/hole of the photocatalyst system.

1.4.2 X-ray Absorption Spectroscopy (XANES and EXAFS)

The complimentary synchrotron-based X-ray absorption spectroscopic techniques of X-ray Absorption Near Edge Spectroscopy (XANES) and Extended X-ray Absorption Fine-Structure Spectroscopy (EXAFS) are based on the absorption of X-rays by the sample that excites an electron from a core state to an empty state at above the Fermi level. This process emits photons from the sample of interest that are subsequently scattered by nearby atoms. This interaction gives off fluorescence emissions and transmissions modes that contain detailed local structural and electronic information of the photocatalyst systems [60]. The XANES region focuses on the pre-edge, the edge and features up to 50 eV above the absorption edge of a specific element in the photocatalyst, while the EXAFS region includes all features in the spectrum above 50 eV from the edge of a specific element in the photocatalyst [61]. XANES is used to discriminate between different oxidation states and local bonding geometry of a specific element. EXAFS is used to determine the bond length and local geometry between different elements present in the photocatalyst. A major

drawback to these characterization techniques is that they average their signal from multiple sites of the same element and, therefore, are not well suited for materials containing multiple components with different oxidation states or structures [62]. Furthermore, surface information is only provided for highly dispersed systems or materials with high surface area, but the usually low surface areas of photocatalysts ($< 10 \text{ m}^2/\text{g}$) assures that the XAS signals will be dominated by the elements present in the bulk phase of the photocatalysts.

1.4.3 Electron Microscopy

Electron microscopy provides the images of a photocatalyst with up to an atomic scale resolution ($< 0.1 \text{ nm}$) that gives insight into the structure and morphology of the photocatalyst system. Electron microscopy encompasses many different techniques, Transmission Electron Microscopy (TEM), Scanning Electron Microscopy (SEM), Scanning Transmission Electron Microscopy (STEM), Energy-Dispersive X-ray Spectroscopy (EDX), and Electron Energy-Loss Spectroscopy (EELS), which have been used to characterize photocatalyst systems. TEM is the most commonly used of these electron techniques for studying photocatalytic materials. TEM functions by generating a primary electron beam of high energy and high intensity that passes through a condenser to produce parallel beams that irradiate the sample. Magnified images of the sample are formed by combining the transmitted electrons using an electromagnetic objective lens. TEM is primarily used to give information on topography, morphology and crystal structure at with atomic resolution (0.1 nm) [63] and bulk composition when coupled with EELS. SEM is carried out by rastering

a narrow electron beam over the surface of the sample and detects the yield of secondary or backscattered electrons as a function of the primary beam. The main difference between SEM and TEM is that SEM sees contrast due to topology and composition of a surface, while the TEM projects all information on the mass it encounters in a 2-D image of subnanometer resolution [62]. SEM instruments only have a lateral resolution of ~ 5 nm and are useful for determination of surface morphology and larger nanoparticles compared to TEM analysis. STEM combines both modes mentioned above and utilize scanning coils to illuminate a small area of the sample from which bright or dark field images are obtained. STEM can be combined with the high-angle annular dark field (HAADF) imaging technique to provide Z-contrast images which can distinguish particles of different atomic number. The image brightness is approximately dependent on the square of the atomic number (Z^2) of the atoms present and very useful for particles with a great difference in atomic mass and not so useful for particles with similar atomic masses.

The elemental composition of a sample can be determined by combining EDX and EELS analysis with the electron microscopic imaging techniques mentioned above. EDX is the more commonly used technique and involves ionization of the sample from the X-rays of the microscope. The X-ray emissions from this ionization event are then analyzed with a solid-state energy dispersive detector. Each element gives out a unique pattern of X-ray lines from the K, L, and M shells which allows for straightforward analysis. EELS is complimentary to EDX in that the ionization event that occurs in the sample leads to a characteristic loss in energy of the transmitted

electrons that can also be detected. EELS is very sensitive to lighter elements ($Z < 11$) where the energy losses are small where EDX is more sensitive to heavier elements ($Z > 11$) [63]. These techniques are also useful for constructing elemental maps to characterize the microstructural composition and elemental distribution of multicomponent catalysts on the nanometer scale. All the electron microscopy techniques, however, only provide structural information about crystalline components (< 1 nm) and do not provide structural information about amorphous or surface phases. An exception occurs is when an element with a high Z number is dispersed as an amorphous surface phase on a support with low Z number elements [64].

1.4.4. Infrared (IR) spectroscopy

Infrared spectroscopy provides vibrational information about chemically bonded surface reaction intermediates and the changes in these molecular vibrations give insight into the bond breaking/making process essential to understanding the catalytic reaction mechanism. Infrared spectroscopy is a bulk technique that can provide bulk structural information as well as the nature of the surface species if the surface area is sufficient to accommodate significant number of surface species. Conventional IR spectroscopy cannot be used to probe photocatalytic water splitting reactions due to the strong absorption by water which requires the use of attenuated total reflectance infrared (ATR-IR) spectroscopy [65, 66]. An advantage of ATR-IR over conventional transmission IR and DRIFTS methods is that ATR-IR only probes the molecules that are located near the surface (μm) in the catalyst region instead of the entire volume of the photoreactor. Thus, ATR-IR spectroscopy allows for *in-situ*

analysis of the solid/liquid interfaces during photocatalytic water splitting. It can be used to obtain information about chemical and geometrical structures of surface species and also give information on reaction mechanism and kinetics [67, 68]. Some of the challenges with *in-situ* ATR-IR for photocatalytic water splitting include weak signals from the low surface area photocatalytic materials, difficulty discriminating between active and spectator species, diatomic molecules such as H₂ and O₂ not being active in IR, and the strong water absorption leading to regions that cannot be used for analysis.

1.5 Approach and Outline of This Thesis

The previous section has highlighted the characterization techniques that have been employed to study photocatalytic materials. One of the major issues with the previous studies has been the focus on correlating bulk structural properties of the photocatalyst systems with photoactivity [26, 31, 47-49, 69, 70]. The lack of surface characterization of the outermost surface layer has led to a catalysis paradigm for bulk mixed metal oxide catalysis including photocatalysts, where bulk structural features are correlated with catalytic activity [71, 72]. Catalytic reactions are a surface phenomenon and surface characterization is needed to correlate surface properties with catalytic activity and to better understand the fundamentals of photocatalysis. Only when surface characterization is performed can appropriate models for catalytic active sites be determined for photocatalytic systems.

This section will look at characterization techniques and the photocatalytic reactor employed in this study for determination of bulk/surface structure – photoactivity relationships for photocatalyst systems for water splitting. Raman spectroscopy will be used to determine the bulk molecular structure of the photocatalyst systems. The bulk electronic structure will be examined using UV-vis diffuse reflectance spectroscopy. Photoluminescence spectroscopy will be used to explore the state of the excited electrons and the lifetime of the excited electrons in the photocatalyst system. Since photocatalyst systems are complex multicomponent systems, bulk characterization techniques are useful for determining the effect of each component on the bulk properties of the photocatalyst system. The oxidation state of surface species (~1-3 nm) will be determined using X-ray photoemission spectroscopy while the composition of the outermost surface layer (~0.3 nm) of the photocatalyst system will be revealed for the first time using high sensitivity low energy ion scattering spectroscopy. Combining bulk and surface characterization will allow for determining the role of each component in the photocatalyst system and allow for more accurate models for the catalytic active sites and the photocatalytic reactions.

1.5.1 Raman Spectroscopy

Raman spectroscopy is a powerful characterization technique which provides vibrational information about the bulk mixed oxide molecular structures and can also give information about surface structures in a photocatalyst system for high surface area materials [73]. Raman spectroscopy is an ideal characterization technique because it can operate in all phases (gas, solid, and liquid), and over a wide range of

temperatures and pressures that are useful for *in situ* studies during photocatalytic water splitting reactions [73]. Like other bulk techniques, the Raman spectra are dominated by the signal from bulk phase due to the greater Raman scattering from the ordered crystalline lattice compared to disordered amorphous surface phases. The ability to detect amorphous phases along with a greater sensitivity for detection of smaller ordered nanoparticles (< 3 nm) makes Raman a more a better tool than the comparable XRD characterization technique. The sharpness of the Raman peaks help to qualitatively determine the relative crystallinity of the bulk phase of the photocatalyst system. Sample fluorescence, one of the limitations for Raman spectroscopy, is not much of an issue when dealing with photocatalyst systems since the bulk mixed oxide photocatalysts tend to give strong Raman signals. Additionally, UV Raman has greater sensitivity towards the surface region of a solid sample than conventional Raman spectroscopy [74].

1.5.2 Ultraviolet-visible (UV-vis) Diffuse Reflectance Spectroscopy (DRS)

UV-vis diffuse reflectance spectroscopy is a characterization technique used to obtain information about the electronic structure of the photocatalyst system based on the absorptive and light scattering properties of the sample under light excitation from the 200–800 nm range. The sample absorbance is then referenced against an MgO standard and the Kubulka Monk function can be calculated for the sample that allows determination of the optical band gap for photocatalyst materials [75-77]. The optical band gap determines how much photon energy is required to generate excited electron/hole pairs in the bulk of the photocatalyst material. It is desirable for a

photocatalyst system to have band gap values below 3.0 eV to be able to absorb energy in the visible light region [20]. Since UV-vis DRS looks at electronic transitions from ground state to excited states in the sample, it is also used to give obtain information on the oxidation states, and coordination of metals from metal-centered and charge transfer transitions [78, 79]. One of the drawbacks to using UV-vis DRS is that it is a bulk technique so the information obtained from it is averaged from all the components of the photocatalysts system, bulk and surface, and cannot give specific information about individual components and the surface region. An advantage of UV-vis DRS is that it can performed under *in situ* conditions during photocatalytic splitting of water

1.5.3 Photoluminescence (PL) Spectroscopy

Photoluminescence spectroscopy is a complimentary technique to UV-vis DRS in that it also gives information on the electronic structure from light excitation. Whereas UV-vis DRS looks at the transition from the ground state to the excited state, PL spectroscopy differs by examining the transition from the excited state to the ground state. The emission of photons from this phenomenon can be measured as fluorescence. This process is relevant to the study of photocatalyst systems since fluorescence occurs when electrons in the conduction band recombine with holes in the valence band. This characterization technique can thus give direct information on electron transfer kinetics during the photocatalytic process. The PL intensity can then be used to compare recombination rates for different photocatalyst systems, determine the band gap energy, and detect impurities and defects in the sample [80, 81]. PL

spectroscopy has the same drawback as UV-vis DRS in that it is a bulk technique and cannot give specific information about individual components nor surface species. However surface species can have a large effect on the PL spectra since surface sites and the presence of adsorbed surface molecules can act as efficient electron traps which help to decrease PL intensity preventing electron/hole recombination [74, 81].

Time-resolved picosecond *in situ* PL (TR-PL) spectroscopy will also be utilized to examine the recombination lifetimes of electron/hole pairs. Whereas conventional or steady-state PL spectroscopy uses continuous excitation from a light source, TR-PL spectroscopy relies on pulsed excitation and measures photoluminescence at certain time intervals after the pulse excitation [80, 82]. The PL emission intensity over time is then fitted to an exponential decay model to determine the lifetimes of photo-generated electron/hole pairs [83, 84]. An increased lifetime of photogenerated electron/hole pairs has been shown to correlate with TiO₂ for photocatalytic splitting [85, 86] and this relationship will be investigated for more active photocatalyst systems.

1.5.4 High-Resolution X-ray Photoemission Spectroscopy (HR-XPS)

XPS is a surface technique that utilizes photons from an X-ray source to excite the electronic states of atoms near the surface (~1-3 nm) of a solid. The electrons ejected from the sample are collected by a hemispherical electron energy analyzer which measures the kinetic energy of the ejected electrons. The kinetic energy measured can then be used to determine the binding energy of the electron from the following equation:

$$E_k = h\nu - E_b - \phi \quad (2)$$

Where h is Planck's constant, ν is the frequency of the exciting energy source, and ϕ is the work function of the spectrometer [62]. Each ejected electron from an element has a characteristic binding energy and the position of this binding energy is used to identify the element and core level of the electron that can be found by consulting binding energy tables [87]. The peak intensities can be used to quantitatively determine the elemental composition (detection limit ~ 1000 ppm for most elements) and the peak positions can be used to determine oxidation states for the elements. In general, binding energies increase with increasing oxidation state typically shifting by about 0-3 eV [62]. Some of the disadvantages of XPS are that it requires ultra-high vacuum conditions, sample damage from the X-ray sources, not sensitive enough to get information on only the outermost layer (~ 0.3 nm) and overlapping elemental peaks that can make spectra analysis challenging.

1.5.5 High Sensitivity Low Energy Ion Scattering Spectroscopy (HS-LEISS)

HS-LEIS is a unique surface characterization technique is a powerful tool for analysis of the *outermost* surface layer (~ 0.3 nm) of the photocatalyst system that gives insight into the nature of the catalytic active sites on the photocatalyst surface. During HS-LEIS, the surface of the sample is bombarded by a noble gas ion with a known energy and a binary collision occurs between the noble gas ion and a surface

atom. The energy of the backscattered ion, E_f , can be determined by the conservational laws of momentum and energy by the equation:

$$E_f = k \left(\frac{\cos \theta \pm \sqrt{\left(\frac{m_1}{m_2}\right)^2 - \sin^2 \theta}}{1 + \frac{m_1}{m_2}} \right)^2 E_0 \quad (3)$$

In this, k is the kinematic factor, m_1 and m_2 are the masses of the primary ion and the scattered surface atom, θ is the back scattering angle, and E_0 is the initial energy for the primary ion [88]. All of the variables are known for the experiment except for m_2 so that value is able to be back-calculated from the experimental data obtained for the backscattered ions. HS-LEIS spectroscopy is used to quantitatively determine the atomic composition of the outermost atomic layer and can detect all elements except for H and He. HS-LEIS spectroscopy is orders of magnitude more sensitive than conventional LEIS spectroscopy with elemental detection as low as 10 ppm and uses lower doses of primary gas ions to obtain static spectra sputtering less than 0.5% of a monolayer [89, 90]. Noble gas ions can penetrate the surface into deeper layers, but are usually neutralized upon scattering; however some particles can become re-ionized and show up as a low energy tail to the peak obtained from surface atoms. The shape of this tail can give information on the distribution of the elements over deeper layers up to 10 nm [89]. Alternatively, a secondary ion source can be used for sputter depth profiling, which can also give information about deeper layers. The disadvantages of using HS-LEIS spectroscopy are that it requires ultra-high vacuum conditions, it does

not give chemical state information (oxidation state) and it may be difficult to distinguish between elements with similar atomic masses.

1.5.6 Photocatalytic Reactor for Water Splitting

There are two different reactor cell designs that are used for photocatalytic water splitting and a schematic of the two reactors are presented in Figure 3. The reactor system consists of a closed-gas circulation system connected to a vacuum pump that removes ambient air from the system prior to the reaction so no atmospheric oxygen is present in the system during photocatalysis. A suspension consisting of the photocatalyst and water is created in the reaction cell with a magnetic stirrer put in to continuously stir the suspension. An inner irradiation reactor cell is used when a UV lamp (high pressure 450W Hg lamp) is used for irradiation while a top down reactor cell is used when a Xe arc lamp is used. A solar simulator can also be used if solar hydrogen production is desired. Appropriate filters are employed when the experiment requires visible light irradiation. Typically NaNO_2 is utilized to filter out UV light in the inner irradiation reactor while cut-off filters are employed for top down reactors. These reactor cells are connected to a water cooling system to maintain room temperature and to minimize the effects from heating due to the high powered lamps. A Liebig condenser is utilized to prevent gas phase water from escaping the reactor so only H_2 and O_2 can be found in the rest of the system. A gas chromatograph is then used to quantify the amount of H_2 and O_2 products.

1.5.7 Dissertation Outline

Although there are over one hundred photocatalyst systems for water splitting that have been discovered, only a few of the more relevant and most studied photocatalyst systems will be investigated. In chapter 2, Ta_2O_5 and NaTaO_3 –based photocatalysts will be examined since these are the most active metal oxide photocatalyst under UV irradiation. Chapter 3 will look at GaN which is an UV active oxynitride photocatalyst. There are two different synthesis methods for the $(\text{Ga}_{1-x}\text{Zn}_x)(\text{N}_{1-x}\text{O}_x)$ photocatalysts which have led to two different proposed models for their catalytic active sites. The validity of the models for these visible light oxynitride photocatalysts will be the focus of investigation in Chapter 4. Chapter 5 will look at TaON photocatalysts which are capable of absorbing light up to 600 nm and is used in Z-scheme photocatalyst systems. Chapter 6 will give a summary of the conclusions found in this dissertation on the photocatalyst systems studied. The future outlook will look at how other characterization techniques can be used to further elucidate the photoactivity of existing photocatalytic materials so fundamental structure-activity relationships can be established for the design of advanced photocatalyst systems.

References

- [1] U.S. Department of Energy (Ed.), *Basic Research Needs for the Hydrogen Economy; A Report from the Basic Energy Sciences Workshop on Hydrogen Production, Storage, and Use*, U.S. Department of Energy, Washington D.C., 2003.
- [2] N.S. Lewis, D.G. Nocera, "Powering the planet: Chemical challenges in solar energy utilization " *Proceedings of the National Academy of Sciences*, **103**, 15729, (2006).
- [3] F.E. Osterloh, "Inorganic Materials as Catalysts for Photochemical Splitting of Water." *Chem. Mater.*, **20**, 35, (2008).
- [4] A.J. Bard, M.A. Fox, "Artificial Photosynthesis: Solar Splitting of Water to Hydrogen and Oxygen " *Acc. Chem. Res.*, **28**, 141, (1995).
- [5] A. Fujishima, K. Honda, "Electrochemical photolysis of water at a semiconductor electrode." *Nature (London)*, **238**, 37, (1972).
- [6] M.G. Walter, E.L. Warren, J.R. McKone, S.W. Boettcher, Q. Mi, E.A. Santori, and N.S. Lewis, "Solar water splitting cells " *Chem. Rev.*, **110**, 6446, (2010).
- [7] Y. Sakai, S. Sugahara, M. Matsumura, Y. Nakato, and H. Tsubomura, "Photoelectrochemical water splitting by tandem type and heterojunction amorphous silicon electrodes " *Canadian Journal of Chemistry*, **66**, 1853, (1988).

- [8] O. Khaselev, "A Monolithic Photovoltaic-Photoelectrochemical Device for Hydrogen Production via Water Splitting " *Science*, **280**, 425, (1998).
- [9] S. Licht, B. Wang, S. Mukerji, T. Soga, M. Umeno, and H. Tributsch, "Efficient Solar Water Splitting, Exemplified by RuO₂-Catalyzed AlGaAs/Si Photoelectrolysis " *The Journal of Physical Chemistry B*, **104**, 8920, (2000).
- [10] A. Mills, S. Le Hunte, "An overview of semiconductor photocatalysis " *J. Photochem. Photobiol. A*, **108**, 1, (1997).
- [11] A. Kubacka, M. Fernandez-Garcia, and G. Colon, "Advanced Nanoarchitectures for Solar Photocatalytic Applications," *Chem. Rev.*, **112**, 1555, (2012).
- [12] N. Serpone, D. Lawless, R. Khairutdinov, and E. Pelizzetti, "Subnanosecond Relaxation Dynamics in TiO₂ Colloidal Sols (Particle Sizes $R_p = 1.0\text{-}13.4$ nm). Relevance to Heterogeneous Photocatalysis." *J. Phys. Chem.*, **99**, 16655, (1995).
- [13] A. Kudo, Y. Miseki, "Heterogeneous photocatalyst materials for water splitting." *Chem. Soc. Rev.*, **38**, 253, (2009).
- [14] I.E. Wachs, "Recent conceptual advances in the catalysis science of mixed metal oxide catalytic materials " *Catalysis Today*, **100**, 79, (2005).
- [15] J.S.J. Hargreaves (Ed.), *Metal Oxide Catalysis*, Wiley-VCH.

- [16] A.L. Linsebigler, G. Lu, and J.T. Yates, "Photocatalysis on TiO₂ Surfaces: Principles, Mechanisms, and Selected Results " *Chem. Rev.*, **95**, 735, (1995).
- [17] T. Takata, A. Tanaka, M. Hara, J.N. Kondo, and K. Domen, "Recent progress of photocatalysts for overall water splitting " *Catalysis Today*, **44**, 17, (1998).
- [18] S. Tabata, H. Nishida, Y. Masaki, and K. Tabata, "Stoichiometric photocatalytic decomposition of pure water in Pt/TiO₂ aqueous suspension system." *Catal. Lett.*, **34**, 245, (1995).
- [19] K. Sayama, H. Arakawa, "Effect of carbonate salt addition on the photocatalytic decomposition of liquid water over Pt-TiO₂ catalyst." *J. Chem. Soc. , Faraday Trans.*, **93**, 1647, (1997).
- [20] K. Maeda, K. Domen, "New Non-Oxide Photocatalysts Designed for Overall Water Splitting under Visible Light." *J. Phys. Chem. C*, **111**, 7851, (2007).
- [21] X. Chen, S. Shen, L. Guo, and S.S. Mao, "Semiconductor-based Photocatalytic Hydrogen Generation " *Chem. Rev.*, **110**, 6503, (2010).
- [22] K. Sayama, H. Arakawa, "Photocatalytic decomposition of water and photocatalytic reduction of carbon dioxide over zirconia catalyst." *J. Phys. Chem.*, **97**, 531, (1993).

- [23] K. Sayama, H. Arakawa, "Effect of Na₂CO₃ addition on photocatalytic decomposition of liquid water over various semiconductor catalysts." *J. Photochem. Photobiol. , A*, **77**, 243, (1994).
- [24] K. Sayama, H. Arakawa, "Effect of carbonate addition on the photocatalytic decomposition of liquid water over a ZrO₂ catalyst." *J. Photochem. Photobiol. , A*, **94**, 67, (1996).
- [25] K. Domen, S. Naito, T. Onishi, and K. Tamaru, "Photocatalytic decomposition of liquid water on a nickel(II) oxide-strontium titanate (SrTiO₃) catalyst." *Chem. Phys. Lett.*, **92**, 433, (1982).
- [26] H. Kato, A. Kudo, "New tantalate photocatalysts for water decomposition into H₂ and O₂." *Chem. Phys. Lett.*, **295**, 487, (1998).
- [27] T. Takata, Y. Furumi, K. Shinohara, A. Tanaka, M. Hara, J.N. Kondo, and K. Domen, "Photocatalytic Decomposition of Water on Spontaneously Hydrated Layered Perovskites." *Chem. Mater.*, **9**, 1063, (1997).
- [28] H.G. Kim, D.W. Hwang, J. Kim, Y.G. Kim, and J.S. Lee, "Highly donor-doped (110) layered perovskite materials as novel photocatalysts for overall water splitting." *Chem. Commun. (Cambridge)*, 1077, (1999).

- [29] A. Kudo, H. Kato, "Photocatalytic decomposition of water into H₂ and O₂ over novel photocatalyst K₃Ta₃Si₂O₁₃ with pillared structure consisting of three TaO₆ chains." *Chem. Lett.*, 867, (1997).
- [30] H. Kato, A. Kudo, "Water Splitting into H₂ and O₂ on Alkali Tantalate Photocatalysts ATaO₃ (A = Li, Na, and K)." *J. Phys. Chem. B*, **105**, 4285, (2001).
- [31] H. Kato, K. Asakura, and A. Kudo, "Highly Efficient Water Splitting into H₂ and O₂ over Lanthanum-Doped NaTaO₃ Photocatalysts with High Crystallinity and Surface Nanostructure." *J. Am. Chem. Soc.*, **125**, 3082, (2003).
- [32] S. Ikeda, T. Itani, K. Nango, and M. Matsumura, "Overall Water Splitting on Tungsten-Based Photocatalysts with Defect Pyrochlore Structure." *Catal. Lett.*, **98**, 229, (2004).
- [33] K. Ikarashi, J. Sato, H. Kobayashi, N. Saito, H. Nishiyama, and Y. Inoue, "Photocatalysis for water decomposition by RuO₂-dispersed ZnGa₂O₄ with d10 configuration." *J. Phys. Chem. B*, **106**, 9048, (2002).
- [34] J. Sato, N. Saito, H. Nishiyama, and Y. Inoue, "Photocatalytic Activity for Water Decomposition of Indates with Octahedrally Coordinated d10 Configuration. I. Influences of Preparation Conditions on Activity." *J. Phys. Chem. B*, **107**, 7965, (2003).

- [35] J. Sato, H. Kobayashi, K. Ikarashi, N. Saito, H. Nishiyama, and Y. Inoue, "Photocatalytic Activity for Water Decomposition of RuO₂-Dispersed Zn₂GeO₄ with d10 Configuration." *J. Phys. Chem. B*, **108**, 4369, (2004).
- [36] J. Sato, N. Saito, H. Nishiyama, and Y. Inoue, "New Photocatalyst Group for Water Decomposition of RuO₂-Loaded p-Block Metal (In, Sn, and Sb) Oxides with d10 Configuration." *J. Phys. Chem. B*, **105**, 6061, (2001).
- [37] A. Kudo, H. Okutomi, and H. Kato, "Photocatalytic Water Splitting into H₂ and O₂ over K₂LnTa₅O₁₅ Powder. " *Chem. Lett.*, 1212, (2000).
- [38] K. Yoshioka, V. Petrykin, M. Kakihana, H. Kato, and A. Kudo, "The relationship between photocatalytic activity and crystal structure in strontium tantalates." *J. Catal.*, **232**, 102, (2005).
- [39] A. Kudo, H. Kato, "Effect of lanthanide-doping into NaTaO₃ photocatalysts for efficient water splitting." *Chem. Phys. Lett.*, **331**, 373, (2000).
- [40] Z. Zou, J. Ye, K. Sayama, and H. Arakawa, "Direct splitting of water under visible light irradiation with an oxide semiconductor photocatalyst." *Nature (London, U. K.)*, **414**, 625, (2001).

- [41] Z. Zou, H. Arakawa, "Direct water splitting into H₂ and O₂ under visible light irradiation with a new series of mixed oxide semiconductor photocatalysts." *J. Photochem. Photobiol. , A*, **158**, 145, (2003).
- [42] H. Liu, J. Yuan, W. Shangguan, and Y. Teraoka, "Visible-light-responding BiYWO₆ solid solution for stoichiometric photocatalytic water splitting." *J. Phys. Chem. C*, **112**, 8521, (2008).
- [43] K. Maeda, K. Teramura, N. Saito, Y. Inoue, H. Kobayashi, and K. Domen, "Overall water splitting using (oxy)nitride photocatalysts." *Pure Appl. Chem.*, **78**, 2267, (2006).
- [44] Y. Lee, H. Terashima, Y. Shimodaira, K. Teramura, M. Hara, H. Kobayashi, K. Domen, and M. Yashima, "Zinc germanium oxynitride as a photocatalyst for overall water splitting under visible light." *J. Phys. Chem. C*, **111**, 1042, (2007).
- [45] W. Wei, Y. Dai, K. Yang, M. Guo, and B. Huang, "Origin of the Visible Light Absorption of GaN-Rich Ga_{1-x}Zn_xN_{1-x}O_x (x = 0.125) Solid Solution " *Journal of Physical Chemistry C*, **112**, 15915, (2008).
- [46] K. Maeda, K. Teramura, T. Takata, M. Hara, N. Saito, K. Toda, Y. Inoue, H. Kobayashi, and K. Domen, "Overall Water Splitting on (Ga_{1-x}Zn_x)(N_{1-x}O_x) Solid Solution Photocatalyst: Relationship between Physical Properties and Photocatalytic Activity." *J. Phys. Chem. B*, **109**, 20504, (2005).

- [47] K. Maeda, K. Teramura, D. Lu, T. Takata, N. Saito, Y. Inoue, and K. Domen, "Characterization of Rh-Cr Mixed-Oxide Nanoparticles Dispersed on $(\text{Ga}_{1-x}\text{Zn}_x)(\text{N}_{1-x}\text{O}_x)$ as a Cocatalyst for Visible-Light-Driven Overall Water Splitting." *J. Phys. Chem. B*, **110**, 13753, (2006).
- [48] K. Maeda, K. Teramura, D. Lu, N. Saito, Y. Inoue, and K. Domen, "Noble-metal/ Cr_2O_3 core/shell nanoparticles as a co-catalyst for photocatalytic overall water splitting." *Angew. Chem., Int. Ed.*, **45**, 7806, (2006).
- [49] K. Maeda, K. Teramura, D. Lu, N. Saito, Y. Inoue, and K. Domen, "Roles of Rh/ Cr_2O_3 (Core/Shell) Nanoparticles Photodeposited on Visible-Light-Responsive $(\text{Ga}_{1-x}\text{Zn}_x)(\text{N}_{1-x}\text{O}_x)$ Solid Solutions in Photocatalytic Overall Water Splitting." *J. Phys. Chem. C*, **111**, 7554, (2007).
- [50] K. Maeda, K. Teramura, and K. Domen, "Effect of post-calcination on photocatalytic activity of $(\text{Ga}_{1-x}\text{Zn}_x)(\text{N}_{1-x}\text{O}_x)$ solid solution for overall water splitting under visible light." *J. Catal.*, **254**, 198, (2008).
- [51] R. Abe, "Development of a New System for Photocatalytic Water Splitting into H_2 and O_2 under Visible Light Irradiation," *Bull. Chem. Soc. Jpn.*, **84**, 1000, (2011).
- [52] H. Kato, M. Hori, R. Kato, Y. Shimodaira, and A. Kudo, "Construction of Z-scheme type heterogeneous photocatalysis systems for water splitting into H_2 and O_2 under visible light irradiation." *Chem. Lett.*, **33**, 1348, (2004).

- [53] M. Higashi, R. Abe, A. Ishikawa, T. Takata, B. Ohtani, and K. Domen, "Z-scheme overall water splitting on modified-TaON photocatalysts under visible light ($\lambda < 500$ nm)." *Chem. Lett.*, **37**, 138, (2008).
- [54] R. Abe, T. Takata, H. Sugihara, and K. Domen, "Photocatalytic overall water splitting under visible light by TaON and WO₃ with an IO₃⁻/I⁻ shuttle redox mediator." *Chem. Commun. (Cambridge, U. K.)*, 3829, (2005).
- [55] K. Maeda, M. Higashi, D. Lu, R. Abe, and K. Domen, "Efficient Nonsacrificial Water Splitting through Two-Step Photoexcitation by Visible Light using a Modified Oxynitride as a Hydrogen Evolution Photocatalyst." *Zhonghua Jiaoyan Yixue Zazhi*, **32**, 5858, (2009).
- [56] A. Kudo, "Development of photocatalyst materials for water splitting." *Int. J. Hydrogen Energy*, **31**, 197, (2006).
- [57] I. Tsuji, H. Kato, and A. Kudo, "Visible-Light-Induced H₂ Evolution from an Aqueous Solution Containing Sulfide and Sulfite over a ZnS-CuInS₂-AgInS₂ Solid-Solution Photocatalyst " *Angewandte Chemie International Edition*, **44**, 3565, (2005).
- [58] I. Tsuji, H. Kato, and A. Kudo, "Photocatalytic Hydrogen Evolution on ZnS-CuInS₂-AgInS₂Solid Solution Photocatalysts with Wide Visible Light Absorption Bands " *Chemistry of Materials*, **18**, 1969, (2006).

- [59] D. Herein, "X-Ray Powder Diffraction" in: , *Handbook of Heterogeneous Catalysis*, 2008, p. 765-774.
- [60] D.C. Koningsberger, D.E. Ramaker, "Applications of X-ray Absorption Spectroscopy in Heterogeneous Catalysis: EXAFS, Atomic XAFS, and Delta XANES" in: , *Handbook of Heterogeneous Catalysis*, 2008, p. 774-803.
- [61] S.R. Bare, T. Ressler, "Advances in Catalysis Volume 52; Chapter 6 Characterization of Catalysts in Reactive Atmospheres by X-ray Absorption Spectroscopy " **52**, 339, (2009).
- [62] J.W. Niemantsverdriet (Ed.), *Spectroscopy in Catalysis*, Wiley-VCH:Weinheim, 2000.
- [63] A.K. Datye, P.L. Hansen, S. Helveg, "Electron Microscopy and Diffraction" in: , *Handbook of Heterogeneous Catalysis*, 2008, p. 803-833.
- [64] W. Zhou, E.I. Ross-Medgaarden, W.V. Knowles, M.S. Wong, I.E. Wachs, and C.J. Kiely, "Identification of active Zr-WO_x clusters on a ZrO₂ support for solid acid catalysts." *Nat. Chem.*, **1**, 722, (2009).
- [65] T. Burgi, A. Baiker, "Attenuated total reflection infrared spectroscopy of solid catalysts functioning in the presence of liquid-phase reactants." *Adv. Catal.*, **50**, 227, (2006).

- [66] B.L. Mojet, S.D. Ebbesen, and L. Lefferts, "Light at the interface: the potential of attenuated total reflection infrared spectroscopy for understanding heterogeneous catalysis in water " *Chem. Soc. Rev.*, **39**, 4643, (2010).
- [67] J. Andanson, A. Baiker, "Exploring catalytic solid/liquid interfaces by in situ attenuated total reflection infrared spectroscopy " *Chem. Soc. Rev.*, **39**, 4571, (2010).
- [68] R. Nakamura, Y. Nakato, "Primary Intermediates of Oxygen Photoevolution Reaction on TiO₂ (Rutile) Particles, Revealed by in Situ FTIR Absorption and Photoluminescence Measurements." *J. Am. Chem. Soc.*, **126**, 1290, (2004).
- [69] H. Kato, A. Kudo, "Photocatalytic water splitting into H₂ and O₂ over various tantalate photocatalysts." *Catal. Today*, **78**, 561, (2003).
- [70] H. Kato, A. Kudo, "Highly efficient decomposition of pure water into H₂ and O₂ over NaTaO₃ photocatalysts." *Catal. Lett.*, **58**, 153, (1999).
- [71] I.E. Wachs, K. Routray, "Catalysis Science of Bulk Mixed Oxides" *ACS Catalysis*, **2**, 1235, (2012).
- [72] S.V. Merzlikin, N.N. Tolkachev, L.E. Briand, T. Strunskus, C. Woll, I.E. Wachs, and W. Grunert, "Anomalous Surface Compositions of Stoichiometric Mixed Oxide Compounds" *Angew. Chem. Int. Ed Engl.*, **49**, 8037-8041, (2010).

- [73] I.E. Wachs, C.A. Roberts, "Monitoring surface metal oxide catalytic active sites with Raman spectroscopy" *Chem. Soc. Rev.*, **39**, 5002-5017, (2010).
- [74] M. Anpo, P.V. Kamat (Eds.), *Environmentally Benign Photocatalysts: Applications of Titanium Oxide-based Materials*, Springer:New York, 2010.
- [75] P. Kubelka, F. Munk, *Z. Tech. Phys.*, **12**, 593, (1931).
- [76] X. Gao, I.E. Wachs, "Investigation of Surface Structures of Supported Vanadium Oxide Catalysts by UV-vis-NIR Diffuse Reflectance Spectroscopy." *J. Phys. Chem. B*, **104**, 1261, (2000).
- [77] W.N. Delgass (Ed.), *Spectroscopy in heterogeneous catalysis*, Academic Press:New York, 1979.
- [78] Z. Sojka, F. Bozon-Verduraz, M. Che, "UV-Vis-NIR and EPR Spectroscopies" in: *Handbook of Heterogeneous Catalysis*, 2008, p. 1039-1065.
- [79] F.C. Jentoft, "Advances in Catalysis Volume 52; Chapter 3 Ultraviolet–Visible–Near Infrared Spectroscopy in Catalysis " **52**, 129 , (2009).
- [80] G.D. Gilliland, "Photoluminescence spectroscopy of crystalline semiconductors" *Materials Science and Engineering: R: Reports*, **18**, 99, (1997).

- [81] M. Anpo, S. Dzwigaj, and M. Che, "Advances in Catalysis Volume 52; Chapter 1 Applications of Photoluminescence Spectroscopy to the Investigation of Oxide-Containing Catalysts in the Working State" **52**, 1, (2009).
- [82] M. Matsuoka, T. Kamegawa, M. Anpo, "Photoluminescence Spectroscopy and Its Application to the Characterization of Active Sites and Reaction Dynamics in Catalysis" in: ,*Handbook of Heterogeneous Catalysis*, 2008, p. 1065-1073.
- [83] B.J. Selby, T.I. Quickenden, and C.G. Freeman, "The Fitting of Luminescence Rises and Decays," *Kinetics and Catalysis*, 44, 5-15, (2003).
- [84] T.I. Quickenden, T.A. Green, and D. Lennon, "Luminescence from UV-Irradiated Amorphous H₂O Ice " *J. Phys. Chem.*, **100**, 16801, (1996).
- [85] J. Tang, J.R. Durrant, and D.R. Klug, "Mechanism of photocatalytic water splitting in TiO₂. Reaction of water with photoholes, importance of charge carrier dynamics, and evidence for four-hole chemistry " *J. Am. Chem. Soc.*, **130**, 13885, (2008).
- [86] C.A. Roberts, A.A. Puretsky, S.P. Phivilay, and I.E. Wachs, "Determination of a Structure-Photocatalytic Relationship for Water Splitting on Well-Defined TiO₂ Nanodomains," *In preparation for publication*.

- [87] J.F. Moulder (Ed.), *Handbook of x-ray photoelectron spectroscopy : a reference book of standard spectra for identification and interpretation of XPS data*, Perkin-Elmer Corporation:Eden Prairie, 1992.
- [88] H. BRONGERSMA, M. DRAXLER, M. DERIDDER, and P. BAUER, "Surface composition analysis by low-energy ion scattering " *Surface Science Reports*, **62**, 63, (2007).
- [89] H.R.J. ter Veen, T. Kim, I.E. Wachs, and H.H. Brongersma, "Applications of High Sensitivity-Low Energy Ion Scattering (HS-LEIS) in heterogeneous catalysis." *Catal. Today*, **140**, 197, (2009).
- [90] J.A. Kilner, S.J. Skinner, and H.H. Brongersma, "The isotope exchange depth profiling (IEDP) technique using SIMS and LEIS " *Journal of Solid State Electrochemistry*, **15**, 861, (2011).

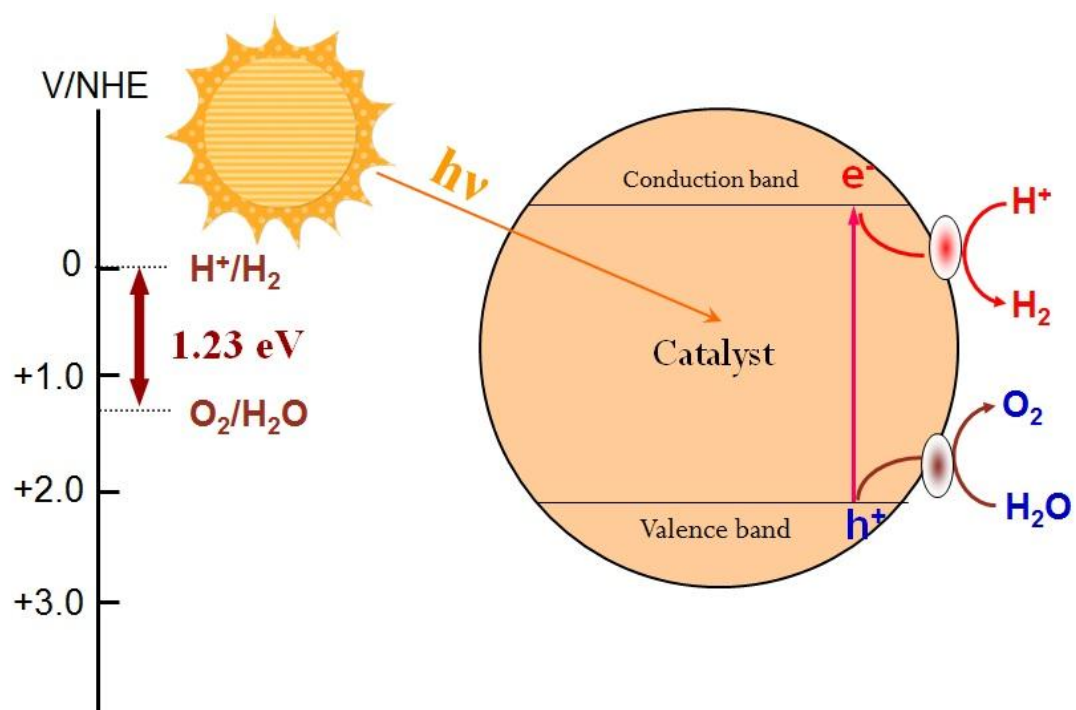


Figure 1.1: Basic Principles of Photocatalytic Water Splitting.

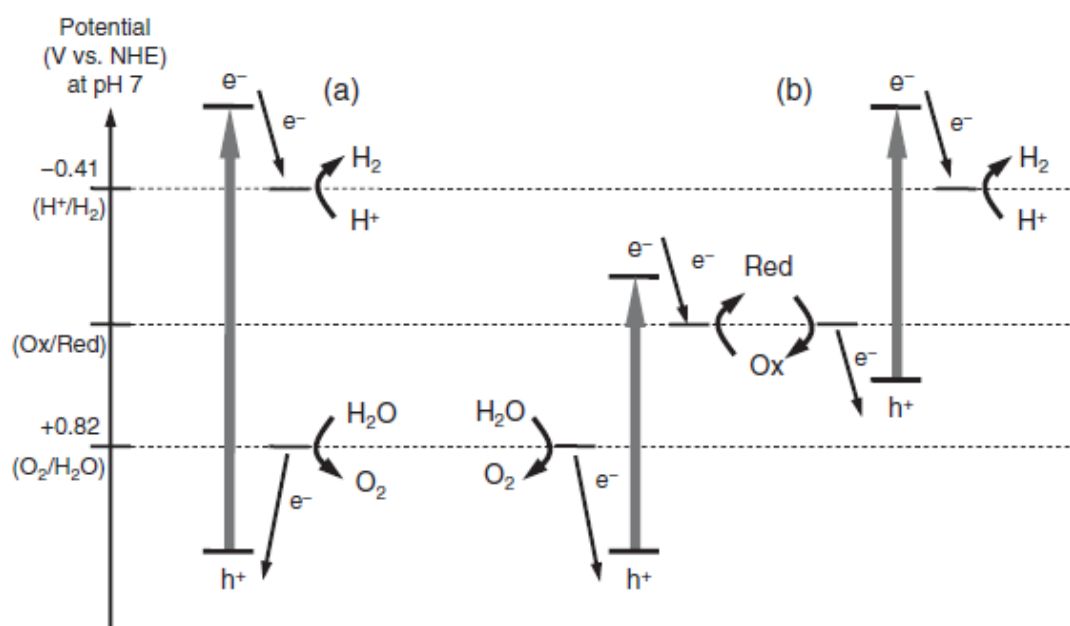


Figure 1.2: Schematic Energy Diagram of photocatalytic water-splitting systems: (a) conventional one-step system and (b) two-step “Z-Scheme” system obtained from [51].

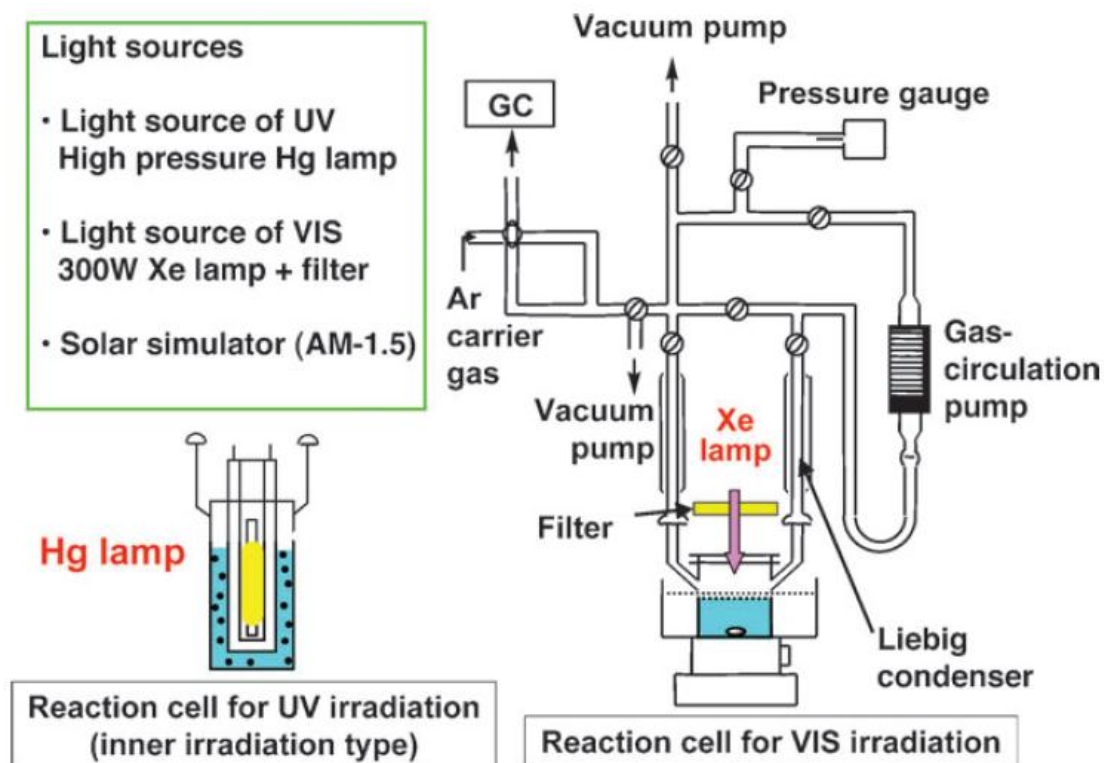


Figure 1.3: Schematic of Photocatalytic Reactor Designs obtained from [13].

CHAPTER 2

Nature of Catalytic Active Sites Present on the Surface of Advanced Bulk Tantalum Mixed Oxide Photocatalysts

Abstract

The most active photocatalyst system for water splitting under UV irradiation (270 nm) is the promoted 0.2%NiO/NaTaO₃:2%La photocatalyst with optimized apparent quantum efficiency (Q.E.) of 56%. The promoted NaTaO₃:2%La phase was synthesized by solid-state reaction between Ta₂O₅, NaCO₃ and La₂O₃ at extremely high temperatures (1120-1470 K) and the NiO promoter was subsequently impregnated from an aqueous Ni(NO₃)₂*6H₂O solution and mildly calcined at 540 K. Raman spectroscopy revealed the bulk molecular structure of NaTaO₃ was not modified by the addition of the La₂O₃ and NiO promoters. UV-vis spectroscopy showed that the bulk band gap energy was likewise not significantly affected by the addition of La₂O₃ and NiO in agreement with the same bulk structure for all the photocatalysts. The surface area of the NaTaO₃ phase is enhanced by ~10 for the La-containing catalysts and not altered for the NiO containing catalysts. HR-XPS and HS-LEIS spectroscopy indicate that the NiO and La₂O₃ promoters are surface

segregated on the bulk NaTaO₃ phase. Photoluminescence (PL) spectroscopy reveals that the addition of La₂O₃ and NiO act as electron traps resulting in the suppression of the PL emission intensity. The greater number of electron traps for the La-containing NaTaO₃ is strictly related to the enhanced surface area of this photocatalyst and the enhanced number of electron traps for the NiO-containing NaTaO₃ is an electronic effect since the surface area of this material was not altered by the addition of NiO. Consequently, the specific photoactivity of the NiO-containing NaTaO₃ catalysts, when normalized per unit surface area, is enhanced by a factor of $\sim 10^1$ - 10^2 because of the electronic promotion of NiO. These insights provide new fundamental molecular/electronic structure-photoactivity relationships about the promoted NaTaO₃ photocatalysts and the important role of surface catalytic active sites. These new findings also bring into question the validity of the previously proposed model for the catalytic active sites for the promoted 0.2%NiO/NaTaO₃:2%La photocatalyst system.

2.1 Introduction

Photocatalytic water splitting is a thermodynamically challenging reaction requiring a large positive change in Gibbs free energy (238 kJ/mol) to produce hydrogen fuel and oxygen. This phenomenon was first brought to attention by the pioneering work by Fujishima and Honda in 1972 [1] and research efforts since then have focused on finding highly active metal oxide semiconductor materials for photocatalytic hydrogen production by water splitting. Hydrogen is considered to be one of the potential candidates to replace fossil fuel for our sustainable energy needs

especially if it can be generated from the photocatalytic conversion of cheap abundant water into clean non-carbon hydrogen from solar energy resources. Development of this clean, renewable form of energy will help to address our reliance on depleted fossil fuel supplies and the environmental problems accompanying its use. Many metal oxide semiconductor catalysts (>130) have been found which are able to photocatalytically convert water into hydrogen and oxygen [2-5]. These semiconductor catalysts are based on d^0 (Ti, Zr, Nb, Ta, and W) transition metal oxides and based on d^{10} (Ga, In, Ge, Sn and Sb) main group metal oxides have emerged as candidates for use in heterogeneous photocatalytic systems because of their advantageous electronic configuration. Although photocatalytic water splitting has garnered much interest in academia, there has not been much industrial interest for photocatalytic water splitting due to the low photocatalytic activity and lack of extensive studies on industrial scale up for the process [5]. Among the discovered semiconductor photocatalyst systems, tantalum-based photocatalysts such as Ta_2O_5 [6, 7], $NaTaO_3$ [8], $K_3Ta_3Si_2O_{13}$ [9], $SrTa_2O_6$ [10] and $NaTaO_3:La$ [11, 12] have been found to be among the most promising for photocatalytic water splitting due to their high photoactivity under UV irradiation.

Some of the strategies that are used to increase the activity of the photocatalysts include the addition of a co-catalyst such as NiO, Pt, Rh_2O_3 , and RuO_2 and doping of the photocatalysts with metal ions to induce changes in morphology [13]. These catalyst design strategies led towards the discovery of lanthanum-doped $NaTaO_3$ loaded with a NiO co-catalyst ($NiO/NaTaO_3:La$) which is currently the most

active photocatalyst for water splitting with an optimized apparent quantum efficiency (Q.E.) of 56% under UV irradiation at 270 nm with a stability of more than 400 hours [11]. Bulk characterization techniques (XRD, TEM, XANES and EXAFS) suggested that LaO_x and NiO species are present as highly dispersed species on the surface of the catalysts because separate crystalline phases of NiO and LaO_x were not detected. Electron microscopy revealed that the particle size of $\text{NaTaO}_3\text{:La}$ (0.1-0.7 μm) were smaller than undoped, La-free NaTaO_3 (2-3 μm) and ordered nanostep structures were found only on $\text{NaTaO}_3\text{:La}$ [11]. It was proposed that the active site for H_2 evolution was at highly dispersed NiO sites selectively deposited on the edges of the nanostep structures while the active site for O_2 evolution was at the groove of the nanostep structures. The high photoactivity of the catalysts was attributed to the separation between the oxidative and reductive active sites. Deriving a model for the catalytic active surface sites based only on bulk techniques is highly problematic since the surface of bulk mixed metal oxides can be surface enriched or depleted of one or more of its constituent components [14, 15]. Thus, it is necessary to understand the nature of the outermost surface layer of a photocatalyst since the catalytic processes producing the H_2 and O_2 proceed through catalytic surface phenomena. This fundamental piece of information is critical to develop solid fundamental photocatalytic models involving the catalytic active surface sites.

The current study will utilize *in situ* optical spectroscopic characterization methods (Raman, UV-vis, photoluminescence (PL) and time-resolved picosecond PL-

Raman) to give further insight into the bulk molecular and electronic structure of NaTaO₃ photocatalysts and how the addition of NiO and La₂O₃ phases affect those bulk properties. The use of the surface science characterization methods of high-resolution X-ray photoelectron spectroscopy (HR-XPS) and high-sensitivity low energy ion scattering (HS-LEIS) spectroscopy will provide additional information about the nature of the surface region (~1-3 nm) and outermost atomic layer (~0.3 nm) of the photocatalysts where the catalytic active sites are located, respectively. This is the first study to report on the surface nature of tantalum mixed oxide photocatalysts. The objectives of this study are to establish (i) fundamental structure-photoactivity relationship for the highly active tantalum-based photocatalysts and (ii) to examine the roles of the surface and bulk characteristics of mixed oxide photocatalysts for water splitting.

2.2. Experimental

2.2.1 Photocatalyst Synthesis

The NaTaO₃ and the doped NaTaO₃:La photocatalysts were synthesized by solid-state reactions [11]. Ta₂O₅ (HC Starck, ceramic grade), Na₂CO₃ (Aldrich, 99.5%), and La₂O₃ (Alfa Aesar, 99.99%) were mixed together and calcined at 1170 K for 1 hour in air followed by intermediate grinding at ambient temperatures and then calcined in air at 1420 K for 10 hours. The molar ratio of Na:La:Ta was = 1-X:X:1, with an excess amount of sodium (5% mol) used to compensate for Na volatilization. The optimized doping of 2 mol% of lanthanum was used in this study. The NiO (0.2

wt. %) was subsequently added to the photocatalyst by impregnation of an aqueous solution of $\text{Ni}(\text{NO}_3)_2 \cdot 6\text{H}_2\text{O}$ (Aldrich, 99.999%). The powdered photocatalyst was placed into a porcelain crucible and heated over a water bath and the suspension was stirred using a glass rod until the solution was completely evaporated. The dried powder was then mildly calcined at 540 K for in air for 1 hour.

2.2.2 *In Situ* Raman Spectroscopy

The Raman spectra of the photocatalysts were obtained on a Lab Ram-HR Raman spectrometer (Horiba-Jobin Yvon) equipped with visible (532 nm) laser excitation utilizing a confocal microscope (Olympus BX-30) for focusing the laser on the catalyst sample. The visible laser excitation was generated by Nd:YAG laser (10 mW) with the scattered photons directed into a single monochromator and focused onto a UV-sensitive liquid- N_2 cooled CCD detector (Horiba-Jobin Yvon CCD-3000V) having a spectral resolution of $\sim 2 \text{ cm}^{-1}$ for the given parameters. About 5-10 mg of the catalyst was placed into a high temperature *in situ* cell (Linkam TS-1500) with a quartz window and cooled with flowing water. The catalyst samples were treated at 673 K for 1 h in flowing 10% O_2/He (Airgas, 30 mL/min) to desorb the adsorbed moisture and the spectra of the dehydrated samples were collected after cooling the catalysts back to 373 K in the flowing 10% O_2/He gas to ensure that the catalyst surface was void of moisture. The spectral acquisition time employed was 5 scans of 5 seconds/scan for each spectrum. System alignment was verified using a silica reference standard line at 520.7 cm^{-1} .

2.2.3 *In Situ* UV-Vis Diffuse Reflectance Spectroscopy

The UV-Vis Diffuse Reflectance spectra were obtained using a Varian Cary 5E UV-vis spectrophotometer with a diffuse reflectance attachment (Harrick Praying Mantis Attachment, DRA-2). The finely ground powder catalyst samples (~20 mg) were loaded into an *in situ* cell (Harrick, HVC-DR2) and measured in the 200-800 nm spectral region with a magnesium oxide reflectance standard used as the baseline. The UV-vis spectra of the photocatalysts were obtained after the samples were treated at 673 K for 1 h in flowing 10% O₂/He (Airgas, 30 mL/min) to desorb the adsorbed moisture. Below 300 nm, the absorbance signal was unacceptably noisy and a filter (Varian, 1.5 ABS) was employed to minimize the background noise. Determination of the Kubelka-Munk function, $F(R_{\infty})$, was obtained from the UV-vis DRS absorbance and processed with Microsoft Excel software. The UV-vis edge energy (E_g) was determined by finding the intercept of the straight line in the low-energy rise of a plot of $[F(R_{\infty})hv]^{1/n}$, where $n = 0.5$ for the direct allowed transition versus hv , where hv is the energy of the incident photon [16-18].

2.2.4 Photoluminescence Spectroscopy and Lifetime Emissions Decay

Photoluminescence spectra and lifetime emissions decay were obtained using a tunable Ti:sapphire laser (Mira 900, Coherent), generating 5 ps pulses with 76 MHz repetition rate and pumped with a frequency-doubled Nd:YVO₄ laser (Coherent Verdi V-18), set at 267 nm and was directed into a tunable Raman/photoluminescence system (Jobin Yvon Horiba, T64000) with UV objective lens to focus the laser onto

the sample. About 5-10 mg of the catalyst sample was placed into a high temperature *in situ* cell (Linkam TS-1500) with a quartz window and cooled with flowing water. The cell was pretreated at 673 K by flowing 10% O₂/N₂ for 30 minutes to desorb adsorbed moisture and then cooled back down to 298 K in flowing N₂ where the photoluminescence spectrum was obtained. The emission spectrum was collected in the 366-700 nm range. The peak of the photoluminescence spectrum was then subsequently used as the emissions decay window for photoluminescence lifetime measurements. For lifetime decay experiments, the luminescence light was subsequently backscattered through the objective lenses and focused onto a slit of a triple-monochromator equipped with a fast gated intensified charge coupled device (ICCD) camera (Picostar HR12, LaVision). The gate width was set to 500 ps and the maximum delay was determined by the repetition rate of the Ti:sapphire laser, ~13200 ps. The laser energy at the sample was maintained at approximately 20 mW to prevent laser-induced sample damage. The experimental decay curves were first fitted to a simple first order exponential decay model:

$$y = A1 \cdot \exp\left(\frac{-t}{t1}\right) + y0 \quad (1)$$

A double first order exponential decay “biexponential” model was also used to account for the case where the photoluminescence decay can be described to the decay of two different excited species back to their ground states independent of one another [19, 20]:

$$y = A1 \cdot \exp\left(\frac{-t}{t1}\right) + A2 \cdot \exp\left(\frac{-t}{t2}\right) + y0 \quad (2)$$

2.2.5 High Resolution X-ray Photoelectron Spectroscopy (HR-XPS)

The HR-XPS spectra of the catalysts were obtained on a Scienta ESCA 300 spectrometer equipped with a 300 mm hemispherical electrostatic analyzer and a monochromatic Al K α X-ray source with energy of 1486.6 eV generated from a rotating anode. This allows for improved chemical selectivity by narrowing the spectral peaks of elements and greatly reducing the spectral background signal compared to conventional XPS spectrometers. Each spectrum was calibrated using a binding energy (BE) value of 285.0 eV for carbon in the C1s region. The atomic concentration ratios were calculated by correcting the measured peak area ratios with relative sensitivity factors employed in the Casa XPS software version 2.3.15

2.2.6 High Sensitivity Low Energy Ion Scattering (HS-LEIS) Spectroscopy

Analysis of the outermost surface layer of the photocatalysts was obtained with the Qtac¹⁰⁰ HS-LEIS Spectrometer (ION-TOF) equipped with a highly sensitive double toroidal analyzer, 3000 times higher sensitivity than conventional LEIS spectrometers, which allows for static depth profiling. The photocatalyst samples were first gently cleaned with atomic oxygen to remove surface hydrocarbon contamination from the atmosphere prior to being transferred inside the analysis chamber. The HS-LEIS spectra were collected using both 3000 eV He⁺ with a 8600 pA current and 4000 eV Ne⁺ with a 2830 pA current as ion sources. For depth

profiling, the surface was sputtered by Ar⁺ gas at 1000 eV at a sputter yield of 1x10¹⁵ ions/cm².

2.3 Results

2.3.1 *In Situ* Raman Spectroscopy

The *in situ* Raman spectra of the tantalum-based photocatalysts are shown in Figure 1. The Raman bands of the bulk Ta₂O₅ are indicative of the crystalline Ta₂O₅ (L) phase [21]. The largest band in the spectrum for the Ta₂O₅ (L) phase is at 100 cm⁻¹ originating from a lattice photon mode along with the band at 199 cm⁻¹. The Raman bands at 256 and 338 cm⁻¹ have been assigned to Ta-O-Ta and TaO₆ bending modes, respectively. The bands at 489, 631, 708 and 848 cm⁻¹ are assigned to Ta-O-Ta symmetric stretching, Ta-O symmetric stretching, Ta-O-Ta antisymmetric stretching and higher order Ta-O symmetric stretching modes, respectively.

The solid state synthesis between Na₂CO₃ and Ta₂O₅ greatly changes the bulk crystal structure of the photocatalyst and the Raman spectrum for the undoped NaTaO₃ photocatalyst is shown in Figure 1. The unmodified NaTaO₃ contains Raman bands at 133, 152, 195 and 213 cm⁻¹ that can be assigned to Na translational vibration modes [22]. The bands at 261 and 313 cm⁻¹ are assignable to bending modes for TaO₆ and the bands at 451, 498, and 629 cm⁻¹ are assignable to Ta-O stretching modes. The doping of La into the NaTaO₃ does not result in any apparent changes to the NaTaO₃ Raman spectrum, which suggests that La doping did not significantly perturb the bulk NaTaO₃ structure. Crystalline La₂O₃ bands expected at 104, 191 and 411 cm⁻¹ are not

present [23] indicating that La_2O_3 is present as an amorphous phase in the NaTaO_3 photocatalyst. The crystalline NiO broad overlapping bands at 460 and 500 cm^{-1} are not detected either because of their relatively weak Raman bands [24] or the presence of dispersed NiO species. Thus, the bulk molecular structure of NaTaO_3 is not affected by the addition of the lanthanum and nickel oxide dopants.

2.3.2 UV-Vis Diffuse Reflectance Spectroscopy

The UV-Vis DRS E_g values for the tantalum-based photocatalysts are given in Table 1. The bulk band gap energies are comparable for all the tantalum-based photocatalysts and are in agreement with previously reported E_g values in the literature [7, 11]. The addition of La_2O_3 and NiO does not have much of an effect on the band gap energy for the NaTaO_3 reflecting the dominant contribution of the NaTaO_3 component.

2.3.3 Photoluminescence Spectroscopy and PL lifetime decay

The photoluminescence emission spectra at 267 nm excitation for the tantalum-based photocatalysts are presented in Figure 2. The bulk Ta_2O_5 photocatalyst exhibits a very intense and broad peak with a peak maximum at 525 nm. The intensity of PL emissions spectra can give information on the crystallinity of the Ta_2O_5 and NaTaO_3 [25]. The strong PL emission spectrum indicates the presence of electron/hole recombination sites in Ta_2O_5 such as defect sites. In contrast, the undoped NaTaO_3 PL spectrum is much broader and the peak intensity is significantly suppressed reflecting a more ordered crystalline structure with less defect sites. The addition of La_2O_3 and NiO to the NaTaO_3 results in further suppression of the

photoluminescence emission intensity suggesting that these dopants further decrease the concentration of defect sites.

The photoluminescence decay curves for the tantalum photocatalysts are plotted in Figure 3. Equation 1 and Equation 2 were used to model emissions decay for the tantalum-based photocatalysts and the fit parameters are given in Table 2. The bulk Ta_2O_5 photocatalyst was found to fit the simple first order exponential decay model while the NaTaO_3 photocatalysts fit the biexponential model. The observed simple first-order exponential decay model for the bulk Ta_2O_5 catalyst can be attributed to the homogeneity of this bulk catalysts, where the emission decay is dominated by only one type of excited tantalum species decaying back to the ground state [19]. This single species decay is not seen in the NaTaO_3 photocatalysts where multiple excited species exist and decay back to their ground states independently of each other. Two different regimes in the decay curves can be observed for the NaTaO_3 photocatalysts that are identified as the “fast” component of decay, which dominates at early decay times, and the “slow” component of the decay, which dominate at later decay times. The parameters t_1 and t_2 refer to the decay constants for the “fast” and “slow” components and A_1 and A_2 refer to the amplitudes of the “fast” and “slow” components, respectively.

The PL emissions decay is related to the lifetimes of the photo-generated electron/hole pairs with slower decay rates indicative of a longer lifetime [26, 27]. The decay constant for Ta_2O_5 is on the same timescale as the NaTaO_3 photocatalysts for the “slow” component of decay. The larger decay constant, t_2 , for NaTaO_3 is

indicative of longer decay lifetimes compared to the Ta₂O₅. For modified NaTaO₃ photocatalysts, the addition of La₂O₃ and NiO leads to a subsequent decrease of the decay constant of the “fast” component (t₁) with a concurrent increase in the amplitude (A₁) of the “fast” component. Also the addition of NiO shows a decrease for the decay constant of the “slow” component (t₂) while the addition of La₂O₃ leads to an increase in the decay constant of the “slow” component (t₂).

2.3.4 High Resolution X-ray Photoelectron Spectroscopy

HR-XPS was employed to determine the elemental composition of the surface region (~1-3 nm) for the NiO/NaTaO₃:La photocatalyst. The XPS survey spectrum for the NiO/NaTaO₃:La photocatalyst is presented in Figure 4. The surface region consists primarily of Na, La, O and Ta. The main binding energy peak for nickel (Ni 2p) is not detected due to overlap with the strong La 3d binding energy peak. The appearance of the Ni LMM Auger peak confirms that Ni is indeed present in the surface region, but the amount cannot be quantified because of the overlap of the Ni 2p peak with the La 3d peak. The atomic concentrations of the elements in the surface region are tabulated in Table 3. The bulk atomic concentration for lanthanum is 0.4% and its 3.7% concentration in the surface region reveals that La is significantly surface enriched in the NiO/NaTaO₃:La photocatalyst system.

2.3.5 High Sensitivity-Low Energy Ion Scattering Spectroscopy

The atomic composition of the outermost surface layer (~0.3 nm) of the 0.2% NiO/NaTaO₃:2%La photocatalyst was determined by HS-LEIS. The HS-LEIS spectra for the outermost layer of the 0.2% NiO/NaTaO₃:2%La photocatalyst, using both He⁺

and Ne^+ ion gases, are shown in Figure 5. For the He^+ HS-LEIS spectrum, scattering from Na, O and Ni atoms with low atomic mass are detected in the topmost surface layer, but He^+ ions cannot readily distinguish between the higher atomic mass elements of La (139 amu) and Ta (181 amu). With Ne^+ ions, however, the La and Ta HS-LEIS peaks can readily be resolved and both elements are also found to be present on the topmost surface layer of the $\text{NiO}/\text{NaTaO}_3\text{:La}$ photocatalyst.

HS-LEIS depth profiling analysis of the $\text{NiO}/\text{NaTaO}_3\text{:La}$ photocatalyst was undertaken to determine its elemental composition with distance from the outermost surface and are presented in Figure 6. For the bulk components O and Na the signal is very strong for the outermost layer and increase in intensity with the depth profile while the La/Ta signal is broader in intensity but also increases with the depth profile as shown in Figure 6a. The HS-LEIS Ni peak is only present in the first few sputtering cycles of Figure 6a revealing that Ni is only present on the outermost layers of this photocatalyst. The HS-LEIS signal for the La peak in Figure 6b is initially very strong in the first few layers and decreases with sputtering reflecting its surface segregation in the $\text{NiO}/\text{NaTaO}_3\text{:La}$ photocatalyst system. The appearance of a small La peak at the end of the sputtering indicates that a small concentration of La is also present in the bulk $\text{NiO}/\text{NaTaO}_3\text{:La}$ photocatalyst. In contrast, the HS-LEIS signal for Ta is extremely small in the outermost surface layer and monotonically increases with sputtering reflecting its diminished concentration on the outermost surface and in the surface region. Unlike Ta, the HS-LEIS spectra reveal that Na is present on the

outermost surface and that its concentration increases with sputtering suggesting some surface segregation of Na in the NiO/NaTaO₃:La photocatalyst.

2.4 Discussion

2.4.1 Bulk Molecular and Electronic Structures of NaTaO₃ Photocatalysts

The bulk molecular structure of the NaTaO₃ photocatalysts is not perturbed by the addition of the La₂O₃ and NiO promoters since the pure NaTaO₃ and promoted NaTaO₃ photocatalysts exhibit the same Raman spectra of the bulk structure. The bulk electronic structure of the NaTaO₃ photocatalysts is also not perturbed by the addition of the La₂O₃ and NiO promoters since the pure NaTaO₃ and promoted NaTaO₃ photocatalysts possess essentially the same optical band gap value of ~4.1-4.2 eV. The similar bulk molecular and electronic structures of the NaTaO₃ photocatalysts suggest that the La₂O₃ and NiO promoters are minimally incorporated into the bulk NaTaO₃ lattice.

2.4.2 Surface Composition of Promoted NaTaO₃ Photocatalyst

The HS-LEIS analysis of the outermost surface layer (~0.3 nm) of the promoted NiO/NaTaO₃:La photocatalyst shows the presence of O, Na, Ta, Ni and La. HS-LEIS depth profile analysis demonstrates that both La and Ni are surface segregated in the promoted photocatalyst since their concentrations decrease during depth profiling. HR-XPS analysis indicates that the La is enriched by a factor of ~10 in the surface region (~1-3 nm) and probably much greater in the topmost surface layer. Although Na and a minor amount of Ta are present in the outermost surface

layer of the promoted $\text{NiO}/\text{NaTaO}_3\text{:La}$ photocatalyst, HS-LEIS depth profiling indicates that their concentrations are not surface enriched because the intensity of their HS-LEIS signals increase with depth profiling, especially that of Ta. The only element whose concentration remains relatively constant is O and reflects the oxide nature of the promoted $\text{NiO}/\text{NaTaO}_3\text{:La}$ photocatalyst. The surface segregation of NiO and La_2O_3 in the promoted $\text{NiO}/\text{NaTaO}_3\text{:La}$ photocatalyst is consistent with the synthesis methods employed.

The promoted $\text{NaTaO}_3\text{:La}$ photocatalyst was synthesized by the solid-state method from physically mixed Ta_2O_5 , NaCO_3 and La_2O_3 at elevated temperatures (1170-1420 K). Under these conditions, Ta_2O_5 reacts with NaCO_3 to form bulk NaTaO_3 because the molten state of basic Na at such extreme temperatures readily reacts with the acidic Ta_2O_5 [28, 29]. The molten basic Na does not have an affinity for reacting with the basic La_2O_3 and the low mobility of La_2O_3 [melting point 2588 K] at these temperatures limits the reaction between acidic Ta_2O_5 and basic La_2O_3 . Consequently, La_2O_3 is not extensively incorporated into the bulk NaTaO_3 structure and remains in the surface region and the topmost surface layer of the promoted $\text{NaTaO}_3\text{:La}$ photocatalyst. Lanthanum oxide is also well known to be a good additive for inhibiting particle sintering at high temperatures results in increased BET surface area and stabilization of small particles [30, 31]. The promotion of NaTaO_3 with La_2O_3 resulted in an increased BET surface area by a factor of ~8 (see Table 4). The NiO promoter was added by impregnation of aqueous $\text{Ni}(\text{NO}_3)_2 \cdot 6\text{H}_2\text{O}$, drying and calcination at 540 K for only 1 hour. This mild calcination treatment is not sufficient

to create a solid-state reaction between NiO and NaTaO₃:La and, consequently, Ni is also surface segregated in the promoted NaTaO₃:La photocatalyst. In summary, basic Na reacted with acidic Ta₂O₅ at the extreme calcination temperatures to form the bulk NaTaO₃ mixed oxide structure and La₂O₃ and NiO were not incorporated into the bulk NaTaO₃ and remained segregated in the surface region and topmost surface layer.

2.4.3 Bulk and Surface Structures of the Promoted NaTaO₃:La

Photocatalyst

A schematic of the bulk and surface structures of the promoted NaTaO₃:La photocatalyst is depicted in Figure 7. The NaTaO₃ bulk phase has a perovskite structure with ABO₃ stoichiometry [22]. Perovskite ABO₃ structures have been shown to be preferentially surface enriched with the A cation (Na) and surface depleted with the B cation (Ta) [29, 32, 33], which is consistent with the HS-LEIS depth profiling measurements in this study. The surface segregation of NiO and La₂O₃ is revealed by the depth profiling HS-LEIS measurements and the HR-XPS surface analyses, and indicated in the schematic of the promoted NaTaO₃:La photocatalyst.

2.4.4 Generation of Excited Electron/Hole Pairs and Their Lifetimes

The main function of the bulk NaTaO₃ mixed oxide support is to control the material's optical band gap that generates excited electron/hole pairs for the photocatalytic reactions with water taking place at the surface of the photocatalyst. The same bulk NaTaO₃ structure and optical band gap for the unpromoted and promoted NaTaO₃ photocatalysts implies that the generation of electron/hole pairs is the same for all the NaTaO₃ photocatalysts.

The recombination of excited electrons and holes is significantly affected by promotion of NaTaO₃ by the surface NiO and La₂O₃ additives as reflected by their PL spectra (see Figure 2). PL spectroscopy monitors the recombination of electrons and holes and the decrease in the intensity of the PL signal reflects the ability of surface NiO and La₂O₃ promoters to create efficient electron traps that help prevent electron/hole recombination and, thus, become available for photocatalysis [34-36]. The increase in the number of electron traps for La promoted NaTaO₃, however, is directly related to the factor of ~10 increase in surface area of this photocatalytic material. The increase in the number of electron traps with the NiO promoter reflects the photoproperties of NiO since the unpromoted and Ni-promoted photocatalyst possess the same surface area.

The decay part of the PL spectra contains information about the lifetime of the excited electrons/holes, usually reflected by the slow t₂ component, and the ratio $\frac{A_2}{A_1+A_2}$ is indicative of the relative population of these long lived electrons with slow emissions decay [26, 27]. The addition of the efficient NiO electrons traps and the higher surface area of the La-promoted NaTaO₃ also dramatically diminishes the relative contribution of the slow component of emissions decay with a greater population of electrons with fast decay lifetimes. Although it is desirable for a photocatalyst to have a greater population of long lived excited electrons with slow decay lifetimes, the trapping of the excited electrons by the surface NiO and the high

surface area allows more electrons and holes to perform photocatalysis at the oxide-water interface.

2.4.5 Structure-Activity Relationships for Splitting of H₂O by NaTaO₃ Photocatalysts

The photocatalysis community typically normalizes their activity results per gram of photocatalyst. The current findings for the promoted NaTaO₃ catalysts, however, demonstrate that the promoters are only altering the surface characteristics of the photocatalyst and suggest that the photoactivity should instead be normalized per unit surface area.

The La₂O₃ promoter has been proposed to be an electronic promoter for the NaTaO₃ photocatalyst, but when the photoactivity for NaTaO₃ and NaTaO₃:La are normalized per unit surface area the photoactivity for both of these catalysts is essentially the same (see Table 4). This indicates that La₂O₃ is not an electronic promoter, but acts as a textural promoter that enhances the BET surface area by a factor of ~10. As mentioned above, lanthanum oxide is known to be a good additive for inhibiting particle sintering at high temperatures and stabilizing high BET surface area [30, 31]. The NiO, however, is an electronic promoter since it dramatically increases the photoactivity per unit surface area by a factor of ~10¹-10² both in the presence and absence of the La₂O₃ promoter and does not affect the overall BET surface area of the photocatalyst (see Table 4).

The accepted model for the promoted NiO/NaTaO₃:La photocatalyst is that there is a synergistic interaction of NiO preferentially self-assembling at nanostep

structures created by the doped La_2O_3 [11]. This conclusion was only reached because the simultaneous addition of NiO and La_2O_3 to NaTaO_3 resulted in extremely enhanced overall photoactivity for water splitting. The current study employs the specific photoactivity values for water splitting and demonstrates that La_2O_3 is a textural promoter and only NiO is an electronic promoter with no synergistic interactions between the NiO and La_2O_3 promoters. The current study also demonstrates that it is necessary to compare specific photoactivity rates in order to fully understand the fundamental structure-activity relationships for photocatalysts.

2.5 Conclusions

The bulk and surface properties of promoted $\text{NiO}/\text{NaTaO}_3\text{:La}$ photocatalysts were investigated with bulk (Raman, UV-vis and PL) and surface (HS-LEIS and HR-XPS) spectroscopy. The bulk NaTaO_3 perovskite molecular and electronic structures are not affected by the La_2O_3 and NiO promoters, which means that the photogenerated excited electron/hole pairs are the same for all the NaTaO_3 -based photocatalysts. Both promoters are surface segregated on the NaTaO_3 particles. The La_2O_3 additive is a structural promoter that stabilizes small NaTaO_3 particles and increases the surface area by a factor of ~ 10 , but does not affect the specific photoactivity for water splitting. The higher surface area of the La_2O_3 promoted NaTaO_3 photocatalyst also increases the total number of defect sites that trap excited electrons. The NiO additive is an electronic promoter that increases the specific photoactivity for water splitting by a factor of 10^1 - 10^2 in the presence or absence of

the La_2O_3 promoter. The new findings provide fundamental insights about the photocatalysis mechanism of promoted $\text{NiO}/\text{NaTaO}_3\text{:La}$ photocatalysts by emphasizing the role of the surface catalytic active sites and the need to normalize the photoactivity per unit surface area. The accepted practice of normalizing photocatalytic performance per unit mass is not fundamentally meaningful since the splitting of water occurs at surface catalytic active sites and leads to incorrect photocatalytic models in the literature.

Acknowledgements

This research was financially supported by the Department of Energy grant: DOE-FG02-93ER14350. Special thanks goes out to Alexander Puretsky at the Center for Nanophase Materials Sciences at Oak Ridge National Laboratory for help in obtaining PL data in conjunction with User Project CNMS2008-075. Thanks to Masashi Tabata and Dr. Kazunari Domen for help in the synthesis of the NaTaO_3 catalysts. The assistance of Dr. A. Miller at Lehigh University in obtaining and interpreting the HR-XPS and HS-LEIS data is also gratefully acknowledged.

References

- [1] A. Fujishima, K. Honda, "Electrochemical photolysis of water at a semiconductor electrode." *Nature (London)*, **238**, 37, (1972).
- [2] K. Maeda, K. Domen, "New Non-Oxide Photocatalysts Designed for Overall Water Splitting under Visible Light." *J. Phys. Chem. C*, **111**, 7851, (2007).
- [3] F.E. Osterloh, "Inorganic Materials as Catalysts for Photochemical Splitting of Water." *Chem. Mater.*, **20**, 35, (2008).
- [4] A. Kudo, Y. Miseki, "Heterogeneous photocatalyst materials for water splitting." *Chem. Soc. Rev.*, **38**, 253, (2009).
- [5] X. Chen, S. Shen, L. Guo, and S.S. Mao, "Semiconductor-based Photocatalytic Hydrogen Generation " *Chem. Rev.*, **110**, 6503, (2010).
- [6] K. Sayama, H. Arakawa, "Effect of Na₂CO₃ addition on photocatalytic decomposition of liquid water over various semiconductor catalysts." *J. Photochem. Photobiol. , A*, **77**, 243, (1994).
- [7] H. Kato, A. Kudo, "New tantalate photocatalysts for water decomposition into H₂ and O₂." *Chem. Phys. Lett.*, **295**, 487, (1998).
- [8] H. Kato, A. Kudo, "Water Splitting into H₂ and O₂ on Alkali Tantalate Photocatalysts ATaO₃ (A = Li, Na, and K)." *J. Phys. Chem. B*, **105**, 4285, (2001).

- [9] A. Kudo, H. Kato, "Photocatalytic decomposition of water into H₂ and O₂ over novel photocatalyst K₃Ta₃Si₂O₁₃ with pillared structure consisting of three TaO₆ chains." *Chem. Lett.*, 867, (1997).
- [10] H. Kato, A. Kudo, "Photocatalytic Decomposition of Pure Water into H₂ and O₂ over SrTa₂O₆ Prepared by a Flux Method. " *Chem. Lett.*, 1207, (1999).
- [11] H. Kato, K. Asakura, and A. Kudo, "Highly Efficient Water Splitting into H₂ and O₂ over Lanthanum-Doped NaTaO₃ Photocatalysts with High Crystallinity and Surface Nanostructure." *J. Am. Chem. Soc.*, **125**, 3082, (2003).
- [12] A. Kudo, H. Kato, "Effect of lanthanide-doping into NaTaO₃ photocatalysts for efficient water splitting." *Chem. Phys. Lett.*, **331**, 373, (2000).
- [13] A. Kudo, H. Kato, and I. Tsuji, "Strategies for the Development of Visible-light-driven Photocatalysts for Water Splitting," *Chem. Lett.*, **33**, 1534, (2004).
- [14] S.V. Merzlikin, N.N. Tolkachev, L.E. Briand, T. Strunskus, C. Woll, I.E. Wachs, and W. Grunert, "Anomalous Surface Compositions of Stoichiometric Mixed Oxide Compounds " *Angew. Chem. Int. Ed Engl.*, **49**, 8037-8041, (2010).
- [15] I.E. Wachs, K. Routray, "Catalysis Science of Bulk Mixed Oxides " *ACS Catalysis*, **2**, 1235 <last_page> 1246, (2012).
- [16] P. Kubelka, F. Munk, *Z. Tech. Phys.*, **12**, 593, (1931).

- [17] X. Gao, I.E. Wachs, "Investigation of Surface Structures of Supported Vanadium Oxide Catalysts by UV-vis-NIR Diffuse Reflectance Spectroscopy." *J. Phys. Chem. B*, **104**, 1261, (2000).
- [18] W.N. Delgass (Ed.), *Spectroscopy in heterogeneous catalysis*, Academic Press:New York, 1979.
- [19] B.J. Selby, T.I. Quickenden, and C.G. Freeman, "The Fitting of Luminescence Rises and Decays," *Kinetics and Catalysis*, 44, 5-15, (2003) .
- [20] T.I. Quickenden, T.A. Green, and D. Lennon, "Luminescence from UV-Irradiated Amorphous H₂O Ice " *J. Phys. Chem.*, **100**, 16801, (1996).
- [21] Y. Chen, J.L.G. Fierro, T. Tanaka, and I.E. Wachs, "Supported Tantalum Oxide Catalysts: Synthesis, Physical Characterization, and Methanol Oxidation Chemical Probe Reaction," *The Journal of Physical Chemistry B*, **107**, 5243, (2003).
- [22] N.G. Teixeira, A. Dias, and R.L. Moreira, "Raman scattering study of the high temperature phase transitions of NaTaO₃," *Journal of the European Ceramic Society*, **27**, 3683, (2007).
- [23] G. Burns, F. Dacol, "Anomalous Raman spectra from La₂CuO₄ " *Physical Review B*, **41**, 4747, (1990).

- [24] S.S. Chan, I.E. Wachs, "In situ laser Raman spectroscopy of nickel oxide supported on gamma-Al₂O₃ " *Journal of Catalysis*, **103**, 224, (1987).
- [25] G.D. Gilliland, "Photoluminescence spectroscopy of crystalline semiconductors " *Materials Science and Engineering: R: Reports*, **18**, 99, (1997).
- [26] J. Tang, J.R. Durrant, and D.R. Klug, "Mechanism of photocatalytic water splitting in TiO₂. Reaction of water with photoholes, importance of charge carrier dynamics, and evidence for four-hole chemistry " *J. Am. Chem. Soc.*, **130**, 13885, (2008).
- [27] C.A. Roberts, A.A. Puretsky, S.P. Phivilay, and I.E. Wachs, "Determination of a Structure-Photocatalytic Relationship for Water Splitting on Well-Defined TiO₂ Nanodomains," *In preparation for publication*, .
- [28] H. BRONGERSMA, M. DRAXLER, M. DERIDDER, and P. BAUER, "Surface composition analysis by low-energy ion scattering " *Surface Science Reports*, **62**, 63, (2007).
- [29] J.A. Kilner, S.J. Skinner, and H.H. Brongersma, "The isotope exchange depth profiling (IEDP) technique using SIMS and LEIS " *Journal of Solid State Electrochemistry*, **15**, 86, (2011).

- [30] J.S. Church, N.W. Cant, and D.L. Trimm, "Stabilisation of aluminas by rare earth and alkaline earth ions " *Applied Catalysis A: General*, **101**, 105, (1993).
- [31] M. Ferrandon, "Hydrothermal Stabilization by Lanthanum of Mixed Metal Oxides and Noble Metal Catalysts for Volatile Organic Compound Removal " *Journal of Catalysis*, **200**, 148, (2001).
- [32] I.C. Fullarton, J.-. Jacobs, H.E. Benthem, J.A. Kilner, H.H. Brongersma, P.J. Scanlon, and B.C.H. Steele, "Study of oxygen ion transport in acceptor doped samarium cobalt oxide " *Ionics*, **1**, 51, (1995).
- [33] M. Viitanen, "Silica poisoning of oxygen membranes " *Solid State Ionics*, **150**, 223, (2002).
- [34] M. Anpo, P.V. Kamat (Eds.), *Environmentally Benign Photocatalysts: Applications of Titanium Oxide-based Materials*, Springer:New York, 2010.
- [35] C. Hu, C. Tsai, and H. Teng, "Structure Characterization and Tuning of Perovskite-Like NaTaO₃ for Applications in Photoluminescence and Photocatalysis " *J Am Ceram Soc*, **92**, 460, (2009).
- [36] C. Hu, Y. Lee, and H. Teng, "Efficient water splitting over Na_{1-x}K_xTaO₃ photocatalysts with cubic perovskite structure " *J.Mater.Chem.*, (2011).

Catalyst	E_g (eV)
Ta₂O₅	4.1
NaTaO₃	4.2
0.2% NiO/NaTaO₃	4.2
NaTaO₃: 2%La	4.2
0.2% NiO /NaTaO₃: 2%La	4.2

Table 2.1: Edge Energy Values from UV-Vis DRS.

Excitation 267 nm	$y=A1*\exp(-x/t1)+A2*\exp(-x/t2)+y0$					
Catalyst	t1 (ns) fast	A1 fast	t2 (ns) slow	A2 slow	A1/ (A1+A2)	A2/ (A1+A2)
Ta₂O₅	0	0	5	3.5	0	1.0000
NaTaO₃	0.8	186	17	3.6	0.9810	0.0190
0.2%NiO/NaTaO₃	0.5	473	10	2.8	0.9941	0.0059
NaTaO₃:2%La	0.3	27641	42	2.8	0.9999	0.0001
0.2%NiO/NaTaO₃: 2%La	0.2	1.36E+10	4	5	1.0000	0.0000

Table 2.2: Photoluminescence decay fit parameters for catalysts at 267 nm excitation.

Elemental Core Electron	% Atomic Concentration
Na 1s	10.4
Ta 4d 5/2	13.5
O 1s	72.4
La 3d 5/2	3.7
Ni 2p 3/2	0

Table 2.3: XPS surface region atomic concentration of promoted 0.2%NiO/NaTaO₃:2%La photocatalyst.

<u>Photocatalyst</u>	<u>Photoactivity</u> ($\mu\text{mol H}_2/\text{h/g}$)	<u>Surface Area (m^2/g)</u>	<u>Specific Photoactivity</u> ($\mu\text{mol H}_2/\text{h/m}^2$)
Ta₂O₅	6	4.0	1.5×10^0
1.0% NiO/Ta₂O₅	1154	4.0	2.9×10^2
NaTaO₃	170	0.4	4.3×10^2
0.5%NiO/NaTaO₃	2180	0.4	5.5×10^3
NaTaO₃:2%La	450	3.2	1.4×10^2
0.2%NiO/NaTaO₃:2%La	19800	3.2	6.2×10^3

Table 2.4: Photoactivity of Tantalum Oxide Photocatalysts for Water Splitting with UV Excitation (>270 nm) obtained from [7, 8, 11].

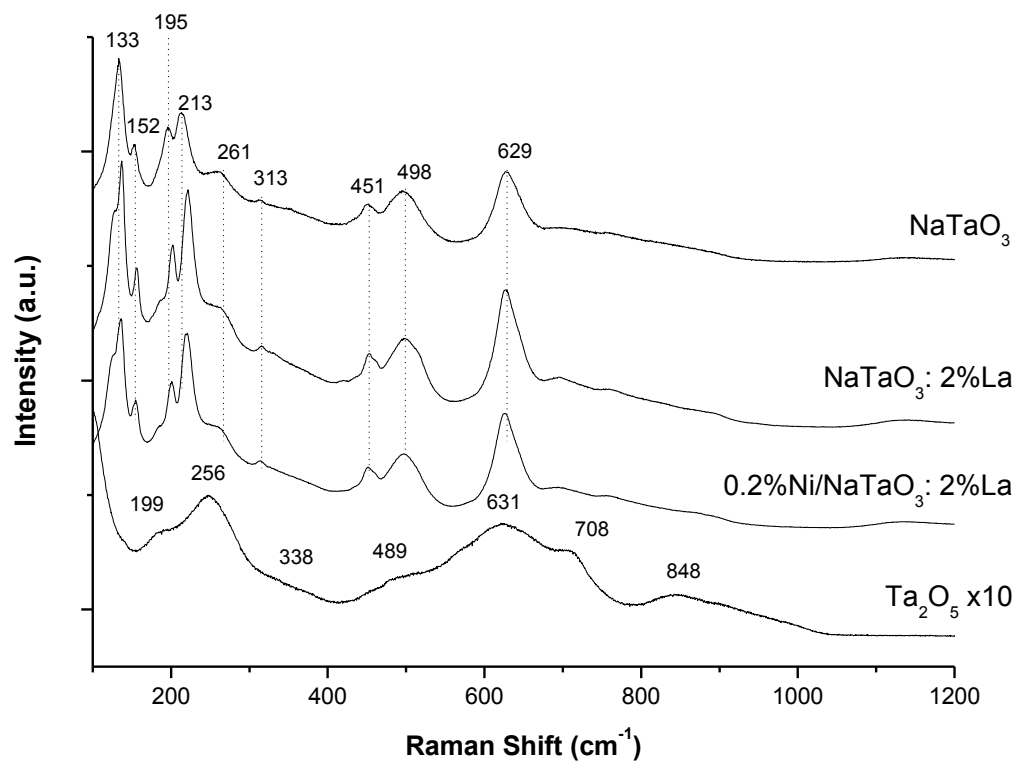


Figure 2.1: Raman Spectra of Tantalum-based Photocatalysts.

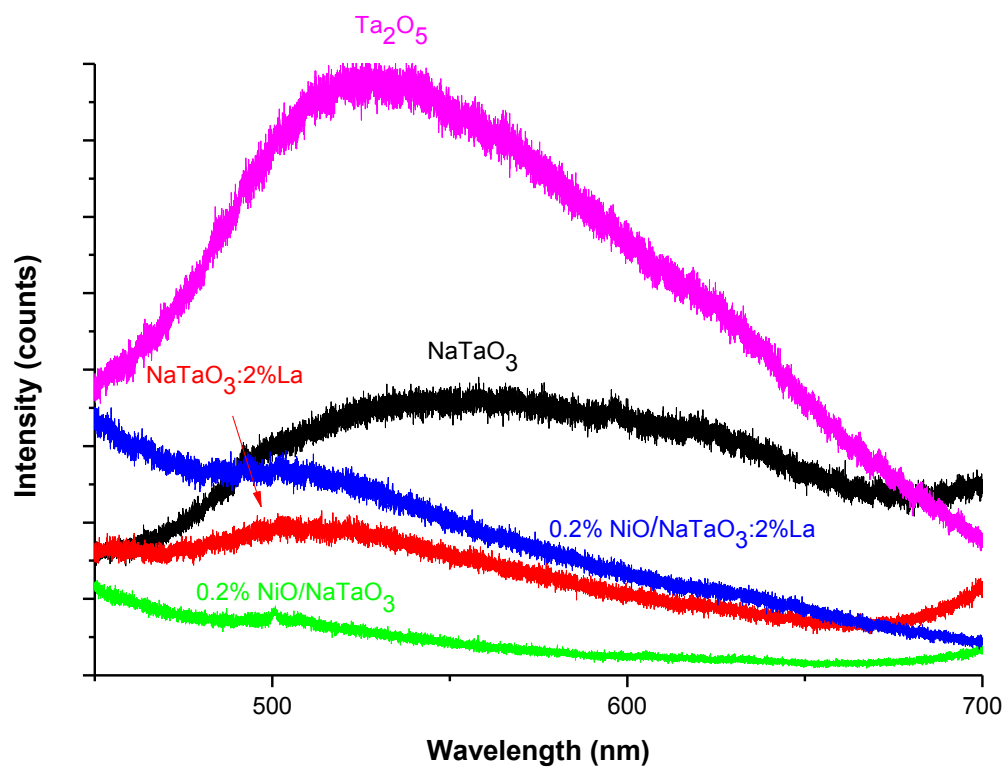


Figure 2.2: Photoluminescence Spectra at 267 nm Excitation for Tantalum-based Photocatalysts.

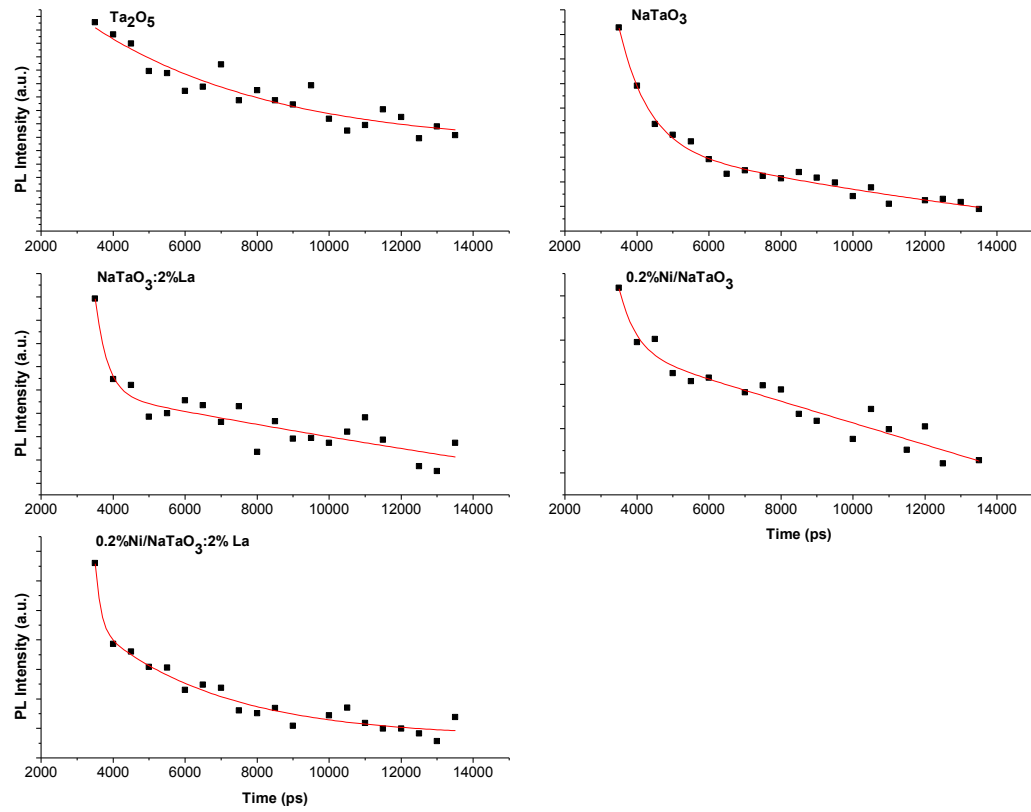


Figure 2.3: Photoluminescence Emissions Decay Curves for Tantalum-based Photocatalysts.

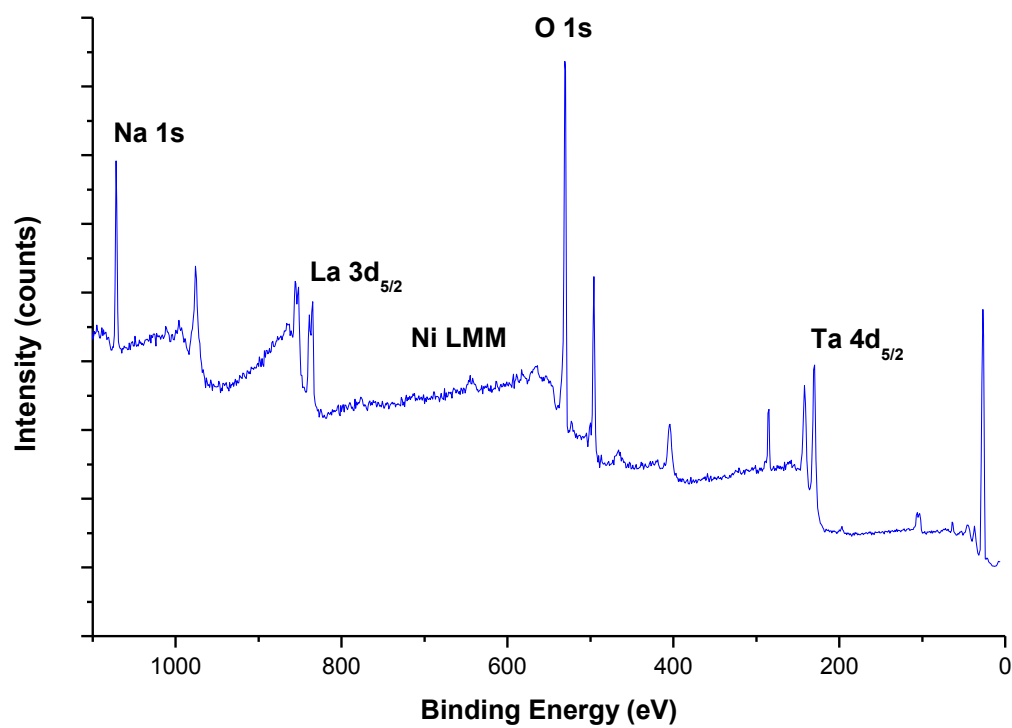


Figure 2.4: XPS survey spectrum of surface region for 0.2%NiO/NaTaO₃:2%La promoted photocatalyst.

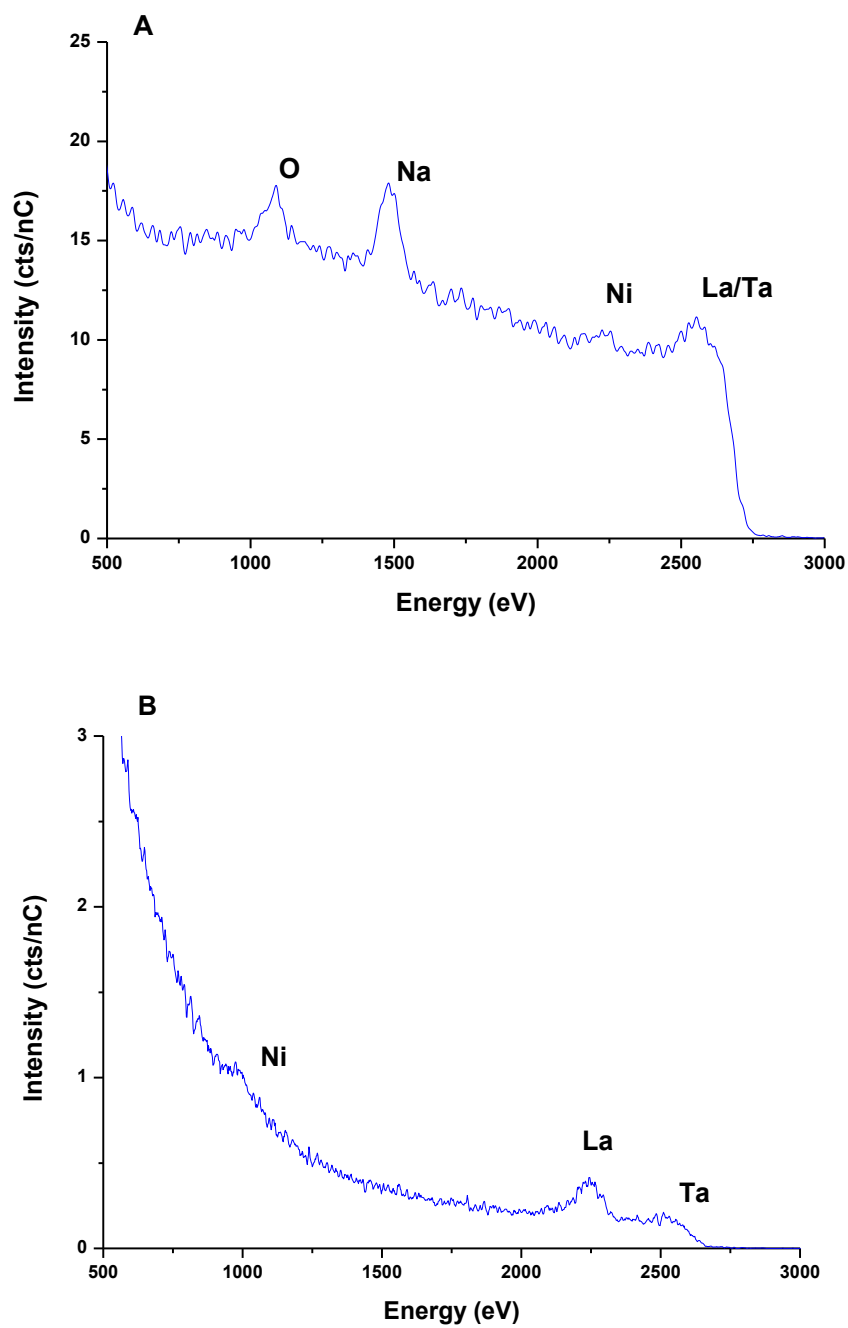


Figure 2.5: HS-LEIS spectra for 0.2%NiO/NaTaO₃:2%La promoted photocatalyst using (a) He⁺ ion gas and (b) Ne⁺ ion gas.

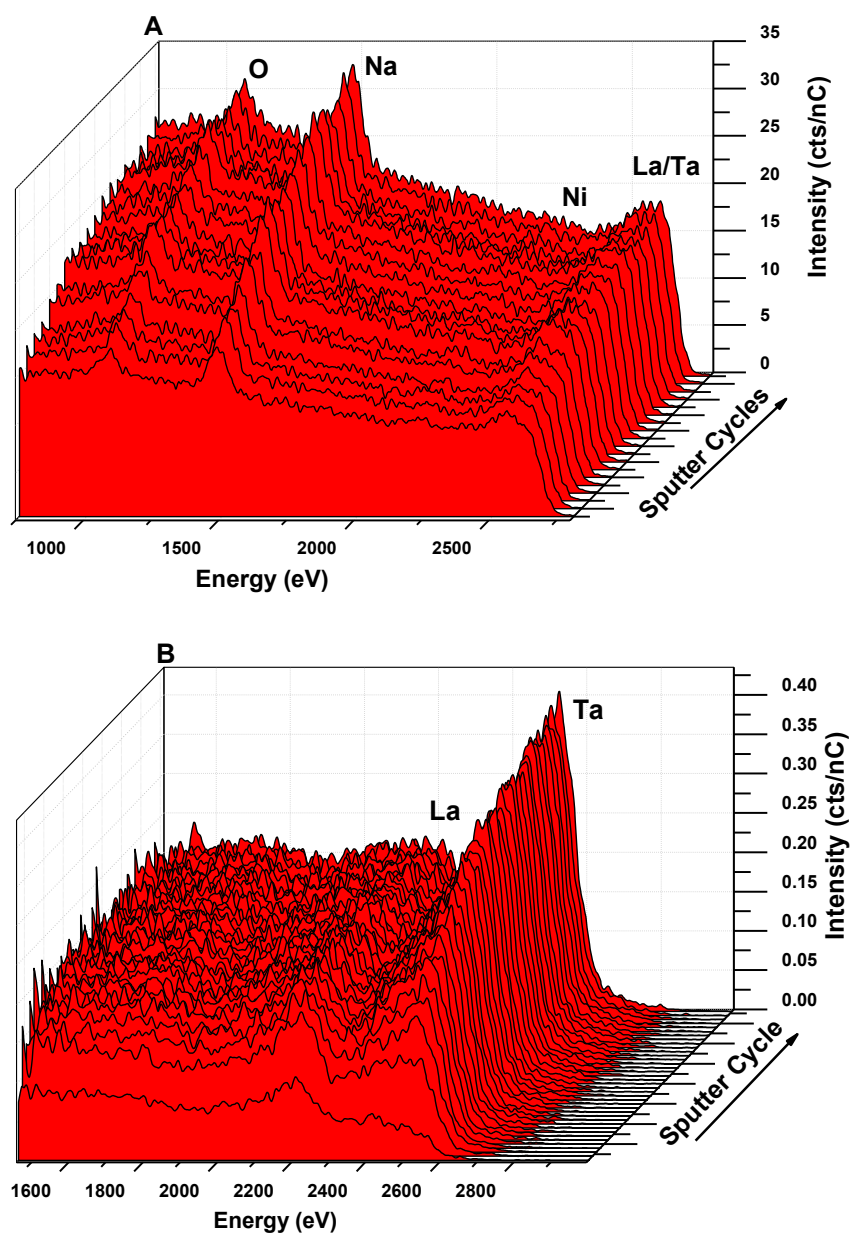
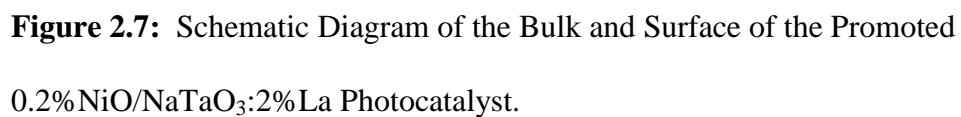


Figure 2.6: HS-LEIS Depth Profile for 0.2% NiO/NaTaO₃:2% La promoted photocatalyst using (a) He⁺ ion gas and (b) Ne⁺ ion gas.



CHAPTER 3

Fundamental Bulk/Surface Structure – Photoactivity

Relationships of Supported (Rh_{2-v}Cr_vO₃)/GaN Photocatalysts

Abstract

Bulk GaN and supported (Rh_{2-y}Cr_yO₃)/GaN photocatalysts were characterized and investigated for UV activated water splitting. The bulk and surface properties of these photocatalysts were characterized with Raman, UV-vis, Photoluminescence (PL) High Resolution-XPS and High Sensitivity-Low Energy Ion Scattering (HS-LEIS) spectroscopy to assist in the development of fundamental structure – photoactivity relationships. Raman and UV-vis spectroscopy showed that the molecular and electronic structures, respectively, of the GaN support were not perturbed by the deposition of the (Rh_{2-y}Cr_yO₃) mixed oxide NPs. High Resolution-XPS and High Sensitivity-LEIS reveal that the surface regions of GaN and supported (Rh_{2-y}Cr_yO₃)/GaN photocatalysts consist of Ga oxynitride and GaO surface layers, respectively. The supported (Rh_{2-y}Cr_yO₃) NPs exclusively consist of Cr⁺³ and Rh⁺³ cations. Photoluminescence (PL) spectroscopy was able to reveal that the (Rh₂₋

$_y\text{Cr}_y\text{O}_3$) NPs helps to decrease the recombination of electron/holes in the bulk GaN by acting as efficient electron traps promoting charge transfer to the surface. These new insights into the surface nature of the $(\text{Rh}_{2-y}\text{Cr}_y\text{O}_3)$ NPs show that Rh^{3+} species on the outermost surface layer are responsible for enhanced H_2 while other surface sites (Cr^{3+} , GaO_x and their contact points) are possibly responsible for O_2 production.

3.1 Introduction

Early research on photocatalytic water splitting primarily focused on the use of semiconductor metal oxide materials with UV irradiation [1-3]. More recently, non-oxide materials have been discovered that are also able to perform photocatalytic water splitting with visible excitation [4]. Unlike the extensive list (>130) of metal oxide semiconductors that can perform photocatalytic water splitting, there are only a handful of these bulk oxynitride materials with d^{10} electronic configuration that are active for overall photocatalytic water splitting: Ge_3N_4 [5-8], $(\text{Ga}_{1-x}\text{Zn}_x)(\text{N}_{1-x}\text{O}_x)$ [9-13], $(\text{Zn}_{1+x}\text{Ge})(\text{N}_2\text{O}_x)$ [14] and GaN [15-17]. There have also been other bulk oxynitride materials discovered with d^0 electronic configurations (Ti, Ta and Nb) that are able to produce H_2 and O_2 with sacrificial reagents, but none are capable of photocatalytic water splitting in pure water [2, 4]. The limited number of bulk oxynitride photocatalysts discovered to be capable of water splitting so far suggests that water splitting is a greater challenge for oxynitrides compared to metal oxide photocatalysts. Although other mixed metal oxynitride materials are more active than GaN and can utilize visible light for photocatalytic water splitting, it is important to

develop fundamental structure/photoactivity relationships for this basic nitride photocatalyst because it is a component of $(\text{Ga}_{1-x}\text{Zn}_x)(\text{N}_{1-x}\text{O}_x)$ oxynitride photocatalysts and understanding how the GaN photocatalyst functions is important for the design of advanced oxynitride photocatalysts.

The present study focuses on the bulk GaN semiconductor photocatalyst. Although GaN has been found to be unable to photocatalytically split water, it becomes an active photocatalyst with UV excitation ($\lambda > 300$ nm) when $(\text{Rh}_{2-y}\text{Cr}_y\text{O}_3)$ mixed oxide NPs are deposited on its surface (quantum efficiency (Q.E.) of 0.7%) [17]. The present investigation will apply high-resolution X-ray photoelectron spectroscopy (HR-XPS) and high-sensitivity low energy ion scattering (HS-LEIS) spectroscopy to provide new insights about the surface region ($\sim 1\text{-}3\text{ nm}$) and outermost atomic layer (~ 0.3 nm) of the supported $(\text{Rh}_{2-y}\text{Cr}_y\text{O}_3)/\text{GaN}$ photocatalyst system. Further insight into the molecular and electronic structures of the bulk GaN phase and influence of the supported $(\text{Rh}_{2-y}\text{Cr}_y\text{O}_3)$ NPs upon the bulk GaN phase properties will be obtained with *in situ* optical spectroscopic characterization (Raman, UV-vis, photoluminescence (PL) and time-resolved picosecond PL-Raman).

3.2 Experimental

3.2.1 Catalyst Synthesis

The bulk GaN was prepared from elemental gallium obtained from Mitsubishi Chemicals. The GaN was mixed in an evaporating dish with the aqueous precursors of $\text{Cr}(\text{NO}_3)_3 \cdot 9\text{H}_2\text{O}$ (Wako Pure Chemicals, 99.9%) and $\text{Na}_3\text{RhCl}_6 \cdot 2\text{H}_2\text{O}$ (Kanto

Chemicals, 97% as Rh) to yield a final composition of 1 wt.% Rh and 1.5wt.% Cr. This suspension was then placed over a water bath and continuously stirred with a glass rod until complete evaporation. The powder was then collected and mildly calcined in air at 623 K for one hour. The supported (Rh_{2-y}Cr_yO₃)/GaN photocatalyst was then washed with distilled water and dried overnight in an oven at 343 K.

3.2.2 Raman Spectroscopy

The Raman spectra for the photocatalyst were performed on a Lab Ram-HR Raman spectrometer (Horiba-Jobin Yvon) equipped with visible (532 nm) laser excitation and utilizing a confocal microscope (Olympus BX-30) for focusing the laser on the catalyst sample. The 532nm visible laser excitation was generated by Nd:YAG laser (10 mW) with the scattered photons directed into a single monochromator and focused onto a UV-sensitive liquid-N₂ cooled CCD detector (Horiba-Jobin Yvon CCD-3000V) having a spectral resolution of $\sim 2 \text{ cm}^{-1}$ for the given parameters. About 5-10 mg of the catalyst was placed into a high temperature *in situ* cell (Linkam TS-1500) with a quartz window and the spectrums were obtained under ambient conditions. The spectral acquisition time employed was 5 scans of 5 seconds/scan for each spectrum. System calibration was verified using a silica reference standard line at 520.7 cm^{-1} .

3.2.3 UV-Vis NIR Diffuse Reflectance Spectroscopy (DRS)

Ultra Violet-visible-Near Infrared (UV-vis-NIR) diffuse reflectance spectroscopy was utilized to obtain the optical edge energy, E_g , values for the photocatalysts. Spectra were obtained using a Varian Cary 5E UV-vis

spectrophotometer with a diffuse reflectance attachment (Harrick Praying Mantis Attachment, DRA-2). The finely ground powder catalyst samples (~20 mg) were loaded into an *in situ* cell (Harrick, HVC-DR2) and measured in the 200-800 nm spectral region with a magnesium oxide reflectance standard used as the baseline. A filter (Varian, 1.5ABS) was employed to minimize the background noise. A magnesium oxide white reflectance standard baseline was collected under ambient conditions. Determination of the Kubelka-Munk function, $F(R_{\infty})$, was obtained from the UV-vis DRS absorbance and processed with Microsoft Excel software. The edge energy was determined by finding the intercept of the straight line in the low-energy rise of a plot of $[F(R_{\infty})h\nu]^{\frac{1}{n}}$, where $n = 0.5$ for the direct allowed transition versus $h\nu$, where $h\nu$ is the energy of the incident photon [18-20].

3.2.4 Photoluminescence Spectroscopy and Photoluminescent Decay

PL spectra and transient PL lifetime measurements of the photocatalysts were conducted using a Ti:sapphire laser (Coherent Mira 900), tunable in the 685-1000 nm spectra range, generating 5 ps pulses with a 76 MHz repetition rate, pumped with a frequency-doubled Nd:YVO₄ laser (Coherent Verdi V-18). The output of the laser was frequency doubled using an ultrafast harmonic generator (Coherent 5-050). To perform the luminescence measurements, the excitation light at 400 nm was directed toward a microscope of a tunable micro-, macro-Raman/photoluminescence system (Jobin Yvon Horiba, T6400) and was focused using a long distance objective (50x, N/A=0.5) onto a sample to a spot size of ~ 2 μm . The photocatalyst sample was

placed into a high temperature *in situ* microscopy stage (Linkam, TS-1500) and pretreated as follows: The samples were heated at 10 °C/min to 673 K in flowing 10% O₂/N₂ (30 sccm) to remove water, since moisture causes quenching of the PL signal [21], and to fully oxidize the samples. Upon cooling to room temperature in flowing inert gas (N₂, 30 sccm), the photoluminescence decay measurements were made. To obtain complete PL spectra, the spectrometer was set to nanometer mode and the grating was moved several times in order to obtain the intensity over a 400 to 800 nm range. The luminescence light was collected through the same objective in backscattering geometry and focused onto a slit of the triple-monochromator equipped with a fast gated intensified charge coupled device (ICCD) camera collecting in the 350-900 nm range (LaVision, Picostar HR12). The ICCD camera was gated using a sequence of 76 MHz pulses propagating with a variable delay relative to the original train of trigger pulses (76 MHz) from a photodiode in a Ti:sapphire laser. The minimum gate width was 300 ps and the maximum delay was defined by the laser repetition rate (~13200 ps). The laser energy at the sample was maintained at approximately 1.6 mW to prevent photo-degradation of the photocatalyst sample. The grating was set to monitor decay centered at emission wavelengths from 500 to 700 nm.

3.2.5 High Resolution X-ray Photoelectron (HR-XPS) Spectroscopy

The HR-XPS spectra of the photocatalysts were obtained on a Scienta ESCA 300 spectrometer equipped with a 300 mm hemispherical electrostatic analyzer and a monochromatic Al K α X-ray source with energy of 1486.6 eV generated from a

rotating anode. This allows for improved chemical selectivity by narrowing the spectral peaks of elements and greatly reducing the spectral background signal compared to conventional XPS spectrometers. Each spectrum was calibrated using a binding energy (BE) value of 285.0 eV for carbon in the C1s region. The atomic concentration ratios were calculated by correcting the measured peak area ratios with relative sensitivity factors employed in the Casa XPS software version 2.3.15.

3.2.6 High Sensitivity Low Energy Ion Scattering (HS- LEISS)

Spectroscopy

Analysis of the outermost surface layer of the photocatalysts was obtained on the Qtac¹⁰⁰ HS-LEIS Spectrometer (ION-TOF) equipped with a highly sensitive double toroidal analyzer, 3000 times higher sensitivity than conventional LEIS spectrometers, which allows for static depth profiling. The photocatalyst samples were first gently cleaned with atomic oxygen to remove surface hydrocarbon contamination from the atmosphere prior to being transferred inside the analysis chamber. The HS-LEIS spectra were taken using both 4000 eV $^4\text{He}^+$ with 11300 pA current and 4000 eV $^{20}\text{Ne}^+$ with 478 pA current as ion sources. TOF mass filters were also utilized for spectra obtained with Ne^+ as an ion source for reduced flux background at low kinetic energies. For depth profiling, the surface was sputtered by Ar^+ gas at 500 eV at a sputter yield of 1×10^{15} ions/cm². Metallic Rh and Cr standards were also analyzed for quantifying the elemental composition of the photocatalysts.

3.3 Results and Discussion

3.3.1 Bulk Characteristics of GaN Photocatalysts

3.3.1.1 Bulk Molecular Structure

The Raman spectra for the ambient GaN photocatalysts are presented in Figure 1 and exhibit bands that are associated with the phonon modes of the hexagonal wurtzite GaN crystal structure [22, 23]. The Raman band at 140 cm^{-1} has been assigned to the E_2 phonon mode, the 413 cm^{-1} band is a combination of optical and acoustic modes, the 530 and 563 cm^{-1} bands are the transverse optical (TO) modes of A_1 and E_1 , respectively, and the 732 cm^{-1} band is from the combination of the longitudinal optical modes of A_1 and E_1 [22, 23]. The Raman spectrum of the supported $(\text{Rh}_{2-y}\text{Cr}_y\text{O}_3)/\text{GaN}$ photocatalyst is dominated by the GaN vibrations and is essentially the same as that of the bulk GaN. The characteristic sharp Raman bands of crystalline Cr_2O_3 NPs at 542 and 603 cm^{-1} [24, 25] are not observed suggesting that crystalline Cr_2O_3 NPs are not present. Crystalline Rh_2O_3 possesses a characteristic Raman band at 550 cm^{-1} [26] that cannot be detected because it is overshadowed by the strong GaN band in this region. Thus, the bulk molecular structure of the GaN phase is unchanged by the deposition of the $(\text{Rh}_{2-y}\text{Cr}_y\text{O}_3)$ mixed oxide NPs.

3.3.1.2 Bulk Electronic Structure

The bulk optical band gap (E_g) values determined from UV-vis DRS measurements and are given in Table 1. The optical band gap for bulk GaN is 3.3 eV and is not perturbed by the deposition of the $(\text{Rh}_{2-y}\text{Cr}_y\text{O}_3)$ mixed oxide NPS, which indicates that the bulk GaN component dominates the UV-vis absorbance spectrum of the supported $(\text{Rh}_{2-y}\text{Cr}_y\text{O}_3)/\text{GaN}$ photocatalyst system.

3.3.2 Surface Composition of GaN photocatalysts

3.3.2.1 Atomic Composition and Chemical State of the Surface Region (~1-3 nm)

The XPS survey spectra for the surface region (~1-3 nm) of the GaN photocatalysts are presented in Figure 2 and the atomic composition is reported in Table 2. The surface region for the bulk GaN consists only of Ga, O and N and no contaminants were detected. Note the O/Ga~1 atomic ratio indicating that Ga is extensively oxidized in the surface region under ambient exposure. The compositions of the surface region for the supported (Rh_{2-y}Cr_yO₃)/GaN and bulk GaN photocatalysts are compared in Table 2. As expected for deposition of an oxide on GaN, the addition of the (Rh_{2-y}Cr_yO₃) mixed oxide NPs to the GaN support doubles the O concentration, while decreasing the concentration of the GaN support elements (~50% Ga and ~30% N).

HR-XPS surface analysis of Cr and Rh for the supported (Rh_{2-y}Cr_yO₃)/GaN photocatalyst was undertaken to determine the chemical states of Cr and Rh in the surface region and presented in Figure 3. The HR-XPS spectra for the Cr 2p and Rh 3d regions of the supported (Rh_{2-y}Cr_yO₃)/GaN photocatalyst reveal the presence of only Cr³⁺ and Rh³⁺ and the absence of Cr⁶⁺ or metallic Rh(0) in the surface region.

3.3.2.2 Outermost Atomic Layer Composition (~0.3 nm)

The outermost surface layer (~0.3 nm) and layers below the surface of bulk GaN were analyzed with dynamic HS-LEIS employing a He⁺ ion gas source and the findings are shown in Figure 4. The HS-LEIS signal for N is almost absent from the

topmost surface layer and significantly increases in intensity into a definable peak with further sputtering into the bulk. Although Ga is present on the topmost surface layer, its HS-LEIS signal also significantly increases with depth profiling. In contrast to that of Ga and N, the HS-LEIS signal for O is strongest on the outermost layer and decreases with sputtering into the bulk demonstrating surface enrichment of O. Depth profiling using Ne^+ ion gas source was also performed (not shown for brevity) showing only a single peak for Ga. The HS-LEIS sputtering findings reveal that for bulk GaN the outermost surface layer consists of GaO_x and that the surface region is present as a Ga oxynitride (GaO_xN_y) layer.

The HS-LEIS spectra comparing the untreated and atomic oxygen treated supported ($\text{Rh}_{2-y}\text{Cr}_y\text{O}_3$)/GaN photocatalyst is presented in Figure 5. This pretreatment method was used to clean off hydrocarbon deposits on the surface, increasing signal intensity and does not affect the surface composition of the photocatalyst. The HS-LEIS depth profiles for the supported ($\text{Rh}_{2-y}\text{Cr}_y\text{O}_3$)/GaN photocatalyst are presented in Figure 6. From Figure 6a, the outermost surface layer contains O, Cr, Ga and Rh and does not contain any detectable N. It appears that the oxidation treatment to form the supported ($\text{Rh}_{2-y}\text{Cr}_y\text{O}_3$) mixed oxide NPs on the GaN support also oxidized the outer surface layers of GaN and is consistent with the 100% increase of the XPS O concentration in the surface region (see Table 2) [27].

More quantitative depth profiling information is provided with Ne^+ depth profiling analysis as shown in Figure 6b and, surprisingly, small concentrations of Sn and Ba contaminants are also found to be present in the outermost surface layers. The

Sn and Ba contaminants were not evident for the bulk GaN and the source of these impurities is not known, but could be due to handling of the material during and after impregnation of the $\text{Cr}(\text{NO}_3)_3 \cdot 9\text{H}_2\text{O}$ and $\text{Na}_3\text{RhCl}_6 \cdot 2\text{H}_2\text{O}$ precursors. Metallic Cr and Rh standards were used to quantify the amounts of these two elements with respect to each other and their quantitative depth profile concentrations are shown in Figure 7. Both Rh and Cr are surface enriched since their bulk concentrations are 1.0% and 1.5% wt., respectively, while their concentrations in the surface region are 3.2% and 6.7%. The outermost surface layer contains more Cr than Rh, the concentrations of Cr and Rh are about the same for the first few layers below the outermost surface, and the concentration of Cr is larger than Rh for the deeper layers below the surface. The increase in the concentration of Cr at deeper layers is indicative of greater Cr concentration in the deeper layers of the $(\text{Rh}_{2-y}\text{Cr}_y\text{O}_3)$ NPs and the presence of dissolved Cr beneath the surface. At all depths, the concentrations of Rh and Cr in the surface region are enriched compared to their bulk concentrations.

3.3.3 Electron/Hole Generation and Recombination

The steady-state PL emissions spectra at 400 nm excitation for the GaN and supported $(\text{Rh}_{2-y}\text{Cr}_y\text{O}_3)/\text{GaN}$ photocatalysts are presented in Figure 8. Both photocatalysts exhibit broad emission bands with maxima at 710 and 725 nm as indicated in Table 1. The intensity of the PL emissions spectra is indicative of the population of electron/hole recombination centers in a photocatalyst [21, 28]. Even with excitation at 400 nm that is greater than the optical absorption edge energy of the GaN (3.3 eV or 375 nm); there is still a large population of photo-excited electrons

generated in the bulk of the GaN. Deposition of the ($\text{Rh}_{2-y}\text{Cr}_y\text{O}_3$) mixed oxide NPs on GaN diminishes the PL emissions reflecting that photo-excited electrons are being trapped by the supported ($\text{Rh}_{2-y}\text{Cr}_y\text{O}_3$) NPs at the mixed oxide/GaN interface and, therefore, are unavailable for recombining with holes in the GaN bulk. In other words, the supported ($\text{Rh}_{2-y}\text{Cr}_y\text{O}_3$) NPs on the GaN support act as efficient electron traps for the photoexcited electrons generated from the GaN bulk and, consequently, minimize electron/hole recombination and promotes charge transfer to the surface [21, 29, 30].

The transient PL decay curves for the GaN photocatalysts using 400 nm excitation at different emission wavelengths are plotted in Figure 9. At all the examined emission wavelengths, both catalysts exhibit a constant emission intensity signifying no decay emissions. The PL properties of the solid-state GaN have been well studied due to its importance in optical and electronic applications [31-33]. These studies utilize excitation in the deep UV range (~325 nm) that is able to generate excited photoelectrons in the GaN so the electron decay can be monitored on the picosecond timescale. Although a higher light excitation is used (400 nm), the GaN photocatalysts are able to generate steady-state PL emissions so there are excited electrons that are decaying and recombining at this wavelength. On the picosecond timescale, the PL emission measured is generated by fluorescence from the material [31]. This lack of measurable fluorescence decay emissions on the picosecond timescale could be due to the powdered GaN exhibiting PL generated from phosphorescence emissions. Phosphorescence materials tend to emit PL over a longer time period (ms - hrs) so there will not be detectable emissions decay on the

picosecond timescale. The constant PL emissions intensity after the pulsed 400 nm excitation can, thus, be attributed to the GaN photocatalysts exhibiting phosphorescence longer than the picosecond timescale.

3.3.4 Bulk/Surface – Photoactivity Relationships of GaN Photocatalysts

The supported (Rh_{2-y}Cr_yO₃)/GaN photocatalyst functions as a two-component system. The role of bulk GaN is to generate electron/hole pairs using UV excitation. Surface analysis was able to show that the GaN bulk phase dynamically changes: GaN → GaO_xN_y → GaO_x in the surface region with some dissolved Cr³⁺ beneath the outermost surface layer. The (Rh_{2-y}Cr_yO₃) NPs are responsible for transferring the photoexcited electrons to the surface and act as the catalytic active sites. In the previous work, GaN was unable to photocatalytically split water by itself only (Rh_{2-y}Cr_yO₃)/GaN was able to produce stoichiometric amount of H₂/O₂ [17]. It was proposed that (Rh_{2-y}Cr_yO₃) were the sites for H₂ production from using MeOH as a sacrificial reagent. The GaN was proposed as the sites for O₂ production from using AgNO₃ as a sacrificial reagent. For another oxynitride photocatalyst, (Ga_{1-x}Zn_x)(N_{1-x}O_x), the loading of only Rh₂O₃ resulted in the nonstoichiometric production rate 50 H₂ : 1 O₂ [10, 34]. However with the addition of Cr₂O₃ the production of H₂ was increased by ~ 77x with stoichiometric O₂ production. These observations show that Rh³⁺ is primarily responsible for H₂ evolution but it is still not clear which site is active for O₂ evolution. From the surface analysis, the possible sites for O₂ evolution are the Cr³⁺ in the (Rh_{2-y}Cr_yO₃) NPs, the GaO_x surface layer or at the contact point

between the two. A schematic modeling the photocatalytic process on $(\text{Rh}_{2-y}\text{Cr}_y\text{O}_3)/\text{GaN}$ is shown in Figure 10.

3.4 Conclusions

The bulk and surface properties of $(\text{Rh}_{2-y}\text{Cr}_y\text{O}_3)/\text{GaN}$ photocatalysts were investigated using bulk (Raman, UV-vis, and PL) and surface (HS-LEIS and HR-XPS) spectroscopic techniques. The bulk molecular and electronic structure of the GaN phase was not affected by the addition of the $(\text{Rh}_{2-y}\text{Cr}_y\text{O}_3)$. The $(\text{Rh}_{2-y}\text{Cr}_y\text{O}_3)$ was found to decrease the recombination of excited electron/holes in the bulk GaN via charge transfer of the excited electrons to the surface promoting the surface photocatalytic reaction. Surface analysis was able to reveal that the composition of the bulk GaN dynamically changes from $\text{GaN} \rightarrow \text{GaO}_x\text{N}_y \rightarrow \text{GaO}_x$ near the surface region. The surface composition of the $(\text{Rh}_{2-y}\text{Cr}_y\text{O}_3)/\text{GaN}$ was revealed for the first time showing that Rh^{3+} present on the outermost surface layer was responsible for enhanced H_2 while the O_2 production can possibly be attributed to other surface sites (Cr^{3+} , GaO_x , or at their contact points).

Acknowledgements

This research was financially supported by the Department of Energy grant: DOE-FG02-93ER14350. Special thanks goes out to Alexander Puretsky at the Center for Nanophase Materials Sciences at Oak Ridge National Laboratory and along with Charles A. Roberts for assistance with the PL experiments in conjunction with User

Project CNMS2008-075. Thanks to K. Maeda and Professor K. Domen at the University of Tokyo for their assistance with the synthesis of the GaN photocatalysts. The assistance of Dr. A. Miller and R. Pafchek at Lehigh University in obtaining and interpreting the HR-XPS and HS-LEIS data is also gratefully acknowledged.

References

- [1] F.E. Osterloh, "Inorganic Materials as Catalysts for Photochemical Splitting of Water." *Chem. Mater.*, 20, 35, (2008).
- [2] A. Kudo, Y. Miseki, "Heterogeneous photocatalyst materials for water splitting." *Chem. Soc. Rev.*, 38, 253, (2009).
- [3] X. Chen, S. Shen, L. Guo, and S.S. Mao, "Semiconductor-based Photocatalytic Hydrogen Generation." *Chem. Rev.*, 110, 6503, (2010).
- [4] K. Maeda, K. Domen, "New Non-Oxide Photocatalysts Designed for Overall Water Splitting under Visible Light." *J. Phys. Chem. C*, 111, 7851, (2007).
- [5] J. Sato, N. Saito, Y. Yamada, K. Maeda, T. Takata, J.N. Kondo, M. Hara, H. Kobayashi, K. Domen, and Y. Inoue, "RuO₂-Loaded beta -Ge₃N₄ as a Non-Oxide Photocatalyst for Overall Water Splitting." *J. Am. Chem. Soc.*, 127, 4150, (2005).
- [6] Y. Lee, T. Watanabe, T. Takata, M. Hara, M. Yoshimura, and K. Domen, "Effect of High-Pressure Ammonia Treatment on the Activity of Ge₃N₄ Photocatalyst for Overall Water Splitting." *J. Phys. Chem. B*, 110, 17563, (2006).
- [7] K. Maeda, N. Saito, D. Lu, Y. Inoue, and K. Domen, "Photocatalytic Properties of RuO₂-Loaded beta -Ge₃N₄ for Overall Water Splitting." *J. Phys. Chem. C*, 111, 4749, (2007).

- [8] K. Maeda, N. Saito, Y. Inoue, and K. Domen, "Dependence of Activity and Stability of Germanium Nitride Powder for Photocatalytic Overall Water Splitting on Structural Properties." *Chem. Mater.*, 19, 4092, (2007).
- [9] K. Maeda, K. Teramura, D. Lu, N. Saito, Y. Inoue, and K. Domen, "Roles of Rh/Cr₂O₃ (Core/Shell) Nanoparticles Photodeposited on Visible-Light-Responsive (Ga_{1-x}Zn_x)(N_{1-x}O_x) Solid Solutions in Photocatalytic Overall Water Splitting." *J. Phys. Chem. C*, 111, 7554, (2007).
- [10] K. Maeda, K. Teramura, D. Lu, T. Takata, N. Saito, Y. Inoue, and K. Domen, "Characterization of Rh-Cr Mixed-Oxide Nanoparticles Dispersed on (Ga_{1-x}Zn_x)(N_{1-x}O_x) as a Cocatalyst for Visible-Light-Driven Overall Water Splitting." *J. Phys. Chem. B*, 110, 13753, (2006).
- [11] K. Maeda, K. Teramura, D. Lu, N. Saito, Y. Inoue, and K. Domen, "Noble-metal/Cr₂O₃ core/shell nanoparticles as a co-catalyst for photocatalytic overall water splitting." *Angew. Chem. , Int. Ed.*, 45, 7806, (2006).
- [12] K. Maeda, K. Teramura, and K. Domen, "Effect of post-calcination on photocatalytic activity of (Ga_{1-x}Zn_x)(N_{1-x}O_x) solid solution for overall water splitting under visible light." *J. Catal.*, 254, 198, (2008).

- [13] K. Maeda, K. Teramura, N. Saito, Y. Inoue, and K. Domen, "Improvement of photocatalytic activity of $(\text{Ga}_{1-x}\text{Zn}_x)(\text{N}_{1-x}\text{O}_x)$ solid solution for overall water splitting by co-loading Cr and another transition metal." *J. Catal.*, 243, 303, (2006).
- [14] Y. Lee, H. Terashima, Y. Shimodaira, K. Teramura, M. Hara, H. Kobayashi, K. Domen, and M. Yashima, "Zinc germanium oxynitride as a photocatalyst for overall water splitting under visible light." *J. Phys. Chem. C*, 111, 1042, (2007).
- [15] N. Arai, N. Saito, H. Nishiyama, Y. Inoue, K. Domen, and K. Sato, "Overall water splitting by RuO_2 -dispersed divalent-ion-doped GaN photocatalysts with d10 electronic configuration." *Chem. Lett.*, 35, 796, (2006).
- [16] N. Arai, N. Saito, H. Nishiyama, K. Domen, H. Kobayashi, K. Sato, and Y. Inoue, "Effects of divalent metal ion (Mg^{2+} , Zn^{2+} and Be^{2+}) doping on photocatalytic activity of ruthenium oxide-loaded gallium nitride for water splitting." *Catal. Today*, 129, 407, (2007).
- [17] K. Maeda, K. Teramura, N. Saito, Y. Inoue, and K. Domen, "Photocatalytic overall water splitting on gallium nitride powder." *Bull. Chem. Soc. Jpn.*, 80, 1004, (2007).
- [18] P. Kubelka, F. Munk, *Z. Tech. Phys.*, 12, 593, (1931).

- [19] X. Gao, I.E. Wachs, "Investigation of Surface Structures of Supported Vanadium Oxide Catalysts by UV-vis-NIR Diffuse Reflectance Spectroscopy." *J. Phys. Chem. B*, 104, 1261, (2000).
- [20] W.N. Delgass (Ed.), *Spectroscopy in heterogeneous catalysis*, Academic Press:New York, 1979.
- [21] M. Anpo, P.V. Kamat (Eds.), *Environmentally Benign Photocatalysts: Applications of Titanium Oxide-based Materials*, Springer:New York, 2010.
- [22] W. Han, Z. Liu, and H. Yu, "Synthesis and optical properties of GaN/ZnO solid solution nanocrystals " *Appl. Phys. Lett.*, 96, 183112, (2010).
- [23] V. Davydov, Y. Kitaev, I. Goncharuk, A. Smirnov, J. Graul, O. Semchinova, D. Uffmann, M. Smirnov, A. Mirgorodsky, and R. Evarestov, "Phonon dispersion and Raman scattering in hexagonal GaN and AlN " *Physical Review B*, 58, 12899, (1998).
- [24] E.L. Lee, I.E. Wachs, "In Situ Spectroscopic Investigation of the Molecular and Electronic Structures of SiO₂ Supported Surface Metal Oxides." *J. Phys. Chem. C*, 111, 14410, (2007).
- [25] D.S. Kim, J.M. Tatibouet, and I.E. Wachs, "Surface structure and reactivity of chromium trioxide/silica catalysts," *J. Catal.*, 136, 209, (1992).

- [26] C.T. Williams, C.G. Takoudis, and M.J. Weaver, "Methanol Oxidation on Rhodium As Probed by Surface-Enhanced Raman and Mass Spectroscopies: Adsorbate Stability, Reactivity, and Catalytic Relevance " *The Journal of Physical Chemistry B*, 102, 406, (1998).
- [27] H. BRONGERSMA, M. DRAXLER, M. DERIDDER, and P. BAUER, "Surface composition analysis by low-energy ion scattering " *Surface Science Reports*, 62, 63, (2007).
- [28] G.D. Gilliland, "Photoluminescence spectroscopy of crystalline semiconductors " *Materials Science and Engineering: R: Reports*, 18, 99, (1997).
- [29] C. Hu, C. Tsai, and H. Teng, "Structure Characterization and Tuning of Perovskite-Like NaTaO₃ for Applications in Photoluminescence and Photocatalysis " *J Am Ceram Soc*, 92, 460, (2009).
- [30] C. Hu, Y. Lee, and H. Teng, "Efficient water splitting over Na_{1-x}K_xTaO₃ photocatalysts with cubic perovskite structure " *J.Mater.Chem.*, (2011).
- [31] M.A. Reshchikov, H. Morkoc, "Luminescence properties of defects in GaN," *J. Appl. Phys.*, 97, 061301, (2005).
- [32] S. Nakamura, "III-V nitride based light-emitting devices." *Solid State Commun.*, 102, 237, (1997).

- [33] E. Calleja, M. Sánchez-García, F. Sánchez, F. Calle, F. Naranjo, E. Muñoz, U. Jahn, and K. Ploog, "Luminescence properties and defects in GaN nanocolumns grown by molecular beam epitaxy " *Physical Review B*, 62, 16826, (2000).
- [34] K. MAEDA, K. TERAMURA, N. SAITO, Y. INOUE, and K. DOMEN, "Improvement of photocatalytic activity of $(\text{Ga}_{1-x}\text{Zn}_x)(\text{N}_{1-x}\text{O}_x)$ solid solution for overall water splitting by co-loading Cr and another transition metal " *Journal of Catalysis*, 243, 303, (2006).

Excitation 400 nm		
Catalyst	E_g (eV)	Peak Maximum (nm)
GaN	3.3	725
(Rh_{2-y}Cr_yO₃) /GaN	3.3	710

Table 3.1: E_g values from UV-vis DRS, and peak emission wavelengths from PL spectroscopy of the GaN photocatalysts at 400 nm excitation.

Element	GaN	(Rh_{2-y}Cr_yO₃)/GaN
O 1s	19.0%	39.5%
N 1s	62.0%	41.1%
Ga 2p 3/2	19.0%	9.5%
Cr 2p 3/2	0.0%	6.7%
Rh 3d	0.0%	3.2%

Table 3.2: HR-XPS surface region atomic composition (~1-3nm) of GaN photocatalysts.

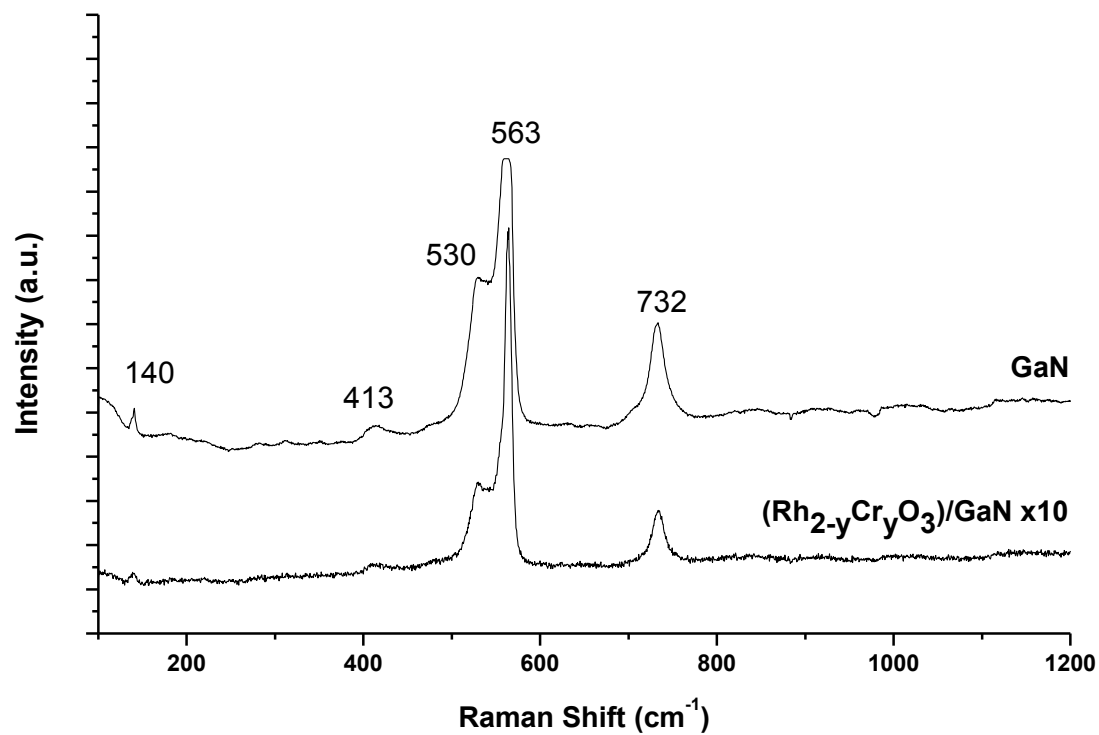


Figure 3.1: Raman spectra for GaN photocatalysts (532 nm).

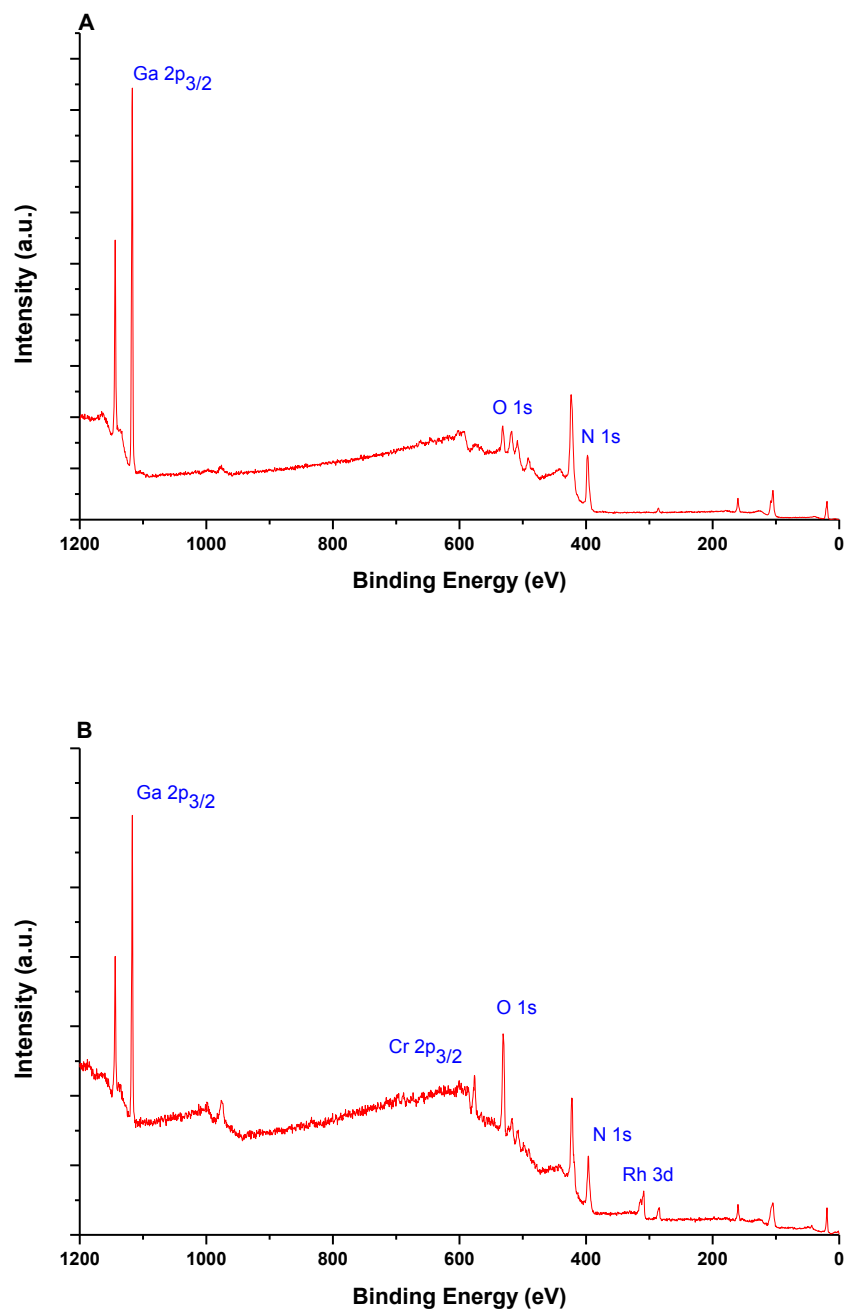


Figure 3.2: XPS survey spectra of (a) GaN and (b) supported (Rh_{2-y}Cr_yO₃)/GaN photocatalysts.

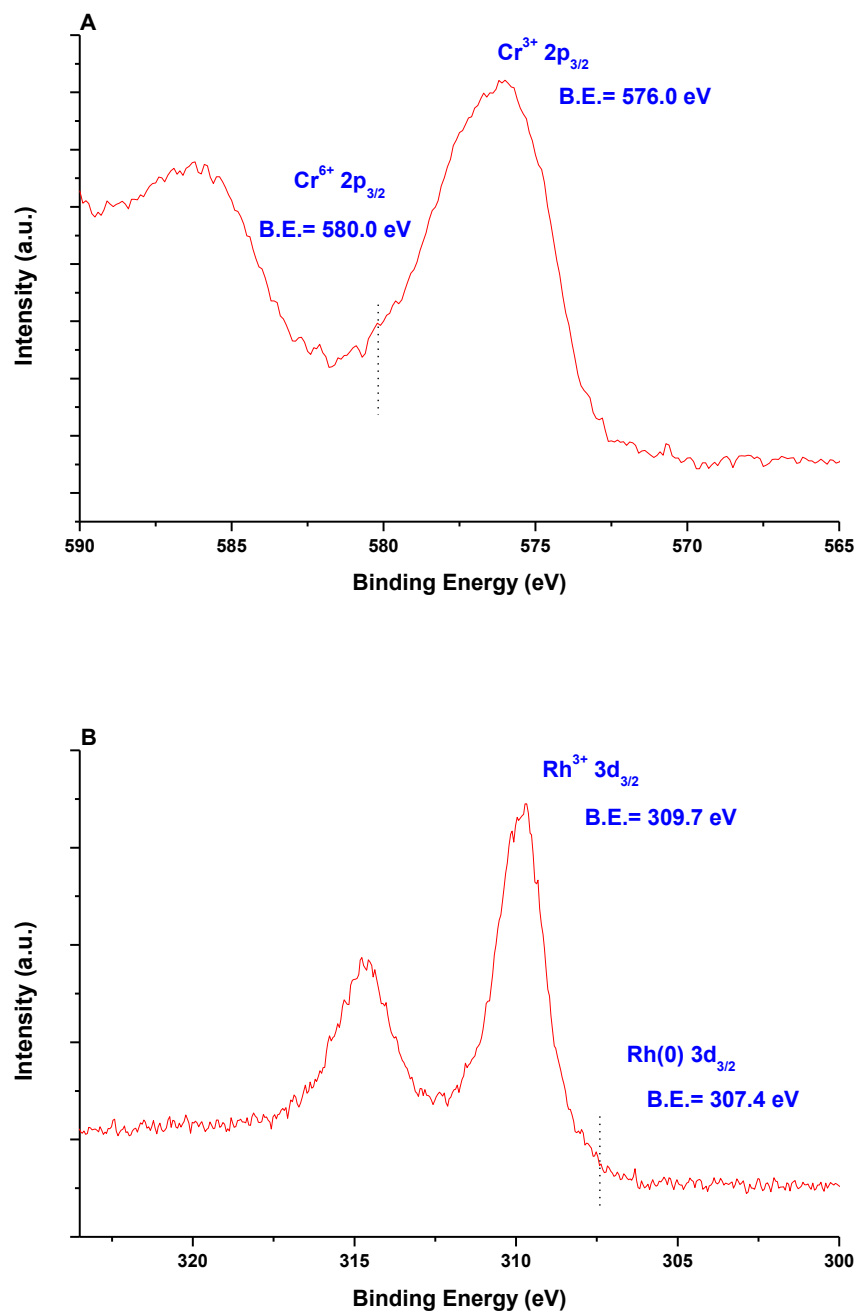


Figure 3.3: HR-XPS spectra of (a) Cr 2p and (b) Rh 3d regions of the supported (Rh/Cr₂O₃)/GaN photocatalyst.

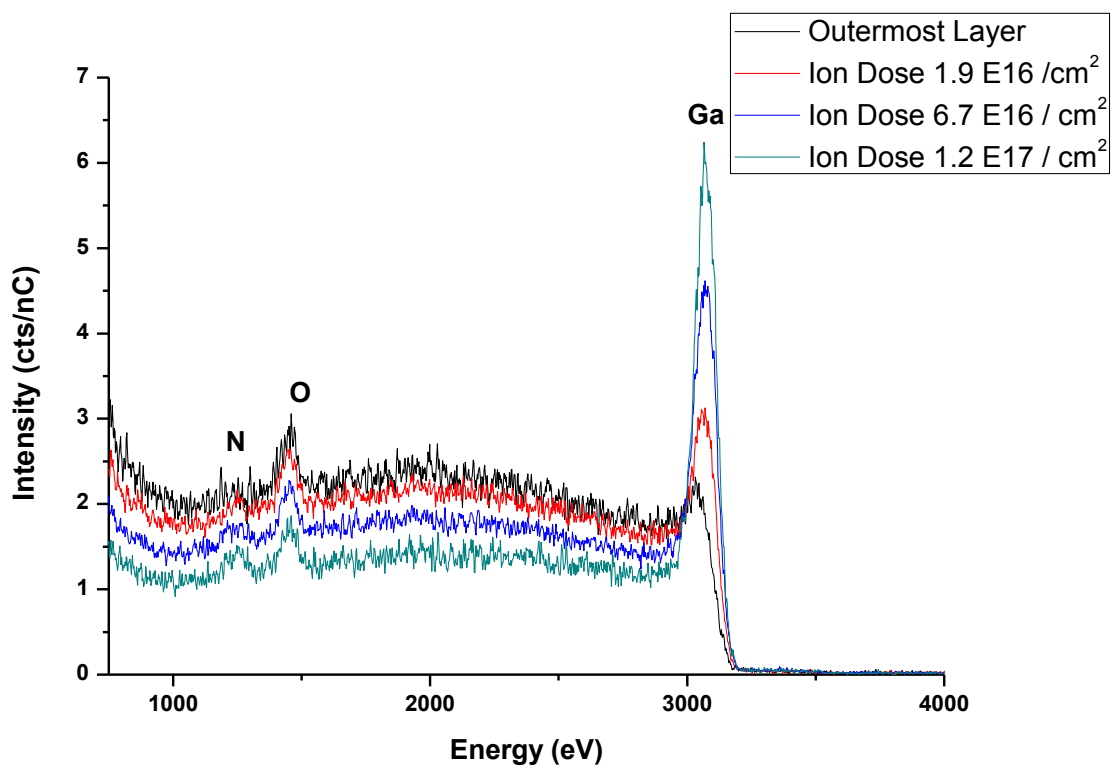


Figure 3.4: HS-LEIS Depth Profile for GaN photocatalyst using He⁺ ion gas.

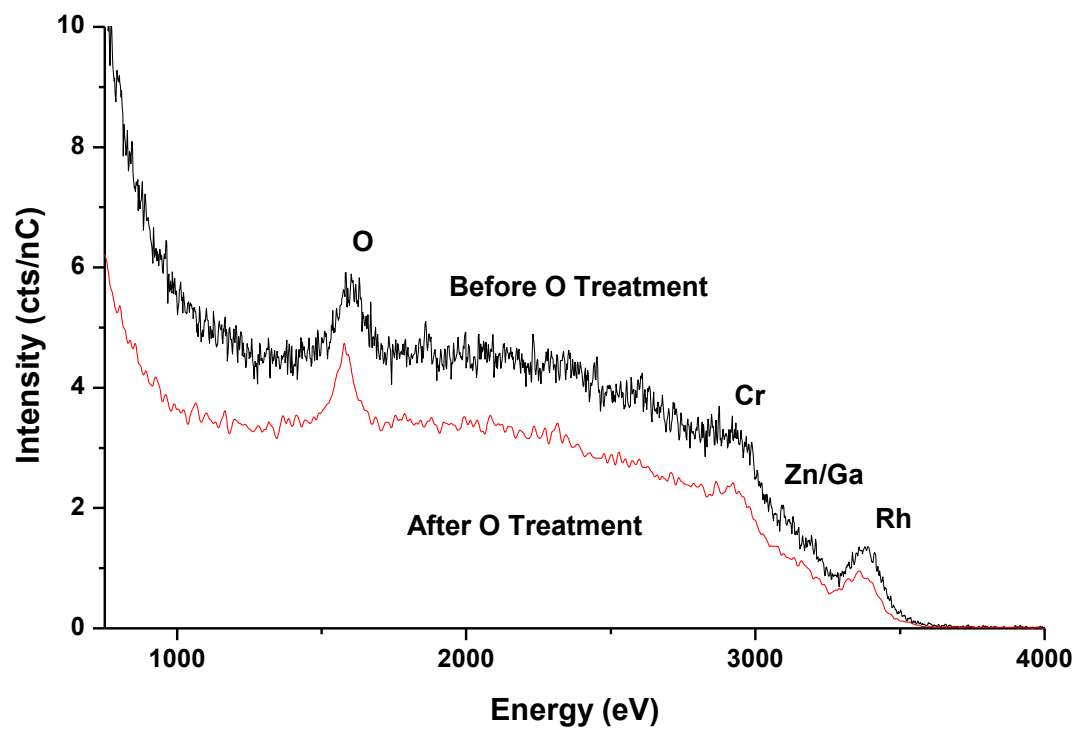


Figure 3.5: HS-LEIS spectra of untreated and atomic O treated supported ($\text{Rh}_{2-y}\text{Cr}_y\text{O}_3$)/GaN photocatalyst.

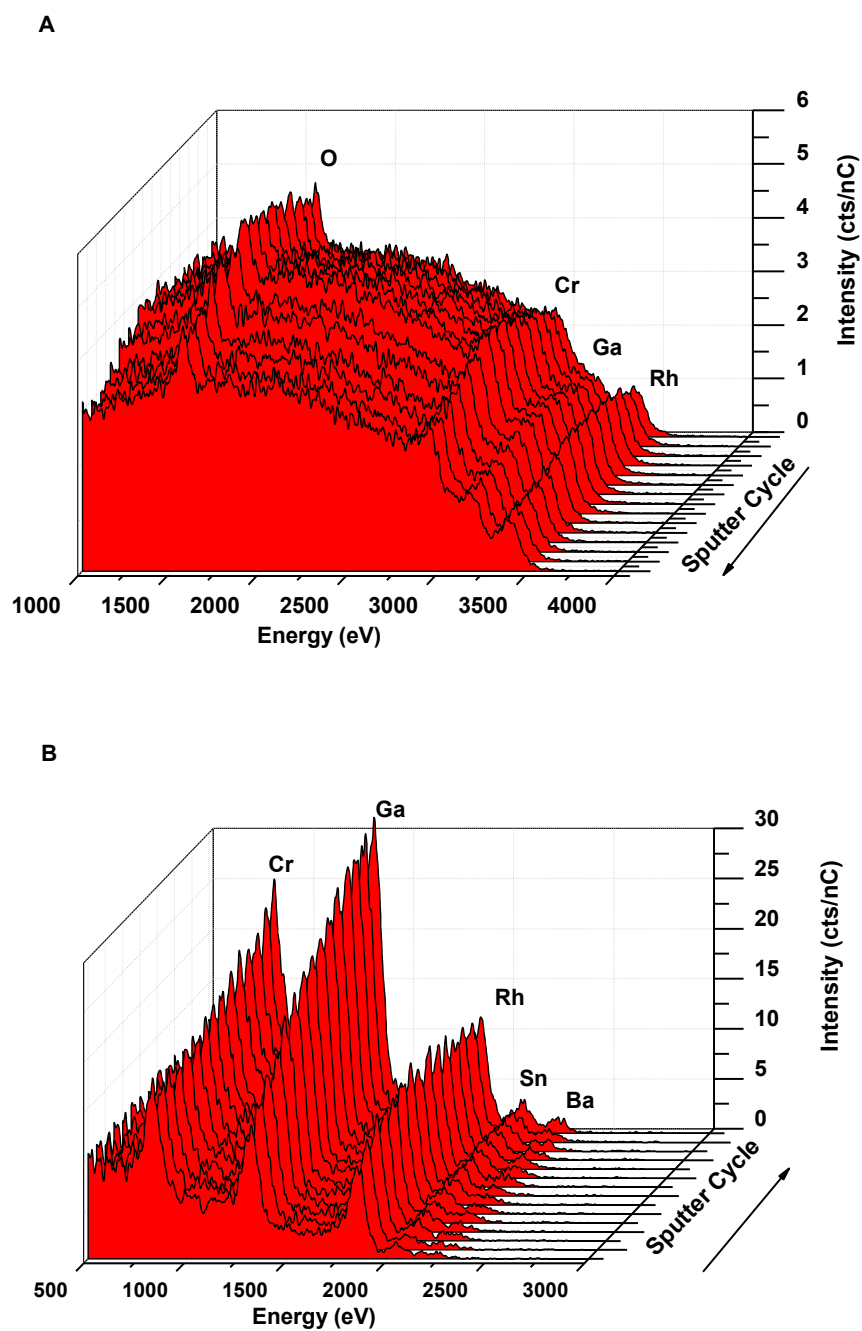


Figure 3.6: HS-LEIS depth profile for the supported $(\text{Rh}_{2-y}\text{Cr}_y\text{O}_3)/\text{GaN}$ photocatalyst using (a) He^+ ion gas and (b) Ne^+ ion gas.

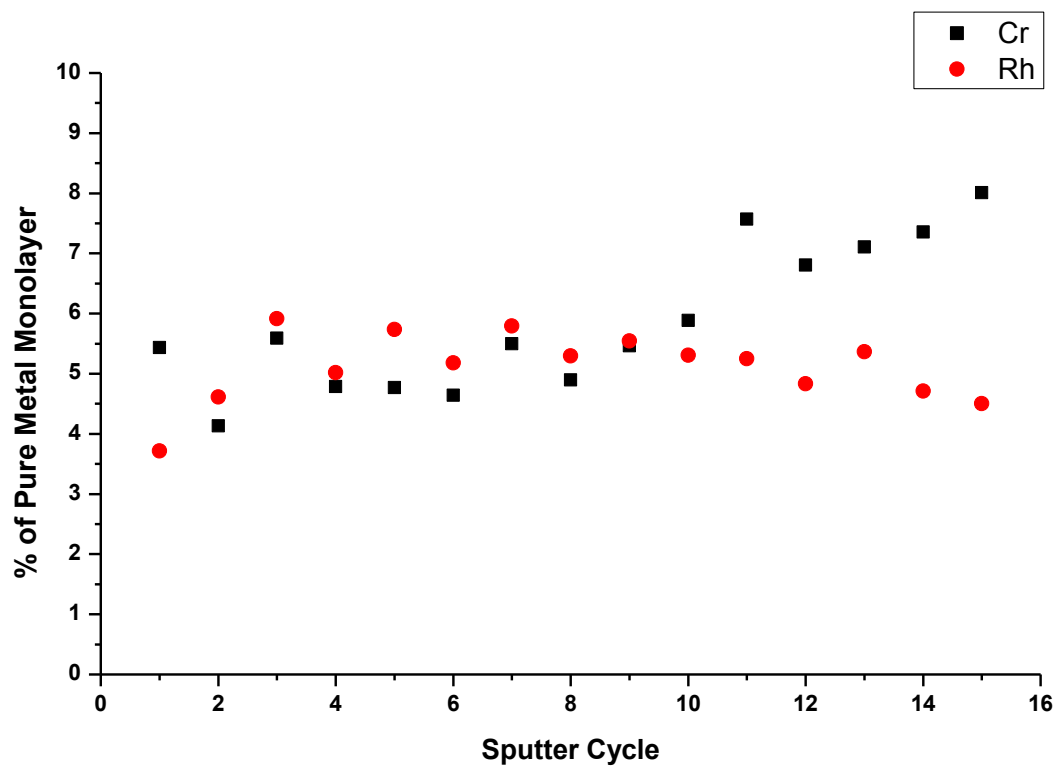


Figure 3.7: HS-LEIS Depth Profile of Cr and Rh for supported $(\text{Rh}_{2-y}\text{Cr}_y\text{O}_3)/\text{GaN}$ photocatalyst using Ne^+ ion gas.

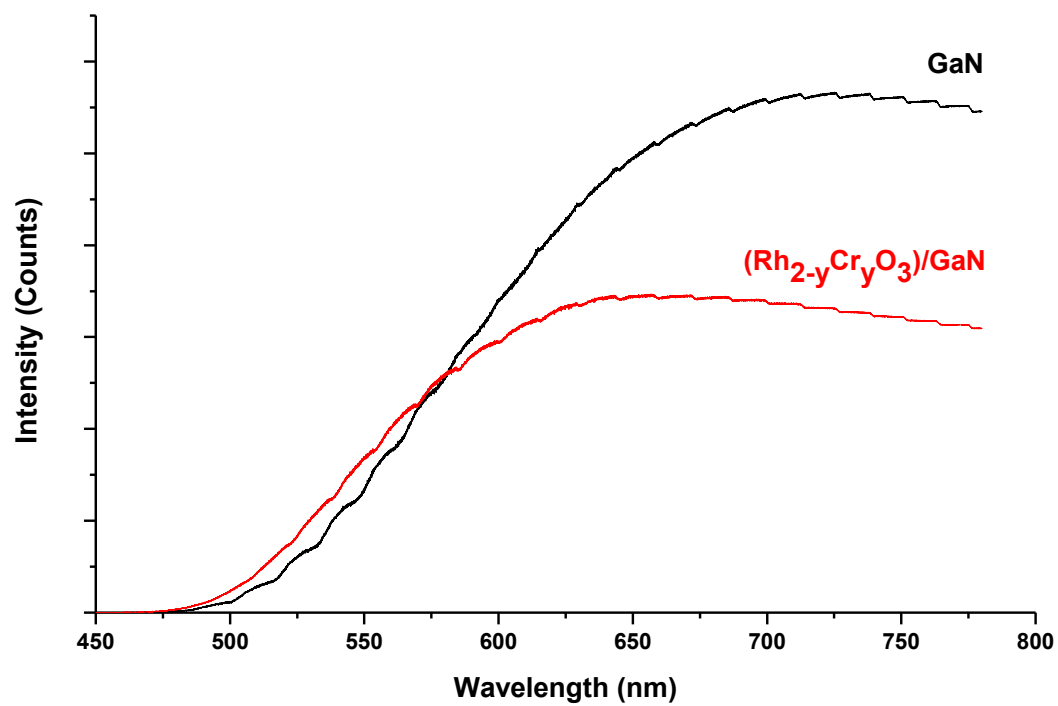


Figure 3.8: PL emissions spectra for GaN photocatalysts (400 nm excitation).

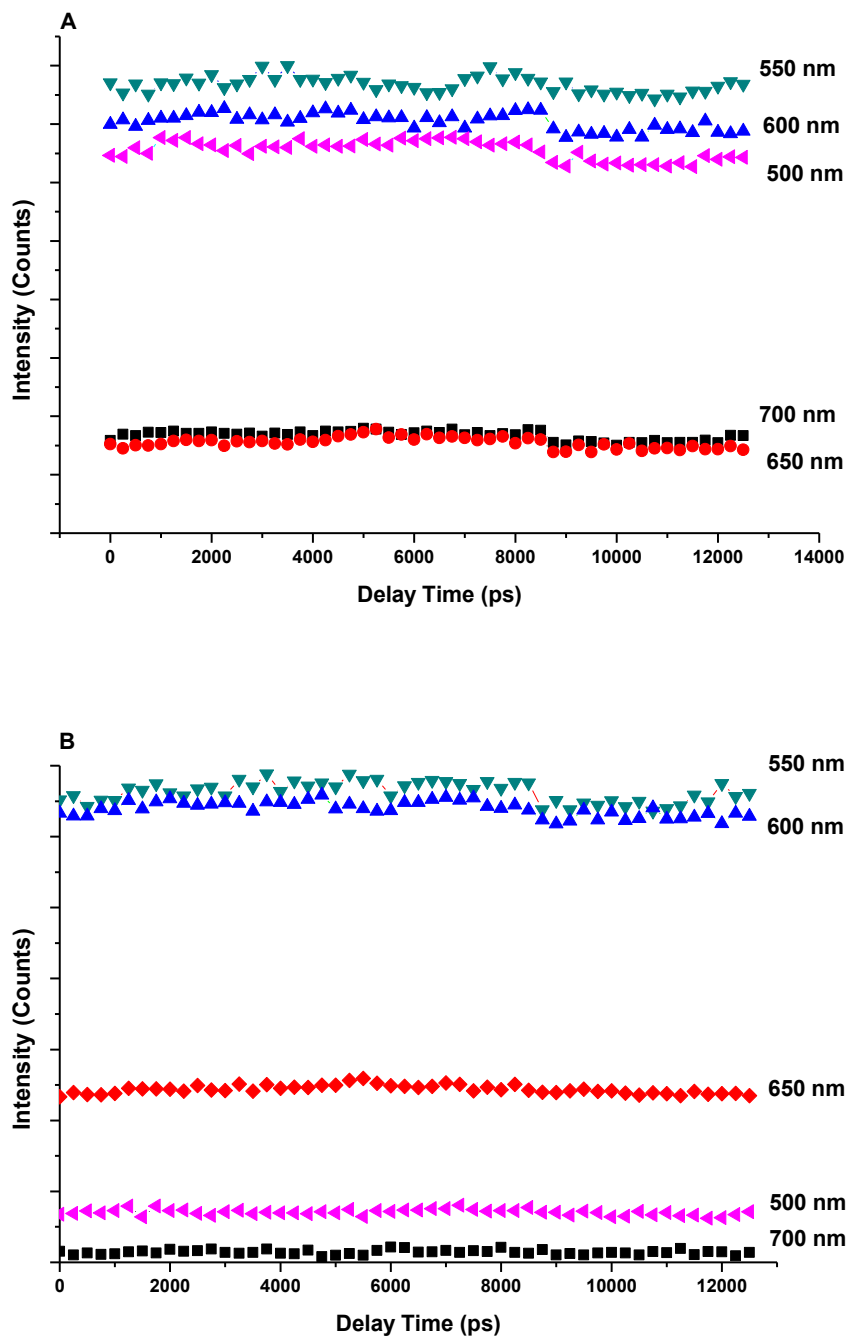


Figure 3.9: PL lifetimes spectra for (a) GaN and (b) (Rh_{2-y}Cr_yO₃)/GaN photocatalysts at different emissions wavelengths (400 nm excitation).

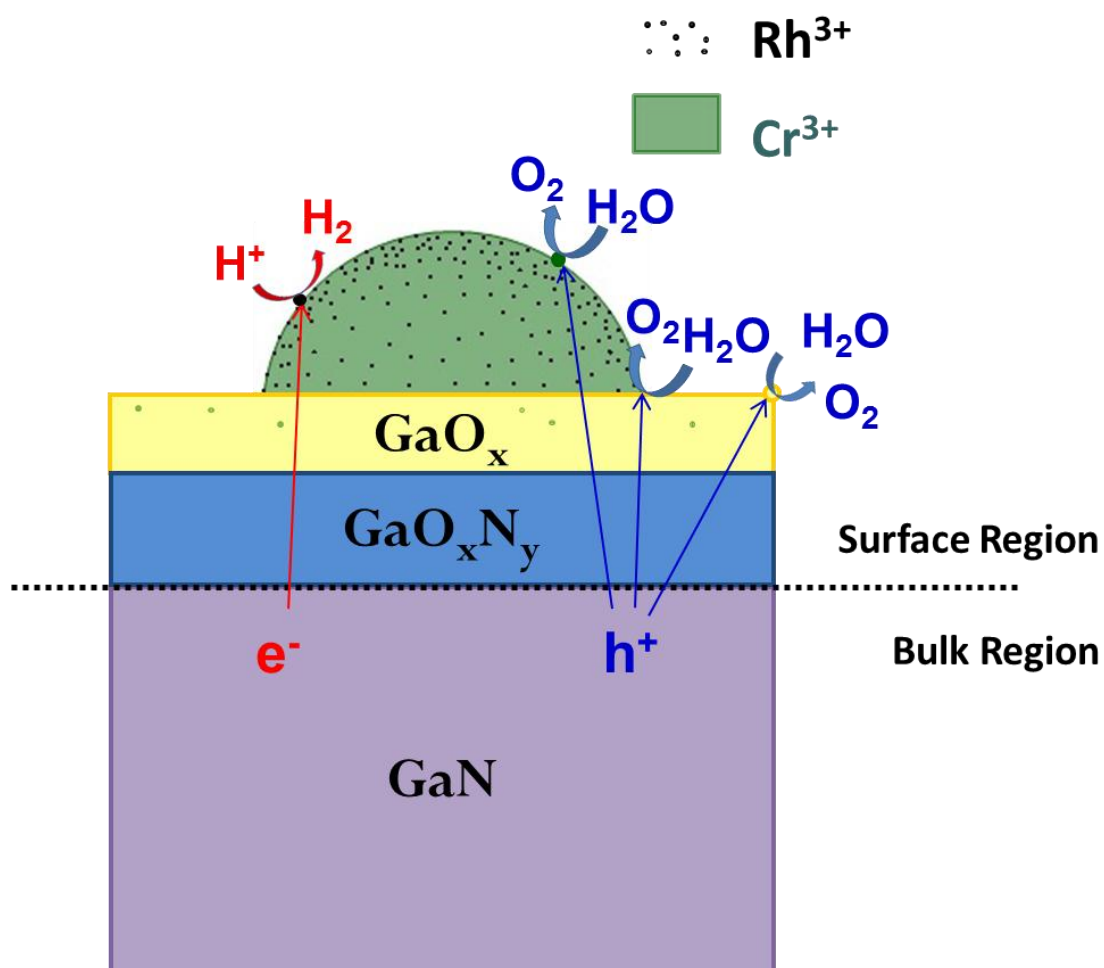


Figure 3.10: Schematic of $(\text{Rh}_{2-y}\text{Cr}_y\text{O}_3)/\text{GaN}$ photocatalysts.

CHAPTER 4

Nature of Catalytic Active Surface Sites Present on Bulk

$(\text{Ga}_{1-x}\text{Zn}_x)(\text{N}_{1-x}\text{O}_x)$ Photocatalysts

Abstract

The supported mixed oxide $(\text{Rh}_{2-y}\text{Cr}_y\text{O}_3)/(\text{Ga}_{1-x}\text{Zn}_x)(\text{N}_{1-x}\text{O}_x)$ and core/shell $(\text{Rh}^0/\text{Cr}_2\text{O}_3)/(\text{Ga}_{1-x}\text{Zn}_x)(\text{N}_{1-x}\text{O}_x)$ photocatalyst, active for splitting of H_2O , were synthesized, extensively characterized for their bulk and surface properties, and examined for water splitting with the objective of developing fundamental structure-photoactivity relationships. Raman and UV-vis spectroscopy revealed that the molecular and electronic structures, respectively, of the oxynitride $(\text{Ga}_{1-x}\text{Zn}_x)(\text{N}_{1-x}\text{O}_x)$ support are not perturbed by the deposition of the Rh-Cr NPs. Photoluminescence (PL) spectroscopy, however, showed that the oxynitride $(\text{Ga}_{1-x}\text{Zn}_x)(\text{N}_{1-x}\text{O}_x)$ support is the source of excited electrons/holes and the Rh-Cr NPs greatly reduce the undesirable recombination of photoexcited electron/holes by acting as efficient electron traps as well as increase the lifetimes of the excitons. High Resolution-XPS and High Sensitivity-LEIS surface analyses reveal that the surfaces of the Rh-Cr NPs consist of Rh^{+3} and Cr^{+3} mixed oxide NPs in spite of the desire to exclusively synthesize metallic

Rh^0 NPs that are encapsulated by Cr_2O_3 films for the core/shell catalysts. The function of the Rh-Cr-O mixed oxide NPs is to trap the excited electrons and holes to harness them for the photocatalytic splitting of water. The Rh^{+3} are the H_2 evolution sites and Cr^{+3} , GaZnO_x or their contact points are the possible O_2 evolution sites. The presence of some exposed metallic Rh^0 in the core/shell photocatalyst, however, decreases the photocatalytic efficiency relative to the mixed oxide photocatalyst by catalyzing the undesirable back reaction between H_2 and O_2 to form water. The current investigation establishes the fundamental structure-photoactivity relationships of these visible light activated photocatalysts. This is also the first study to employ High Sensitivity-Low Energy Ion Scattering to determine the composition of the outermost surface layers of photocatalysts that is critical for a complete understanding of complex, multicomponent photocatalysts.

4.1 Introduction

Throughout much of the 40 years of research on photocatalytic water splitting, efforts have been dedicated towards finding suitable materials that are able to produce H_2 and O_2 at significant quantum efficiency (Q.E.). The focus has been on discovering semiconductor mixed metal oxide materials that are able to efficiently produce H_2 and O_2 with $\text{NiO}/\text{NaTaO}_3\text{:La}$ being the most active semiconductor metal oxide photocatalyst system under UV irradiation with a Q.E. of 56% [1-4]. This achievement demonstrated that it is possible for a photocatalyst system to be more efficient than the targeted goal of 30% Q.E. for the start of commercialization of

photocatalytic hydrogen production on the industrial scale [3]. The goal, however, is for 30% Q.E. under visible light irradiation and not just UV light irradiation for semiconductor mixed metal oxide photocatalyst systems.

The research focus has now shifted towards the design of novel photocatalytic materials that are able to photocatalytic split water under visible light irradiation. The design of advanced, robust solar powered photocatalyst systems is the ultimate objective in photocatalysis research since the visible region covers a much larger portion of the sun's radiation compared to the narrow UV region [5]. The large band gap energies of semiconductor mixed metal oxides hinder their ability to fully utilize visible light energy. Only a few of these semiconductor mixed metal oxides (NiO/InTaO_4 (Q.E. = 0.7%) [6], $\text{RuO}_2/\text{InTaO}_4$ (Q.E. = 0.4%) [7] and $\text{RuO}_2/\text{YBiWO}_6$ (Q.E. = 0.2%) [8]) have been found to be able to perform the water splitting reaction under visible light excitation with very low quantum efficiencies.

In order to overcome the low Q.E. of mixed metal oxides, the Domen research group investigated the calcination of physically mixed metal oxides under NH_3 flow that form novel, advanced bulk mixed metal oxynitride materials, $(\text{Ga}_{1-x}\text{Zn}_x)(\text{N}_{1-x}\text{O}_x)$ and $(\text{Zn}_{1+x}\text{Ge})(\text{N}_2\text{O}_x)$, that are able to generate electron/hole pairs under visible light irradiation for photocatalytic water splitting [1, 9, 10]. Whereas GaN absorbs in the UV region (3.3 eV), the mixed $(\text{Ga}_{1-x}\text{Zn}_x)(\text{N}_{1-x}\text{O}_x)$ oxynitride solid solution absorbs in the visible region (2.4-2.8 eV with increasing ZnO lowering the band gap) that allows for absorption of visible light for electron/hole generation. The narrowing of the band gap is attributed to the presence of p-d repulsion between Zn3d and N2p electrons that

increases the valence band maximum allowing for visible light irradiation [11-13]. Although $(\text{Ga}_{1-x}\text{Zn}_x)(\text{N}_{1-x}\text{O}_x)$ generates electron/holes pairs in its bulk phase, it is unable to photocatalytically split water at its surface. Modification of the $(\text{Ga}_{1-x}\text{Zn}_x)(\text{N}_{1-x}\text{O}_x)$ with various transition metal oxides (Ni, Ru, Rh, Ir, and Pt), however, is able to activate the photocatalyst system for hydrogen and oxygen production [14]. The photoactivity was found to be further enhanced (between 2.5 – 860x) when the transition metal oxides were co-loaded with Cr_2O_3 . The co-loaded $(\text{Rh-Cr}_2\text{O}_3)/(\text{Ga}_{1-x}\text{Zn}_x)(\text{N}_{1-x}\text{O}_x)$ catalyst is the most active of all the oxynitride photocatalysts under visible light water splitting ($\lambda > 400\text{nm}$) with an optimized apparent Q.E of 5.9% [15-18].

Two different synthesis methods have been developed in the photocatalysis literature for the loading of Rh and Cr onto the $(\text{Ga}_{1-x}\text{Zn}_x)(\text{N}_{1-x}\text{O}_x)$ substrate. The first synthesis method involves a one-step co-impregnation of $\text{Na}_3\text{RhCl}_6 \cdot 2\text{H}_2\text{O}$ and $\text{Cr}(\text{NO}_3)_3 \cdot 9\text{H}_2\text{O}$ onto the $(\text{Ga}_{1-x}\text{Zn}_x)(\text{N}_{1-x}\text{O}_x)$ followed by calcination in air at 623K that forms supported $\text{Rh}_{2-y}\text{Cr}_y\text{O}_3$ mixed oxide nanoparticles (NPs) on the bulk $(\text{Ga}_{1-x}\text{Zn}_x)(\text{N}_{1-x}\text{O}_x)$ support. The supported $\text{Rh}_{2-y}\text{Cr}_y\text{O}_3$ NPs were proposed to be the catalytic active site for H_2 production and the bulk $(\text{Ga}_{1-x}\text{Zn}_x)(\text{N}_{1-x}\text{O}_x)$ support providing the active sites for O_2 production for this preparation technique [15]. The second synthesis method is a two-step process, aqueous $\text{Na}_3\text{RhCl}_6 \cdot 2\text{H}_2\text{O}$ is initially photodeposited onto the bulk $(\text{Ga}_{1-x}\text{Zn}_x)(\text{N}_{1-x}\text{O}_x)$ support, dried at 343 K, followed by Cr photodeposition from an aqueous K_2CrO_4 solution and again dried at 343 K. The motivation for this photodeposition synthesis method is to cover up the metallic Rh^0

NPs with a thin Cr_2O_3 layer creating a core/shell arrangement to prevent or minimize the O_2 and H_2 back reaction to form H_2O that readily takes place with exposed metallic Rh^0 [15]. It was proposed that H_2 evolves from the metallic Rh^0 component while the Cr_2O_3 shell prevents the O_2/H_2 back reaction to form water and that the bulk $(\text{Ga}_{1-x}\text{Zn}_x)(\text{N}_{1-x}\text{O}_x)$ provides the active sites for O_2 production [17]. These photocatalysis models were proposed from application of bulk characterization techniques and to fully understand these complex systems requires complementary surface characterization information since the catalytic splitting of water takes place at the surface of photocatalysts [19, 20]. The lack of surface information about the $(\text{Rh-Cr})/(\text{Ga}_{1-x}\text{Zn}_x)(\text{N}_{1-x}\text{O}_x)$ oxynitride photocatalysts prevents a fundamental understanding of the functioning of these novel materials and limits our ability to have guiding principles to design advanced visible light activated mixed oxynitride photocatalysts.

The present study utilizes cutting edge surface characterization methods (high-resolution X-ray photoelectron spectroscopy (HR-XPS) that analyzes ~1-3nm of the surface region and high-sensitivity low energy ion scattering (HS-LEIS) that analyzes ~0.3nm of outermost or topmost surface layer) for the $(\text{Rh-Cr})/(\text{Ga}_{1-x}\text{Zn}_x)(\text{N}_{1-x}\text{O}_x)$ photocatalyst systems prepared by the different synthesis methods. The fresh and used photocatalysts will be also compared to determine how their surfaces are affected by the photocatalytic water splitting environment. *In situ* optical spectroscopic characterization techniques (Raman, UV-vis, photoluminescence (PL) and time-resolved picosecond PL-Raman) will also be applied to provide further insights into

the bulk molecular and electronic structures to determine (i) how $(\text{Ga}_{1-x}\text{Zn}_x)(\text{N}_{1-x}\text{O}_x)$ differs from the bulk Ga_2O_3 and ZnO precursors, and (ii) how $\text{Rh}_{2-y}\text{Cr}_y\text{O}_3$ NPs affect the bulk properties of the $(\text{Ga}_{1-x}\text{Zn}_x)(\text{N}_{1-x}\text{O}_x)$ support. The photocatalytic activity of the two synthesis methods will also be determined to help develop fundamental structure-photoactivity relationships for these novel, advanced oxynitride photocatalysts for water splitting.

4.2 Experimental

4.2.1 Catalyst Synthesis

The $(\text{Ga}_{1-x}\text{Zn}_x)(\text{N}_{1-x}\text{O}_x)$ with $x=0.12$ as measured from energy-dispersive (EDX) analysis was synthesized by a nitridation method [13]. A mixture of Ga_2O_3 (High Purity Chemicals, 99.9%) and ZnO (Kanto Chemicals, 99%) in a 1:2 molar ratio was first well mixed in an agate mortar. The physical mixture was then calcined at 1123 K under NH_3 flow (250 ml/min) for 15 hours in a custom quartz nitridation reactor. For the co-impregnation synthesis method, the $(\text{Ga}_{1-x}\text{Zn}_x)(\text{N}_{1-x}\text{O}_x)$ was mixed in an evaporating dish with the aqueous precursors, $\text{Cr}(\text{NO}_3)_3 \cdot 9\text{H}_2\text{O}$ (Wako Pure Chemicals, 99.9%) and $\text{Na}_3\text{RhCl}_6 \cdot 2\text{H}_2\text{O}$ (Kanto Chemicals, 97% as Rh), yielding 1 wt.% Rh and 1.5wt.% Cr [15]. This suspension was then placed over a water bath and continuously stirred with a glass rod until complete evaporation. The powder was then collected and calcined in air at 623 K for one hour. The catalyst obtained from the co-impregnation method will be referred to as $(\text{Rh}_{2-y}\text{Cr}_y\text{O}_3)/(\text{Ga}_{1-x}\text{Zn}_x)(\text{N}_{1-x}\text{O}_x)$, so named in the literature. For the photodeposition synthesis method, the

(Ga_{1-x}Zn_x)(N_{1-x}O_x) powder is placed in a Pyrex inner irradiation-type reaction vessel connected to a glass closed gas circulation system in an aqueous solution (~370 ml) containing Na₃RhCl₆•2H₂O (Kanto Chemicals, 97% as Rh) [17] yielding 1 wt% Rh. After the system was evacuated, the reactor was irradiated with a 450 W high-pressure Hg lamp with a sodium nitrite aqueous solution as a filter to block ultraviolet light for 4 hours. The temperature of the reactant solution was maintained at room temperature by flowing cooling water. The powder was then separated from the solution via filtration, washed thoroughly with distilled water and dried overnight in an oven at 343 K. This procedure is then repeated where the Rh-deposited (Ga_{1-x}Zn_x)(N_{1-x}O_x) is placed in the Pyrex inner irradiation-type reaction vessel in an aqueous K₂CrO₄ solution yielding 2.5% Cr. After irradiation for 4 hours with a 450 W high-pressure Hg lamp with a sodium nitrite aqueous solution as a filter, the filtrated powder is washed thoroughly with distilled water and dried overnight in an oven at 343 K. The catalyst obtained from the photodeposition method will be referred to as (Rh/Cr₂O₃)/(Ga_{1-x}Zn_x)(N_{1-x}O_x) named so in the literature.

4.2.2 Raman Spectroscopy

Raman spectroscopy was utilized to obtain the molecular structure of the fresh photocatalysts and was performed on a Lab Ram-HR Raman spectrometer (Horiba-Jobin Yvon) equipped with visible (442 and 532 nm) laser excitation and utilizing a confocal microscope (Olympus BX-30) for focusing the laser on the catalyst sample. The 532nm visible laser excitation was generated by Nd:YAG laser (10 mW) and the 442 visible laser excitation was generated by a He-Cd laser (~7 mW) with the

scattered photons directed into a single monochromator and focused onto a UV-sensitive liquid-N₂ cooled CCD detector (Horiba-Jobin Yvon CCD-3000V) having a spectral resolution of $\sim 2 \text{ cm}^{-1}$ for the given parameters. About 5-10 mg of the catalyst was placed into a high temperature *in situ* cell (Linkam TS-1500) with a quartz window and the spectrums were obtained under ambient conditions. The spectral acquisition time employed was 5 scans of 5 seconds/scan for each spectrum. System alignment was verified using a silica reference standard line at 520.7 cm^{-1} .

4.2.3 UV-Vis NIR Diffuse Reflectance Spectroscopy (DRS)

Ultra Violet-visible-Near Infrared (UV-vis-NIR) diffuse reflectance spectroscopy (DRS) was utilized to obtain the optical edge energy, E_g , values for the fresh photocatalysts. Spectra were obtained using a Varian Cary 5E UV-vis spectrophotometer with a diffuse reflectance attachment (Harrick Praying Mantis Attachment, DRA-2). The finely ground powder catalyst samples ($\sim 20 \text{ mg}$) were loaded into an *in situ* cell (Harrick, HVC-DR2) and measured in the 200-800 nm spectral region with a magnesium oxide reflectance standard used as the baseline. A filter (Varian, 1.5ABS) was employed to minimize the background noise. A magnesium oxide white reflectance standard baseline was collected under ambient conditions. Determination of the Kubelka-Munk function, $F(R_\infty)$, was obtained from the UV-vis DRS absorbance and processed with Microsoft Excel software. The edge energy was determined by finding the intercept of the straight line in the low-energy

rise of a plot of $[F(R_{\infty})h\nu]^{1/n}$, where $n = 0.5$ for the direct allowed transition versus $h\nu$, where $h\nu$ is the energy of the incident photon [21-23].

4.2.4 High Resolution X-ray Photoelectron (HR-XPS) Spectroscopy

The HR-XPS spectra of the fresh and used photocatalysts were obtained on a Scienta ESCA 300 spectrometer equipped with a 300 mm hemispherical electrostatic analyzer and a monochromatic Al K α X-ray source with energy of 1486.6 eV generated from a rotating anode. This allows for improved chemical selectivity by narrowing the spectral peaks of elements and greatly reducing the spectral background signal compared to conventional XPS spectrometers. Each spectrum was calibrated using a binding energy (BE) value of 285.0 eV for carbon in the C1s region. The atomic concentration ratios were calculated by correcting the measured peak area ratios with relative sensitivity factors employed in the Casa XPS software version 2.3.15.

4.2.5 High Sensitivity Low Energy Ion Scattering (HS-LEISS)

Spectroscopy

Analysis of the outermost surface layer of the fresh and used photocatalysts was obtained on the Qtac¹⁰⁰ HS-LEIS Spectrometer (ION-TOF) equipped with a highly sensitive double toroidal analyzer, 3000 times higher sensitivity than conventional LEIS spectrometers, which allows for static depth profiling. The photocatalyst samples were first gently cleaned with atomic oxygen to remove surface hydrocarbon contamination from the atmosphere prior to being transferred inside the

analysis chamber. The HS-LEIS spectra were taken using both 4000 eV $^4\text{He}^+$ with 7245 pA current and 3000 eV $^{20}\text{Ne}^+$ with 2959 pA current as ion sources. TOF mass filters were also utilized for spectra obtained with Ne^+ as an ion source for reduced flux background at low kinetic energies. For depth profiling, the surface was sputtered by Ar^+ gas at 500 eV at a sputter yield of 1×10^{15} ions/cm². Metallic Rh and Cr standards were also analyzed for quantifying the elemental composition of the photocatalysts.

4.2.6 Photoluminescence Spectroscopy and Photoluminescent Decay

Spectrally resolved PL spectra and transient PL lifetime measurements of the fresh photocatalysts were conducted using a Ti:sapphire laser (Coherent Mira 900), tunable in the 685-1000 nm spectra range, generating 5 ps pulses with a 76 MHz repetition rate, pumped with a frequency-doubled Nd:YVO₄ laser (Coherent Verdi V-18). The output of the laser was frequency doubled using an ultrafast harmonic generator (Coherent 5-050). To perform the luminescence measurements, the excitation light at 400 nm was directed toward a microscope of a tunable micro-, macro-Raman/photoluminescence system (Jobin Yvon Horiba, T6400) and was focused using a long distance objective (50x, N/A=0.5) onto a sample to a spot size of $\sim 2 \mu\text{m}$. The photocatalyst sample was placed into a high temperature *in situ* microscopy stage (Linkam, TS-1500) and pretreated as follows: The samples were heated at 10 °C/min to 673 K in flowing 10% O₂/N₂ (30 sccm) to remove water, since moisture causes quenching of the PL signal [24], and to fully oxidize the samples. Upon cooling to room temperature in flowing inert gas (N₂, 30 sccm), the

photoluminescence decay measurements were made. To obtain complete PL spectra, the spectrometer was set to nanometer mode and the grating was moved several times in order to obtain the intensity over a 400 to 800 nm range. The luminescence light was collected through the same objective in backscattering geometry and focused onto a slit of the triple-monochromator equipped with a fast gated intensified charge coupled device (ICCD) camera collecting in the 350-900 nm range (LaVision, Picostar HR12). The ICCD camera was gated using a sequence of 76 MHz pulses propagating with a variable delay relative to the original train of trigger pulses (76 MHz) from a photodiode in a Ti:sapphire laser. The minimum gate width was 300 ps and the maximum delay was defined by the laser repetition rate (~13.2 ns). The laser energy at the sample was maintained at approximately 1.6 mW to prevent photo-degradation of the photocatalyst sample. The grating was set to monitor decay centered at emission wavelengths from 500 to 700 nm. The grating setting used to monitor PL lifetimes decay was based on the PL peak maximum from the PL spectra. Experimental decay curves were then fit to a double first-order exponential decay model to account for an observed “fast” (t_1) and “slow” (t_2) components [25, 26]:

$$y = A1 \cdot \exp\left(\frac{-t}{t1}\right) + A2 \cdot \exp\left(\frac{-t}{t2}\right) + y0 \quad (1)$$

4.2.7 Photocatalytic Water Splitting

About 0.1 g of the photocatalyst powder was placed in a top down Pyrex reactor cell filled with 100 ml of distilled water. A magnetic stirrer was also placed in the reactor to allow for continuous stirring of the suspension. The reactor was then

attached to a closed-gas circulation system connected to a vacuum pump. Air in the system was removed prior to the reaction so no atmospheric oxygen can be detected in the system. A Xe arc lamp was used to irradiation the sample for the reaction and cut-off filters were utilized to only allow $\lambda > 400$ nm. A Liebig condenser connected to the closed gas circulation system was used to prevent gas phase water from escaping the reactor so only H₂ and O₂ products can be found in the rest of the closed gas circulation system. A cooling water system was also utilized to keep the reactor at room temperature. A gas chromatograph was used to measure H₂, O₂, and N₂ products in the system. After the reaction, the used catalysts were filtered out from the suspension to allow for further surface analysis (HR-XPS and HS-LEISS).

4.3 Results

4.3.1 Bulk Molecular Structures

The Raman spectra for the bulk Ga₂O₃ and ZnO precursors used for the synthesis of the (Ga_{1-x}Zn_x)(N_{1-x}O_x) are shown in Figure 1. The bulk Ga₂O₃ contains Raman bands characteristic of β -Ga₂O₃ [27, 28]: bands below 200 cm⁻¹ are assignable to the translation and libration of GaO₄ and Ga₂O₆ chains, bands between 300–500 cm⁻¹ are assigned to Ga₂O₆ symmetric stretching and bending modes, and higher frequency bands between 500–700 cm⁻¹ are from GaO₄ stretching and bending modes. The Raman spectrum of ZnO contains bands from phonon modes indicative of the ZnO wurtzite structure [29]: the bands between 100-540 cm⁻¹ are dominated by acoustic phonon modes, the bands between 540-820 cm⁻¹ originate from optical and

acoustic phonons modes, and bands between 820-1200 cm^{-1} are from optical phonon modes and their overtones.

The Raman spectra of the synthesized $(\text{Ga}_{1-x}\text{Zn}_x)(\text{N}_{1-x}\text{O}_x)$ and $(\text{Rh}_{2-y}\text{Cr}_y\text{O}_3)/(\text{Ga}_{1-x}\text{Zn}_x)(\text{N}_{1-x}\text{O}_x)$ are presented in Figure 2. The $(\text{Ga}_{1-x}\text{Zn}_x)(\text{N}_{1-x}\text{O}_x)$ contains strong bands below 200 cm^{-1} that can be attributed to the translation and libration modes of GaO_4 and Ga_2O_6 chains similar to the for bulk Ga_2O_3 . The band at 332 cm^{-1} has been assigned to multiple photon modes of ZnO and can be assigned to a phonon mode in the $(\text{Ga}_{1-x}\text{Zn}_x)(\text{N}_{1-x}\text{O}_x)$ solid solution while the 637 cm^{-1} is from the O-Zn-O local structure in the $(\text{Ga}_{1-x}\text{Zn}_x)(\text{N}_{1-x}\text{O}_x)$ solid solution [30]. The Raman bands at 412, 556, and 717 cm^{-1} are indicative of GaN optical phonon modes in the $(\text{Ga}_{1-x}\text{Zn}_x)(\text{N}_{1-x}\text{O}_x)$ solid solution [30, 31]. The Raman spectra suggest that the $(\text{Ga}_{1-x}\text{Zn}_x)(\text{N}_{1-x}\text{O}_x)$ oxynitride also contains impure phases of Ga_2O_3 , GaN and ZnO . The Raman spectrum of $(\text{Rh}_{2-y}\text{Cr}_y\text{O}_3)/(\text{Ga}_{1-x}\text{Zn}_x)(\text{N}_{1-x}\text{O}_x)$ does not differ noticeably from the Raman spectrum of the bulk $(\text{Ga}_{1-x}\text{Zn}_x)(\text{N}_{1-x}\text{O}_x)$ phase. Crystalline Cr_2O_3 characteristic Raman bands at 542 and 603 cm^{-1} [32, 33] are not detected, which may be due to overlap with the bulk $(\text{Ga}_{1-x}\text{Zn}_x)(\text{N}_{1-x}\text{O}_x)$ vibrations. The weak and broad Rh_2O_3 Raman band at 550 cm^{-1} [34] is also not detected because of the strong bulk $(\text{Ga}_{1-x}\text{Zn}_x)(\text{N}_{1-x}\text{O}_x)$ vibrations. Although Raman spectroscopy does not provide information about the supported $\text{Rh}_{2-y}\text{Cr}_y\text{O}_3$ NPs, it does reveal that the bulk molecular structure of the $(\text{Ga}_{1-x}\text{Zn}_x)(\text{N}_{1-x}\text{O}_x)$ support is not modified by the addition of the $\text{Rh}_{2-y}\text{Cr}_y\text{O}_3$ NPs.

4.3.2 Bulk Electronic Structures

The UV-vis DRS optical bulk E_g values of the photocatalysts are tabulated in Table 1. The bulk band gap energy values for β -Ga₂O₃ (4.7 eV or 264 nm absorption edge) and ZnO (3.2 eV or 388 nm) are in agreement with previously reported E_g values [13, 35]. The bulk band gap energy for the (Ga_{1-x}Zn_x)(N_{1-x}O_x) is 2.6 eV (477 nm) and falls in the reported range of 2.4-2.8 eV (442 - 517 nm) for visible light active (Ga_{1-x}Zn_x)(N_{1-x}O_x) materials [13]. Deposition of Rh_{2-y}Cr_yO₃ NPs on the (Ga_{1-x}Zn_x)(N_{1-x}O_x) support essential does not perturb the overall band gap energy of the composite photocatalyst.

4.3.3 Atomic Composition of Surface Region (~1-3nm)

The atomic composition obtained from the XPS survey spectrum for the bulk (Ga_{1-x}Zn_x)(N_{1-x}O_x) is shown in Table 2. No contaminants were detected in the sample and the O concentration was found to be slightly higher (15%) compared to the bulk concentration (12%). The XPS survey spectra of the fresh and used supported (Rh_{2-y}Cr_yO₃)/(Ga_{1-x}Zn_x)(N_{1-x}O_x) photocatalysts are compared in Figure 3. The surface region of the fresh (Rh_{2-y}Cr_yO₃)/(Ga_{1-x}Zn_x)(N_{1-x}O_x) consists primarily of Ga, Zn, Cr, O, N and Rh with some Na and Cl residual contaminants from the Na₃RhCl₆•2H₂O precursor. Compared to the bulk (Ga_{1-x}Zn_x)(N_{1-x}O_x), the O concentration was found to increase while the N and Ga concentration decreased showing the surface region became oxidized after the calcination procedure. After being employed as a photocatalyst for the splitting of water, the surface Na contaminant is gone and the surface Cl concentration decreased by more than 50% most probably because of their

aqueous solubility. The elemental composition of the surface regions for both photocatalysts are compared in Table 3 and indicate an increase of O, but almost the same concentrations of Ga, Zn, Cr, O, N and Rh. This trend suggests that the Na and Cl contaminants were occupying some of the O sites in the surface region of the photocatalyst.

The XPS survey spectra (not shown for brevity) for the fresh and used supported $(\text{Rh}/\text{Cr}_2\text{O}_3)/(\text{Ga}_{1-x}\text{Zn}_x)(\text{N}_{1-x}\text{O}_x)$ photocatalysts did not exhibit any contaminants from the K_2CrO_4 precursor. The atomic compositions obtained from the XPS survey spectra for the supported $(\text{Rh}/\text{Cr}_2\text{O}_3)/(\text{Ga}_{1-x}\text{Zn}_x)(\text{N}_{1-x}\text{O}_x)$ photocatalysts are listed in Table 4. The used photocatalyst was found to possess slightly less O (5.3 %), and slightly more N (3.3%) and Ga (2.0%) while the concentration of the other elements staying relatively constant in the surface region. These changes are within the margin of error ($\pm 5\%$) for the XPS spectrometer and, thus, surface composition of the supported $(\text{Rh}/\text{Cr}_2\text{O}_3)/(\text{Ga}_{1-x}\text{Zn}_x)(\text{N}_{1-x}\text{O}_x)$ photocatalyst remained relatively constant during photocatalytic splitting. In addition, all the photocatalysts contained $\sim 1\%$ Rh and $\sim 5\%$ Cr for the supported $(\text{Rh}_{2-y}\text{Cr}_y\text{O}_3)/(\text{Ga}_{1-x}\text{Zn}_x)(\text{N}_{1-x}\text{O}_x)$ photocatalyst while the supported $(\text{Rh}/\text{Cr}_2\text{O}_3)/(\text{Ga}_{1-x}\text{Zn}_x)(\text{N}_{1-x}\text{O}_x)$ photocatalysts contained $\sim 3.5\%$ Cr in the surface region.

The HR-XPS spectra for Cr 2p and Rh 3d peaks in the surface region were also collected in order to determine their oxidation states. The Cr 2p and Rh 3d transitions for the supported $(\text{Rh}_{2-y}\text{Cr}_y\text{O}_3)/(\text{Ga}_{1-x}\text{Zn}_x)(\text{N}_{1-x}\text{O}_x)$ photocatalysts are presented in Figure 4 and reveals the presence of only Cr^{3+} and Rh^{3+} species in the surface region.

Neither Cr^{6+} or metallic $\text{Rh}(0)$ species were found for these photocatalysts in the surface region. The Cr 2p and Rh 3d peaks for the supported $(\text{Rh}/\text{Cr}_2\text{O}_3)/(\text{Ga}_{1-x}\text{Zn}_x)(\text{N}_{1-x}\text{O}_x)$ core/shell photocatalysts are presented in Figure 5. The Cr 2p region reveals the existence of only Cr^{3+} without any Cr^{6+} species. The peak in the Rh 3d region shows that Rh^{3+} is the dominant Rh phase on the surface with only a small shoulder corresponding to the presence of a trace of metallic $\text{Rh}(0)$.

4.3.4 Atomic Composition of Outermost Surface Layer (~0.3nm)

The atomic composition of the outermost surface layer (~0.3 nm) and the layers beneath the topmost surface layer of the photocatalysts were analyzed by HS-LEIS spectroscopy depth profiling. The HS-LEIS spectra for the $(\text{Ga}_{1-x}\text{Zn}_x)(\text{N}_{1-x}\text{O}_x)$ support using both $^4\text{He}^+$ and $^{20}\text{Ne}^+$ as ion gas sources are presented in Figures 6A and 6B. Resolvable peaks for the N, O and Zn/Ga in the outermost surface layer with the $^4\text{He}^+$ gas ion source are shown in Figure 6A. The atomic oxygen pretreatment cleaned off hydrocarbons deposited on the surface which did not affect the surface composition of the other elements and increased signal intensity for the sample. The other photocatalyst samples were also pretreated with atomic oxygen and the surface composition of non-carbon elements were likewise not affected. The close atomic masses of Zn and Ga did not allow for resolution between these two elements using He^+ and Ne^+ gas ions as shown in Figure 6B. Further attempts were made to resolve these two elements with the heavier $^{40}\text{Ar}^+$ gas ions, but resolving the Ga and Zn signals was also unsuccessful.

The HS-LEIS depth profiles for fresh $(\text{Rh}_{2-y}\text{Cr}_y\text{O}_3)/(\text{Ga}_{1-x}\text{Zn}_x)(\text{N}_{1-x}\text{O}_x)$ using both $^4\text{He}^+$ and $^{20}\text{Ne}^+$ as ion gas sources are presented in Figures 7A and 7B. The HS-LEIS resolvable peaks are for the O, Na, Cl, Cr, Zn/Ga, and Rh in the outermost surface layer with the $^4\text{He}^+$ gas ion source are shown in Figure 7A. The absence of a peak for N is possibly due to the slow velocity of the $^4\text{He}^+$ gas ions which makes it difficult to obtain good elemental sensitivity for low mass elements like N without the use of $^3\text{He}^+$ as gas ion source [36]. The evolution of the HS-LEIS signals for Cl, Na and Zn/Ga, normalized against the relatively constant O signal, are shown in Figure 8 during the dynamic depth profiling. The Cl and Na contaminants slightly decrease with depth profiling reflecting some surface enrichment of Na and Cl. The Zn/Ga signal significantly increases during the depth profiling as expected for the bulk nature of the Zn and Ga oxides. The HS-LEIS signals for Cr and Rh are more easily resolved with Ne^+ gas ions as seen in Figure 7B. The Rh and Cr signals were calibrated against metallic Rh and Cr standards in order to quantify these two elements as shown in Figure 9. The outermost surface layer contains slightly more Rh than Cr, and the Cr concentration markedly increase with depth profiling while that of Rh markedly decreases. These concentration profiles reveal that Rh is surface segregated while Cr becomes more prevalent with increasing depth. The ~5 times greater concentration of Cr at the end of the depth profile is much higher than the expected ~1.5 times greater Cr expected from the catalysts loading.

The HS-LEIS depth profiles for the used supported $(\text{Rh}_{2-y}\text{Cr}_y\text{O}_3)/(\text{Ga}_{1-x}\text{Zn}_x)(\text{N}_{1-x}\text{O}_x)$ photocatalyst are presented in Figure 10. A very small

shoulder for N is visible in the depth profile of Figure 10A indicating that N is being exposed on the surface of the supported $(\text{Rh}_{2-y}\text{Cr}_y\text{O}_3)/(\text{Ga}_{1-x}\text{Zn}_x)(\text{N}_{1-x}\text{O}_x)$ photocatalysts during the water splitting reaction. Traces of the Na and Cl contaminants are not detected during HS-LEIS depth profiling, unlike XPS analysis of the surface region, which suggests that the trace Cl contaminant is not present on the outermost surface layers of this used photocatalyst. The Rh and Cr depth profiles for the used $(\text{Rh}_{2-y}\text{Cr}_y\text{O}_3)/(\text{Ga}_{1-x}\text{Zn}_x)(\text{N}_{1-x}\text{O}_x)$ photocatalyst in Figure 11 reveal comparable amounts of Rh and Cr on the outermost surface and the Cr concentration increases while the Rh concentration decreases with depth profiling as found for the fresh $(\text{Rh}_{2-y}\text{Cr}_y\text{O}_3)/(\text{Ga}_{1-x}\text{Zn}_x)(\text{N}_{1-x}\text{O}_x)$ photocatalyst. The similar depth profile trends for the Rh and Cr for the fresh and used supported $(\text{Rh}_{2-y}\text{Cr}_y\text{O}_3)/(\text{Ga}_{1-x}\text{Zn}_x)(\text{N}_{1-x}\text{O}_x)$ photocatalysts suggests a static situation exists during photocatalysis for the supported $(\text{Rh}_{2-y}\text{Cr}_y\text{O}_3)$ NPs.

The HS-LEIS depth profiles for the fresh supported $(\text{Rh}/\text{Cr}_2\text{O}_3)/(\text{Ga}_{1-x}\text{Zn}_x)(\text{N}_{1-x}\text{O}_x)$ core/shell photocatalyst are presented in Figure 12 and show that the outer surface region is void of any contaminants and N. The Cr and Rh depth profiles for the fresh supported $(\text{Rh}/\text{Cr}_2\text{O}_3)/(\text{Ga}_{1-x}\text{Zn}_x)(\text{N}_{1-x}\text{O}_x)$ core/shell photocatalyst are shown in Figure 13 and reveal that the outermost layers contain about twice as much Rh as Cr. With increasing depth from the outer surface, the concentration of Cr decreases only slightly while that of Rh falls rapidly and becomes lower than that of Cr at the end of the sputtering. The corresponding HS-LEIS depth profiles for the used supported $(\text{Rh}/\text{Cr}_2\text{O}_3)/(\text{Ga}_{1-x}\text{Zn}_x)(\text{N}_{1-x}\text{O}_x)$ core/shell

photocatalysts are presented in Figure 14 and the main spectral difference with the fresh core/shell photocatalyst is the existence of some N (see Figure 14A). The appearance of N in the outermost layers was also found for the used supported $(\text{Rh}_{2-y}\text{Cr}_y\text{O}_3)/(\text{Ga}_{1-x}\text{Zn}_x)(\text{N}_{1-x}\text{O}_x)$ mixed oxide photocatalyst suggests possible surface enrichment during the photocatalytic water splitting reaction. The HS-LEIS Cr and Rh depth profiles for the used supported $(\text{Rh}/\text{Cr}_2\text{O}_3)/(\text{Ga}_{1-x}\text{Zn}_x)(\text{N}_{1-x}\text{O}_x)$ core/shell photocatalyst are given in Figure 15 and the trend is similar to that of the fresh supported $(\text{Rh}/\text{Cr}_2\text{O}_3)/(\text{Ga}_{1-x}\text{Zn}_x)(\text{N}_{1-x}\text{O}_x)$ core/shell photocatalyst: Rh concentration is about twice as great in the outermost layers and rapidly decreases while the Cr concentration only slightly decreases with increasing depth. Also found for the supported $(\text{Rh}_{2-y}\text{Cr}_y\text{O}_3)/(\text{Ga}_{1-x}\text{Zn}_x)(\text{N}_{1-x}\text{O}_x)$ mixed oxide photocatalysts, the Rh and Cr depth profile concentrations for the supported $(\text{Rh}/\text{Cr}_2\text{O}_3)/(\text{Ga}_{1-x}\text{Zn}_x)(\text{N}_{1-x}\text{O}_x)$ core/shell photocatalysts are not altered by the photocatalytic reaction environment.

4.3.5 Dynamics of Photoexcited Electrons and Holes

The photoluminescence (PL) emission spectrum monitors the recombination dynamics of excited electrons and holes. The PL intensity is indicative of the population of electron/hole recombination centers (self-trapped electrons, oxygen vacancies, defect sites, impurities, reduced metal ions, etc.) in the bulk phase of excited photocatalysts with high intensity reflecting a greater number of recombination centers [24, 37]. The PL emission spectra of bulk ZnO , Ga_2O_3 and $(\text{Ga}_{1-x}\text{Zn}_x)(\text{N}_{1-x}\text{O}_x)$ photocatalysts in response to laser excitation at 400 nm are presented in Figure 16 and their peak maxima are listed in Table 1. The much lower

PL emissions intensities for bulk ZnO and Ga₂O₃ might at first suggest that these oxides appear to be more suitable photocatalysts than the (Ga_{1-x}Zn_x)(N_{1-x}O_x) oxynitride, but the low PL emissions intensities are actually a consequence of the 400 nm excitation energy being lower than their optical band gap energy values (388 and 264 nm). The optical absorption edge values for bulk ZnO and Ga₂O₃ are in the UV-range, thus, the lack of PL emissions is due to the use of visible light irradiation causing a decreased population of excited electrons being able to recombine. The addition of the (Rh_{2-y}Cr_yO₃) NPs greatly diminishes the PL emissions of the (Ga_{1-x}Zn_x)(N_{1-x}O_x) showing that electron/hole recombination is decreased in the presence of the supported NPs because of electrons being trapped and unable to recombine with holes in the bulk phase to produce emission.

The photoluminescence emission decay curves for the bulk ZnO, Ga₂O₃ and oxynitride photocatalysts are plotted in Figure 17. The PL emission decays for all the photocatalysts were modeled with Equation 1 that is based on two different species of electrons decaying at different rates and the fit parameters are given in Table 1. The parameters t₁ and A₁ refer to decay constant and amplitude of the “fast” component of electron decay while t₂ and A₂ refer to the decay constant and amplitude of the “slow” component of electron decay. Comparison of the PL emission decays from the bulk ZnO, Ga₂O₃ and (Ga_{1-x}Zn_x)(N_{1-x}O_x) indicates that both t₁ and t₂ increase with decreasing optical band gap energy, which is indicative of longer lifetimes of photo-generated electron/hole pairs [38, 39]. Deposition of the (Rh_{2-y}Cr_yO₃) NPs on the

$(\text{Ga}_{1-x}\text{Zn}_x)(\text{N}_{1-x}\text{O}_x)$ support prolongs the lifetime of excited electrons/holes in this multicomponent photocatalyst system.

4.3.6 Photocatalytic Water Splitting

The evolution of the H_2 and O_2 products from steady-state photocatalytic water splitting was monitored over 7 hours for the supported $(\text{Rh}_{2-y}\text{Cr}_y\text{O}_3)/(\text{Ga}_{1-x}\text{Zn}_x)(\text{N}_{1-x}\text{O}_x)$ mixed oxide and supported $(\text{Rh}/\text{Cr}_2\text{O}_3)/(\text{Ga}_{1-x}\text{Zn}_x)(\text{N}_{1-x}\text{O}_x)$ core/shell photocatalysts and are presented in Figure 18. Both photocatalysts were able to produce H_2 and O_2 at the proper 2:1 stoichiometric ratio. The production rate (units of $\mu\text{mol}/\text{g catalyst}/\text{h}$) for the supported $(\text{Rh}_{2-y}\text{Cr}_y\text{O}_3)/(\text{Ga}_{1-x}\text{Zn}_x)(\text{N}_{1-x}\text{O}_x)$ mixed oxide photocatalyst was 161 for H_2 and 79.4 for O_2 while the production rate for the supported $(\text{Rh}/\text{Cr}_2\text{O}_3)/(\text{Ga}_{1-x}\text{Zn}_x)(\text{N}_{1-x}\text{O}_x)$ core/shell photocatalyst was 71.1 for H_2 and 33.4 for O_2 . The BET surface areas of both photocatalyst systems were dominated by that of the $(\text{Ga}_{1-x}\text{Zn}_x)(\text{N}_{1-x}\text{O}_x)$ oxynitride support at $8 \text{ m}^2/\text{g}$ [13], and the surface area normalized activities (units of $\mu\text{mol}/\text{m}^2/\text{h}$) for the supported $(\text{Rh}_{2-y}\text{Cr}_y\text{O}_3)/(\text{Ga}_{1-x}\text{Zn}_x)(\text{N}_{1-x}\text{O}_x)$ mixed oxide photocatalyst are $20.1 \text{ H}_2/9.9 \text{ O}_2$ and $8.9 \text{ H}_2/4.2 \text{ O}_2$ for the supported $(\text{Rh}/\text{Cr}_2\text{O}_3)/(\text{Ga}_{1-x}\text{Zn}_x)(\text{N}_{1-x}\text{O}_x)$ core/shell photocatalyst. Thus, the supported $(\text{Rh}_{2-y}\text{Cr}_y\text{O}_3)/(\text{Ga}_{1-x}\text{Zn}_x)(\text{N}_{1-x}\text{O}_x)$ mixed oxide photocatalyst is slightly more than 2 times as active as the supported $(\text{Rh}/\text{Cr}_2\text{O}_3)/(\text{Ga}_{1-x}\text{Zn}_x)(\text{N}_{1-x}\text{O}_x)$ core/shell photocatalyst. No formation of N_2 was detected and indicates that N_3^- oxidation to N_2 did not occur at the surface of the oxynitride photocatalysts [13].

4.4 Discussion

4.4.1 Bulk and Electronic Structures of the $(\text{Ga}_{1-x}\text{Zn}_x)(\text{N}_{1-x}\text{O}_x)$ Oxynitride

Support

The bulk molecular structure of the oxynitride support was confirmed to be the $(\text{Ga}_{1-x}\text{Zn}_x)(\text{N}_{1-x}\text{O}_x)$ solid solution with Raman spectroscopy (see Figure 2). The corresponding UV-vis spectrum confirms that the $(\text{Ga}_{1-x}\text{Zn}_x)(\text{N}_{1-x}\text{O}_x)$ oxynitride phase is a solid solution and is not just a physical mixture of Ga_2O_3 , ZnO and GaN materials for its synthesis. The presence of small amounts of beta- Ga_2O_3 , ZnO and GaN NPs, which presumably reside on the surface of the oxynitride solid solution support, were also detected with Raman spectroscopy. The bulk molecular and electronic structures of the $(\text{Ga}_{1-x}\text{Zn}_x)(\text{N}_{1-x}\text{O}_x)$ oxynitride support phase were not perturbed by the deposition of the $(\text{Rh}_{2-y}\text{Cr}_y\text{O}_3)$ mixed oxide NPs as reflected in the resulting Raman and UV-vis spectra (see Figures 2 and Table 1). Thus, the deposition of the $(\text{Rh}_{2-y}\text{Cr}_y\text{O}_3)$ mixed oxide NPs onto the surface $(\text{Ga}_{1-x}\text{Zn}_x)(\text{N}_{1-x}\text{O}_x)$ support had almost no measurable effect on the bulk oxynitride phase.

4.4.2 Atomic Distribution of the Surface Region of Supported $(\text{Ga}_{1-x}\text{Zn}_x)(\text{N}_{1-x}\text{O}_x)$ Photocatalysts

4.4.2.1 Model of the Supported $(\text{Rh}_{2-y}\text{Cr}_y\text{O}_3)/(\text{Ga}_{1-x}\text{Zn}_x)(\text{N}_{1-x}\text{O}_x)$ Mixed Oxide Photocatalyst

Although the surface of the fresh supported $(\text{Rh}_{2-y}\text{Cr}_y\text{O}_3)/(\text{Ga}_{1-x}\text{Zn}_x)(\text{N}_{1-x}\text{O}_x)$ photocatalyst initially was contaminated with Na and Cl from the rhodium precursor,

Na and Cl were easily dissolved in the aqueous environment from the outermost surface layer ($\sim 0.3\text{nm}$) during photocatalysis. The Na is also completely absent from the surface region ($\sim 1\text{-}3\text{nm}$) of the used photocatalyst and the Cl concentration diminishes more than 50% from the surface region (Table 2). LEIS was able to show a small peak for N on the $(\text{Ga}_{1-x}\text{Zn}_x)(\text{N}_{1-x}\text{O}_x)$ which is not present for the $(\text{Rh}_{2-y}\text{Cr}_y\text{O}_3)/(\text{Ga}_{1-x}\text{Zn}_x)(\text{N}_{1-x}\text{O}_x)$. The surface region for the $(\text{Rh}_{2-y}\text{Cr}_y\text{O}_3)/(\text{Ga}_{1-x}\text{Zn}_x)(\text{N}_{1-x}\text{O}_x)$ was also found to be enriched with O relative to N (surface ~ 0.5 vs. bulk ~ 0.14), which is not too surprising since the deposited $(\text{Rh}_{2-y}\text{Cr}_y\text{O}_3)$ NPs do not possess any N. The lack of N on the $(\text{Rh}_{2-y}\text{Cr}_y\text{O}_3)/(\text{Ga}_{1-x}\text{Zn}_x)(\text{N}_{1-x}\text{O}_x)$ combined with the surface enriched O gives evidence for the existence of a GaZnO_x thin film on the surface of the $(\text{Ga}_{1-x}\text{Zn}_x)(\text{N}_{1-x}\text{O}_x)$ which arises due to the calcination treatment in air. The deposited $(\text{Rh}_{2-y}\text{Cr}_y\text{O}_3)$ NPs on the oxynitride support exclusively contain Cr^{3+} and Rh^{3+} species both in the fresh and used photocatalysts (see HR-XPS spectra in Figure 4). The Rh^{+3} species is surface enriched and its concentration significantly decreases with depth while the Cr^{+3} concentration increases with depth from the surface for the fresh and used photocatalysts (see HS-LEIS Figures 9 and 11). The increase in Cr^{3+} concentration with depth profile can be explained by the formation of some C_2O_3 NPs on the surface, dissolved Cr^{3+} in the GaZnO_x layer, and increased Cr^{3+} concentration in the $(\text{Rh}_{2-y}\text{Cr}_y\text{O}_3)$ NPs with depth from the surface. The increased Ga/Zn concentration with depth profiling indicates that Ga and Zn are not surface enriched (see HS-LEIS Figures 7 and 10). The lower XPS ratio of Ga to Zn in the surface region, ~ 5 , compared to the bulk, ~ 7 , suggests that Ga is depleted relative

to Zn in the surface region of the oxynitride support (see Table 2). A schematic of the structure of the supported $(\text{Rh}_{2-y}\text{Cr}_y\text{O}_3)/(\text{Ga}_{1-x}\text{Zn}_x)(\text{N}_{1-x}\text{O}_x)$ photocatalyst is depicted in Figure 19.

4.4.2.2 Model of the Supported $(\text{Rh}/\text{Cr}_2\text{O}_3)/(\text{Ga}_{1-x}\text{Zn}_x)(\text{N}_{1-x}\text{O}_x)$

Core/Shell Photocatalyst

The photodeposition synthesis method yielded a relatively contaminant-free photocatalyst whose surface did not contain the Na and Cl from the Rh precursor as well as the K from the Cr precursor. The lack of N on the outermost surface with surface enriched O shows that a GaZnO_x film covers the surface of the $(\text{Ga}_{1-x}\text{Zn}_x)(\text{N}_{1-x}\text{O}_x)$. Surface Cr^{3+} and Rh^{3+} are the dominant chemical states in the $\text{Rh}/\text{Cr}_2\text{O}_3$ core/shell NPs with only a small amount of metallic Rh^0 (see HR-XPS Figure 5). The Rh concentration in the outermost surface layer is almost ~ 2 is much as the Cr and much higher than the $\sim 1:1$ ratio for the supported $(\text{Rh}_{2-y}\text{Cr}_y\text{O}_3)/(\text{Ga}_{1-x}\text{Zn}_x)(\text{N}_{1-x}\text{O}_x)$ photocatalyst and its concentration significantly decreases with depth profiling (see HS-LEIS Figures 13 and 15). The most surprising new insights about the surface region is that Rh is fully oxidized and surface enriched given that the photodeposition synthesis was supposed to encapsulate the metallic Rh^0 NPs with a thin Cr_2O_3 film. There are two possibilities to explain why the Rh concentration is much higher on the outermost surface layer. The 2:1 Rh:Cr ratio on the surface can be attributed to Rh^0 NPs that were not fully encapsulated by the Cr_2O_3 shell and becomes oxidized forming a Rh^{3+} shell over the Rh^0 NP. The second possibility is that during the photodeposition synthesis the Rh was able to become

oxidized and diffuse through the Cr_2O_3 layer, presumably related to the Rh_2O_3 having similar structure as Cr_2O_3 and being the driving force to surface segregate. These surprising findings are in contrast to the supported core/shell model (metallic Rh core encapsulated by a Cr_2O_3 film) previously proposed [17]. The previous investigation employed bulk EXAFS/XANES to analyze the Rh and the bulk nature of this spectroscopic method indicates that the majority Rh species in the core/shell photocatalyst is indeed metallic Rh^0 , but provides no information about the surface region [17]. The current surface measurements, however, demonstrate that it is Rh^{+3} that is surface enriched in the topmost surface layer and surface region of the core/shell photocatalyst where the photocatalytic splitting of water takes place. The LEIS shows that the Cr concentration stays constant with depth indicating uniform Cr concentration in the Rh-Cr NPs along with the formation of some Cr_2O_3 NPs. A schematic of the supported $(\text{Rh}/\text{Cr}_2\text{O}_3)/(\text{Ga}_{1-x}\text{Zn}_x)(\text{N}_{1-x}\text{O}_x)$ core/shell photocatalyst is depicted in Figure 20.

4.4.3 Generation of Excited Electron/Hole Pairs and Their Lifetimes

Although the $(\text{Ga}_{1-x}\text{Zn}_x)(\text{N}_{1-x}\text{O}_x)$ phase is able to generate excited electrons/holes with visible light excitation, it is unable to photocatalytically split water at the surface/water interface [13]. The function of the bulk $(\text{Ga}_{1-x}\text{Zn}_x)(\text{N}_{1-x}\text{O}_x)$ phase, or support, of the multicomponent photocatalyst system is to generate excited electron/holes upon excitation by visible light. PL spectroscopy is able to measure the recombination of electrons/holes in the photocatalyst and the presence of the supported $(\text{Rh}_{2-y}\text{Cr}_y\text{O}_3)$ particles suppresses the PL signal of the bulk

(Ga_{1-x}Zn_x)(N_{1-x}O_x), which indicates that the supported (Rh_{2-y}Cr_yO₃) particles prevent recombination of electrons and holes. This suggests that the supported (Rh_{2-y}Cr_yO₃) mixed oxide particles are efficient electron traps that minimize electron and hole recombination and, thus, allow for their consumption at the surface for photocatalytic water splitting [24, 40, 41]. Transient PL spectroscopy is able to measure the lifetime of the excited electrons/holes from the decay emissions parameters based on the “slow” t₂ component and where the ratio $\frac{A_2}{A_1+A_2}$ is indicative of the relative population of these long lived electrons with slow emissions decay [38, 39]. The electron traps from the surface (Rh_{2-y}Cr_yO₃) were able to prolong the lifetimes of excited electrons/holes as shown in Table 1 from the increased lifetimes not only from the “slow” t₂ component of decay but also for “fast” t₁ component. The relative population of long lived excited electrons was also found to be enhanced by the surface (Rh_{2-y}Cr_yO₃). PL and transient PL decay spectroscopy demonstrated that the surface modified (Rh_{2-y}Cr_yO₃) possessed all of the measurable desired properties for an efficient photocatalyst system. The surface (Rh_{2-y}Cr_yO₃) decreased the recombination of electron/holes in the bulk by transferring them to the surface which increased the lifetimes and population of the excited electrons and holes. This greatly increases the probability for the photocatalytic splitting of H₂O into H₂ and O₂ at the surface. HS-LEISS depth profiling revealed that the Cr₂O₃ species is more concentrated than the Rh₂O₃ near the bulk is seen in Figure 9 so the Cr₂O₃ may be more responsible for these charge transfer effects.

4.4.4 Structure-Photoactivity Relationships for Splitting of H₂O by (Ga_{1-x}Zn_x)(N_{1-x}O_x) Photocatalysts

4.4.4.1 Supported (Rh_{2-y}Cr_yO₃)/(Ga_{1-x}Zn_x)(N_{1-x}O_x) Mixed Oxide Photocatalyst

The supported (Rh_{2-y}Cr_yO₃)/(Ga_{1-x}Zn_x)(N_{1-x}O_x) photocatalyst is a two component photosystem. The bulk (Ga_{1-x}Zn_x)(N_{1-x}O_x) support phase has a band gap of 2.6 eV that allows homogeneous generation of electrons and holes inside this phase with visible light activation. The bulk generated electrons and holes must avoid recombination and diffuse to the surface to be able to perform the photocatalytic reaction. The supported (Rh_{2-y}Cr_yO₃) mixed oxide NPs are the catalytic active sites that trap and harness the electrons and holes to perform photocatalytic splitting of water to H₂ [15]. It was previously shown that although supported Rh₂O₃/(Ga_{1-x}Zn_x)(N_{1-x}O_x) photocatalyst is able to split H₂O into H₂, it is unable to produce any significant O₂ [14]. Only when Cr₂O₃ is added to the supported Rh₂O₃/(Ga_{1-x}Zn_x)(N_{1-x}O_x) photocatalyst is the stoichiometric amount of O₂ simultaneously evolved [14]. These observations suggest that the function of the Rh⁺³ sites is to generate H₂ while the O₂ evolution site can exist at several points: on the Cr³⁺ sites, GaZnO_x or at their contact points (see Figure 19). There is not enough evidence to determine which the active site is but the surface analysis reveals those are the likely sites for O₂ evolution. The current HS-LEISS surface analysis reveals that the ideal surface composition for the (Rh_{2-y}Cr_yO₃) NPs consists of a ~ 1:1 ratio of Rh:Cr on the

outermost surface layer for the supported $(\text{Rh}_{2-y}\text{Cr}_y\text{O}_3)/(\text{Ga}_{1-x}\text{Zn}_x)(\text{N}_{1-x}\text{O}_x)$ photocatalysts.

4.4.4.2 Supported $(\text{Rh}/\text{Cr}_2\text{O}_3)/(\text{Ga}_{1-x}\text{Zn}_x)(\text{N}_{1-x}\text{O}_x)$ Core/Shell

Photocatalyst

The supported $(\text{Rh}/\text{Cr}_2\text{O}_3)/(\text{Ga}_{1-x}\text{Zn}_x)(\text{N}_{1-x}\text{O}_x)$ core/shell photocatalyst is a three-component system. The bulk oxynitride $(\text{Ga}_{1-x}\text{Zn}_x)(\text{N}_{1-x}\text{O}_x)$ support phase generates the bulk electrons and holes with visible light excitation. The supported metallic Rh NPs trap the electrons arriving at the $\text{Rh}/(\text{Ga}_{1-x}\text{Zn}_x)(\text{N}_{1-x}\text{O}_x)$ interface. The metallic Rh NPs are encapsulated by a film of $(\text{Rh}_{2-y}\text{Cr}_y\text{O}_3)$ that requires the electrons to diffuse from the metallic Rh NPs to the surface of the $(\text{Rh}_{2-y}\text{Cr}_y\text{O}_3)$ mixed oxides NPs to participate in the photocatalytic water splitting reaction.

The supported $(\text{Rh}/\text{Cr}_2\text{O}_3)/(\text{Ga}_{1-x}\text{Zn}_x)(\text{N}_{1-x}\text{O}_x)$ core/shell photocatalyst was designed to optimize evolution of H_2 [17]. Although metallic Rh is known as a good H_2 evolution photocatalyst, it also suffers from catalyzing the back reaction between H_2 and O_2 to water [3]. To minimize the back reaction by metallic Rh NPs it was proposed to encapsulate the metallic Rh NPS with a Cr_2O_3 film [17]. The current HS-LEIS analysis, however, reveals that some of the metallic Rh was able to become oxidized during Cr_2O_3 photodeposition and, surprisingly, to diffuse to the surface of the “encapsulating” chromia film (see Figure 12). This suggests that the supported core/shell photocatalyst may actually function similarly to the supported $(\text{Rh}_{2-y}\text{Cr}_y\text{O}_3)$ mixed oxide NPs where the Rh^{+3} evolves H_2 with Cr^{3+} , GaZnO_x or their contact points as the possible active sites for O_2 evolution. Although the metallic Rh component may

enhance the trapping of electrons and supply them to the $(\text{Rh}_{2-y}\text{Cr}_y\text{O}_3)$ mixed oxide film, the presence of some metallic Rh^0 is also detected in the surface region (see HR-XPS Figure 5) that catalyzes the undesirable back reaction between H_2 and O_2 to form water. Consequently, the supported $(\text{Rh}/\text{Cr}_2\text{O}_3)/(\text{Ga}_{1-x}\text{Zn}_x)(\text{N}_{1-x}\text{O}_x)$ core/shell photocatalyst is actually only ~50% as efficient as the supported $(\text{Rh}_{2-y}\text{Cr}_y\text{O}_3)/(\text{Ga}_{1-x}\text{Zn}_x)(\text{N}_{1-x}\text{O}_x)$ mixed oxide photocatalyst because the desired catalyst was not achieved in the photodeposition process [17]. The high 2:1 ratio for Rh:Cr found on the outermost surface layer may also be a factor in the decreased activity giving evidence for the possibility of exposed metallic Rh^0 NPs with a thin Rh^{3+} shell which were not encapsulated by the $(\text{Rh}_{2-y}\text{Cr}_y\text{O}_3)$ mixed oxide film. The model for the photocatalytic process is given in Figure 20.

4.5 Conclusions

The bulk and surface properties of supported $(\text{Rh}_{2-y}\text{Cr}_y\text{O}_3)/(\text{Ga}_{1-x}\text{Zn}_x)(\text{N}_{1-x}\text{O}_x)$ mixed oxide and $(\text{Rh}/\text{Cr}_2\text{O}_3)/(\text{Ga}_{1-x}\text{Zn}_x)(\text{N}_{1-x}\text{O}_x)$ core/shell visible light activated photocatalysts were investigated with bulk (Raman, UV-vis, and PL) and surface (HS-LEIS and HR-XPS) spectroscopic techniques. The bulk molecular and electronic structures of the oxynitride $(\text{Ga}_{1-x}\text{Zn}_x)(\text{N}_{1-x}\text{O}_x)$ support phase were not affected by the addition of the Rh-Cr NPs. The supported Rh-Cr NPs, however, affected the recombination of excited electrons and holes revealing their ability to trap electrons and holes and harness them for photocatalytic splitting of water. The $\text{Rh}_{2-y}\text{Cr}_y\text{O}_3$ NPs were responsible for evolution of the H_2 (Rh^{+3}) and several sites are proposed (Cr^{+3} ,

GaZnO_x or their contact points) for O₂ photocatalytic reaction products. The presence of some metallic Rh⁰ in the supported (Rh/Cr₂O₃)/(Ga_{1-x}Zn_x)(N_{1-x}O_x) core/shell photocatalysts is responsible for its lower water splitting efficiency because the metallic Rh⁰ catalyzes the undesirable backward reaction of H₂ and O₂ to water. This study establishes for the first time the fundamental structure-photoactivity relationships for the novel visible light active supported (Rh-Cr)/(Ga_{1-x}Zn_x)(N_{1-x}O_x) photocatalysts.

Acknowledgements

This research was financially supported by the Department of Energy grant: DOE-FG02-93ER14350. Special thanks goes out to Alexander Puretsky at the Center for Nanophase Materials Sciences at Oak Ridge National Laboratory and Charles Roberts for assistance with the PL experiments in conjunction with User Project CNMS2008-075. Thanks to A. Xiong, Dr. J. Kubota and Dr. K. Domen at the University of Tokyo for their assistance with the synthesis of the (Ga_{1-x}Zn_x)(N_{1-x}O_x) photocatalysts as well as generating the photocatalytic activity data. The assistance of Dr. A. Miller at Lehigh University in obtaining and interpreting the HR-XPS and HS-LEIS data is also gratefully acknowledged.

References

- [1] K. Maeda, K. Domen, "New Non-Oxide Photocatalysts Designed for Overall Water Splitting under Visible Light." *J. Phys. Chem. C*, **111**, 7851, (2007).
- [2] F.E. Osterloh, "Inorganic Materials as Catalysts for Photochemical Splitting of Water." *Chem. Mater.*, **20**, 35, (2008).
- [3] A. Kudo, Y. Miseki, "Heterogeneous photocatalyst materials for water splitting." *Chem. Soc. Rev.*, **38**, 253, (2009).
- [4] X. Chen, S. Shen, L. Guo, and S.S. Mao, "Semiconductor-based Photocatalytic Hydrogen Generation " *Chem. Rev.*, **110**, 6503, (2010).
- [5] K. Maeda, K. Domen, "Photocatalytic Water Splitting: Recent Progress and Future Challenges " *The Journal of Physical Chemistry Letters*, **1**, 2655, (2010).
- [6] Z. Zou, J. Ye, K. Sayama, and H. Arakawa, "Direct splitting of water under visible light irradiation with an oxide semiconductor photocatalyst." *Nature (London, U. K.)*, **414**, 625, (2001).
- [7] Z. Zou, H. Arakawa, "Direct water splitting into H₂ and O₂ under visible light irradiation with a new series of mixed oxide semiconductor photocatalysts." *J. Photochem. Photobiol. , A*, **158**, 145, (2003).

- [8] H. Liu, J. Yuan, W. Shangguan, and Y. Teraoka, "Visible-light-responding BiYWO₆ solid solution for stoichiometric photocatalytic water splitting." *J. Phys. Chem. C*, **112**, 8521, (2008).
- [9] K. Maeda, K. Teramura, N. Saito, Y. Inoue, H. Kobayashi, and K. Domen, "Overall water splitting using (oxy)nitride photocatalysts." *Pure Appl. Chem.*, **78**, 2267, (2006).
- [10] Y. Lee, H. Terashima, Y. Shimodaira, K. Teramura, M. Hara, H. Kobayashi, K. Domen, and M. Yashima, "Zinc germanium oxynitride as a photocatalyst for overall water splitting under visible light." *J. Phys. Chem. C*, **111**, 1042, (2007).
- [11] T. Hirai, K. Maeda, M. Yoshida, J. Kubota, S. Ikeda, M. Matsumura, and K. Domen, "Origin of Visible Light Absorption in GaN-Rich (Ga_{1-x}Zn_x)(N_{1-x}O_x) Photocatalysts." *J. Phys. Chem. C*, **111**, 18853, (2007).
- [12] W. Wei, Y. Dai, K. Yang, M. Guo, and B. Huang, "Origin of the Visible Light Absorption of GaN-Rich Ga_{1-x}Zn_xN_{1-x}O_x (x = 0.125) Solid Solution " *Journal of Physical Chemistry C*, **112**, 15915, (2008).
- [13] K. Maeda, K. Teramura, T. Takata, M. Hara, N. Saito, K. Toda, Y. Inoue, H. Kobayashi, and K. Domen, "Overall Water Splitting on (Ga_{1-x}Zn_x)(N_{1-x}O_x) Solid Solution Photocatalyst: Relationship between Physical Properties and Photocatalytic Activity." *J. Phys. Chem. B*, **109**, 20504, (2005).

- [14] K. Maeda, K. Teramura, N. Saito, Y. Inoue, and K. Domen, "Improvement of photocatalytic activity of $(\text{Ga}_{1-x}\text{Zn}_x)(\text{N}_{1-x}\text{O}_x)$ solid solution for overall water splitting by co-loading Cr and another transition metal." *J. Catal.*, **243**, 303, (2006).
- [15] K. Maeda, K. Teramura, D. Lu, T. Takata, N. Saito, Y. Inoue, and K. Domen, "Characterization of Rh-Cr Mixed-Oxide Nanoparticles Dispersed on $(\text{Ga}_{1-x}\text{Zn}_x)(\text{N}_{1-x}\text{O}_x)$ as a Cocatalyst for Visible-Light-Driven Overall Water Splitting." *J. Phys. Chem. B*, **110**, 13753, (2006).
- [16] K. Maeda, K. Teramura, D. Lu, N. Saito, Y. Inoue, and K. Domen, "Noble-metal/ Cr_2O_3 core/shell nanoparticles as a co-catalyst for photocatalytic overall water splitting." *Angew. Chem. , Int. Ed.*, **45**, 7806, (2006).
- [17] K. Maeda, K. Teramura, D. Lu, N. Saito, Y. Inoue, and K. Domen, "Roles of Rh/ Cr_2O_3 (Core/Shell) Nanoparticles Photodeposited on Visible-Light-Responsive $(\text{Ga}_{1-x}\text{Zn}_x)(\text{N}_{1-x}\text{O}_x)$ Solid Solutions in Photocatalytic Overall Water Splitting." *J. Phys. Chem. C*, **111**, 7554, (2007).
- [18] K. Maeda, K. Teramura, and K. Domen, "Effect of post-calcination on photocatalytic activity of $(\text{Ga}_{1-x}\text{Zn}_x)(\text{N}_{1-x}\text{O}_x)$ solid solution for overall water splitting under visible light." *J. Catal.*, **254**, 198, (2008).

- [19] S.V. Merzlikin, N.N. Tolkachev, L.E. Briand, T. Strunskus, C. Woll, I.E. Wachs, and W. Grunert, "Anomalous Surface Compositions of Stoichiometric Mixed Oxide Compounds " *Angew. Chem. Int. Ed Engl.*, **49**, 8037, (2010).
- [20] I.E. Wachs, K. Routray, "Catalysis Science of Bulk Mixed Oxides " *ACS Catalysis*, **2**, 1235, (2012).
- [21] P. Kubelka, F. Munk, *Z. Tech. Phys.*, **12**, 593, (1931).
- [22] X. Gao, I.E. Wachs, "Investigation of Surface Structures of Supported Vanadium Oxide Catalysts by UV-vis-NIR Diffuse Reflectance Spectroscopy." *J. Phys. Chem. B*, **104**, 1261, (2000).
- [23] W.N. Delgass (Ed.), *Spectroscopy in heterogeneous catalysis*, Academic Press:New York, 1979.
- [24] M. Anpo, P.V. Kamat (Eds.), *Environmentally Benign Photocatalysts: Applications of Titanium Oxide-based Materials*, Springer:New York, 2010.
- [25] B.J. Selby, T.I. Quickenden, and C.G. Freeman, "The Fitting of Luminescence Rises and Decays," *Kinetics and Catalysis*, 44, 5, (2003) .
- [26] T.I. Quickenden, T.A. Green, and D. Lennon, "Luminescence from UV-Irradiated Amorphous H₂O Ice " *J. Phys. Chem.*, **100**, 16801, (1996).

- [27] Y. Zhao, R.L. Frost, "Raman spectroscopy and characterisation of α -gallium oxyhydroxide and β -gallium oxide nanorods " *J. Raman Spectrosc.*, **39**, 1494, (2008).
- [28] R. Rao, A.M. Rao, B. Xu, J. Dong, S. Sharma, and M.K. Sunkara, "Blueshifted Raman scattering and its correlation with the [110] growth direction in gallium oxide nanowires " *J. Appl. Phys.*, **98**, 094312, (2005).
- [29] R. Cuscó, E. Alarcón-Lladó, J. Ibáñez, L. Artús, J. Jiménez, B. Wang, and M. Callahan, "Temperature dependence of Raman scattering in ZnO " *Physical Review B*, **75**, (2007).
- [30] W. Han, Z. Liu, and H. Yu, "Synthesis and optical properties of GaN/ZnO solid solution nanocrystals " *Appl. Phys. Lett.*, **96**, 183112, (2010).
- [31] V. Davydov, Y. Kitaev, I. Goncharuk, A. Smirnov, J. Graul, O. Semchinova, D. Uffmann, M. Smirnov, A. Mirgorodsky, and R. Evarestov, "Phonon dispersion and Raman scattering in hexagonal GaN and AlN " *Physical Review B*, **58**, 12899, (1998).
- [32] E.L. Lee, I.E. Wachs, "In Situ Spectroscopic Investigation of the Molecular and Electronic Structures of SiO₂ Supported Surface Metal Oxides." *J. Phys. Chem. C*, **111**, 14410, (2007).
- [33] D.S. Kim, J.M. Tatibouet, and I.E. Wachs, "Surface structure and reactivity of chromium trioxide/silica catalysts," *J. Catal.*, **136**, 209, (1992).

- [34] C.T. Williams, C.G. Takoudis, and M.J. Weaver, "Methanol Oxidation on Rhodium As Probed by Surface-Enhanced Raman and Mass Spectroscopies: Adsorbate Stability, Reactivity, and Catalytic Relevance " *The Journal of Physical Chemistry B*, **102**, 406, (1998).
- [35] T. Yanagida, Y. Sakata, and H. Imamura, "Photocatalytic decomposition of H₂O into H₂ and O₂ over Ga₂O₃ loaded with NiO." *Chem. Lett.*, **33**, 726, (2004).
- [36] H. BRONGERSMA, M. DRAXLER, M. DERIDDER, and P. BAUER, "Surface composition analysis by low-energy ion scattering " *Surface Science Reports*, **62**, 63, (2007).
- [37] G.D. Gilliland, "Photoluminescence spectroscopy of crystalline semiconductors" *Materials Science and Engineering: R: Reports*, **18**, 99, (1997).
- [38] J. Tang, J.R. Durrant, and D.R. Klug, "Mechanism of photocatalytic water splitting in TiO₂. Reaction of water with photoholes, importance of charge carrier dynamics, and evidence for four-hole chemistry " *J. Am. Chem. Soc.*, **130**, 13885, (2008).
- [39] C.A. Roberts, A.A. Puretsky, S.P. Phivilay, and I.E. Wachs, "Determination of a Structure-Photocatalytic Relationship for Water Splitting on Well-Defined TiO₂ Nanodomains," *In preparation for publication*, .

- [40] C. Hu, C. Tsai, and H. Teng, "Structure Characterization and Tuning of Perovskite-Like NaTaO_3 for Applications in Photoluminescence and Photocatalysis " *J Am Ceram Soc*, **92**, 460, (2009).
- [41] C. Hu, Y. Lee, and H. Teng, "Efficient water splitting over $\text{Na}_{1-x}\text{K}_x\text{TaO}_3$ photocatalysts with cubic perovskite structure" *J.Mater.Chem.*, (2011).

Excitation 400 nm			$y=A1*\exp(-t/t1)+A2*\exp(-t/t2)+y0$					
Catalyst	Eg (eV)	Peak Maximum (nm)	t1 (ps) fast	A1 fast	t2 (ps) slow	A2 slow	A1/(A1+A2)	A2/(A1+A2)
Ga₂O₃	4.7	713	4	131417	2404	1	0.99	9.40E-06
ZnO	3.2	637	789	29	6818	8	0.79	0.21
(Ga_{1-x}Zn_x)(N_{1-x}O_x)	2.6	657	941	179	7421	57	0.76	0.24
(Rh_{2-y}Cr_yO₃)/(Ga_{1-x}Zn_x)(N_{1-x}O_x).	2.5	725	1003	26	8002	15	0.64	0.36

Table 4.1: Eg values, peak emission wavelengths, and decay fit parameters of the catalysts at 400 nm excitation. The decay parameters displayed are those found in the PL spectra taken in the emission range of the peak value.

Element	
O 1s	15.9%
N 1s	60.2%
Ga 2p 3/2	22.2%
Zn 2p 3/2	1.7%

Table 4.2: XPS surface region atomic composition (~1-3nm) of $(\text{Ga}_{1-x}\text{Zn}_x)(\text{N}_{1-x}\text{O}_x)$.

Element	Fresh	Used
O 1s	23.5%	31.1%
N 1s	50.2%	48.6%
Ga 2p 3/2	10.9%	10.6%
Zn 2p 3/2	2.4%	1.9%
Cr 2p 3/2	5.2%	5.1%
Rh 3d	0.8%	1.1%
Cl 2p	3.5%	1.5%
Na 1s	3.4%	0.0%

Table 4.3: XPS surface region atomic composition (~1-3nm) of fresh and used (Rh₂-_yCr_yO₃) / (Ga_{1-x}Zn_x)(N_{1-x}O_x) mixed oxide photocatalysts.

Element	Fresh	Used
O 1s	31.7%	26.4%
N 1s	50.8%	54.1%
Ga 2p 3/2	10.9%	12.9%
Zn 2p 3/2	2.1%	1.7%
Cr 2p 3/2	3.4%	3.7%
Rh 3d	1.1%	1.2%
Cl 2p	0.0%	0.0%
Na 1s	0.0%	0.0%
K 2s	0.0%	0.0%

Table 4.4: HR-XPS surface region atomic composition (~1-3nm) of fresh and used (Rh/Cr₂O₃)/(Ga_{1-x}Zn_x)(N_{1-x}O_x) core/shell photocatalysts.

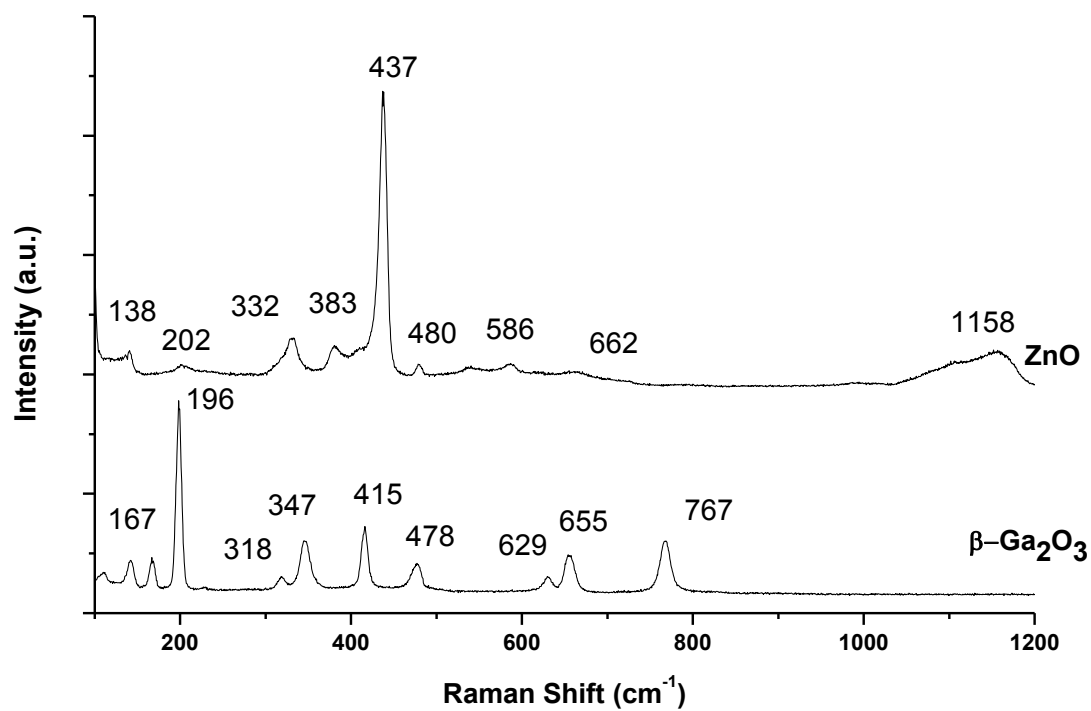


Figure 4.1: Raman Spectra of $\beta\text{-Ga}_2\text{O}_3$ and ZnO precursors (532 nm) under ambient conditions.

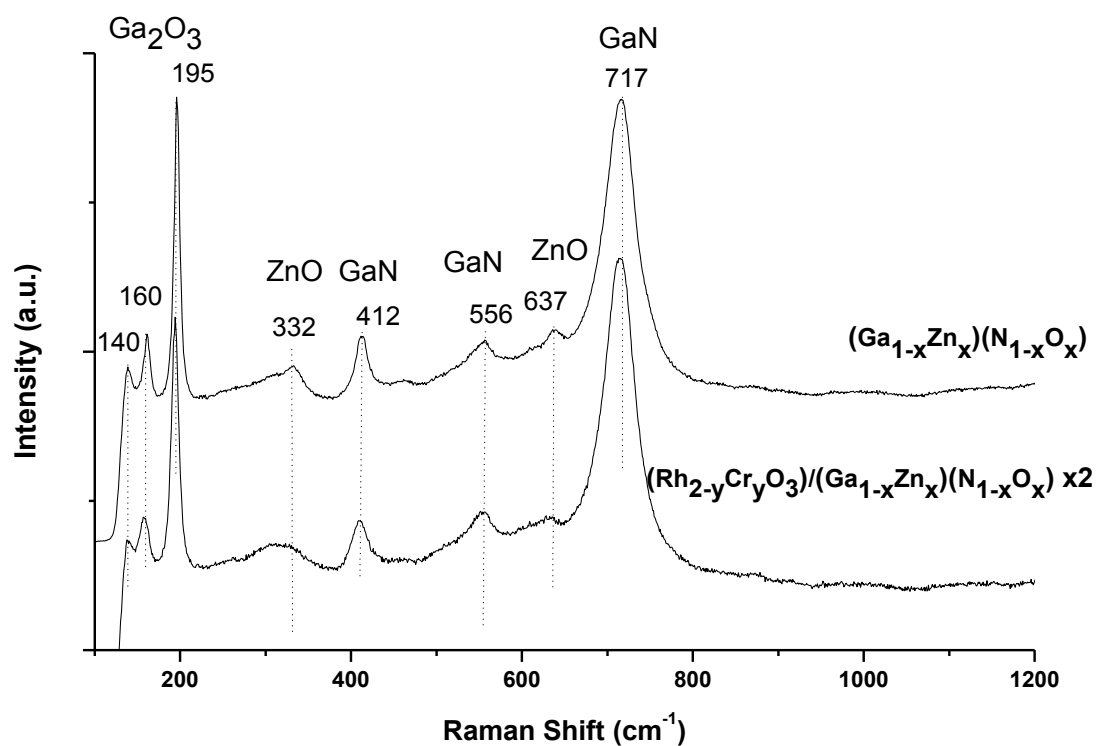


Figure 4.2: Raman Spectra of $(\text{Ga}_{1-x}\text{Zn}_x)(\text{N}_{1-x}\text{O}_x)$ and $(\text{Rh}_{2-y}\text{Cr}_y\text{O}_3)/(\text{Ga}_{1-x}\text{Zn}_x)(\text{N}_{1-x}\text{O}_x)$ (432 nm) under ambient conditions.

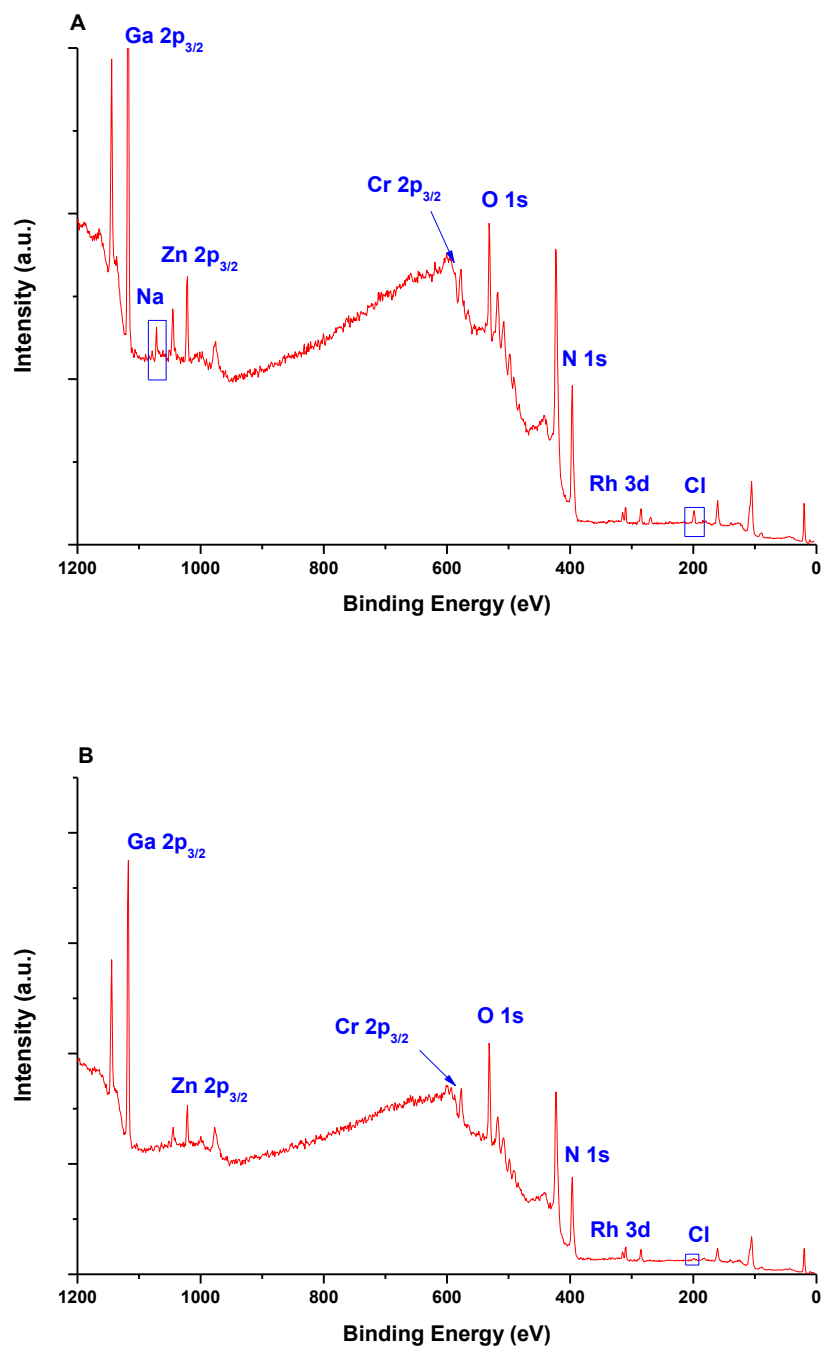


Figure 4.3: XPS Survey spectra of (a) fresh and (b) used $(\text{Rh}_{2-y}\text{Cr}_y\text{O}_3)/(\text{Ga}_{1-x}\text{Zn}_x)(\text{N}_{1-x}\text{O}_x)$ photocatalysts.

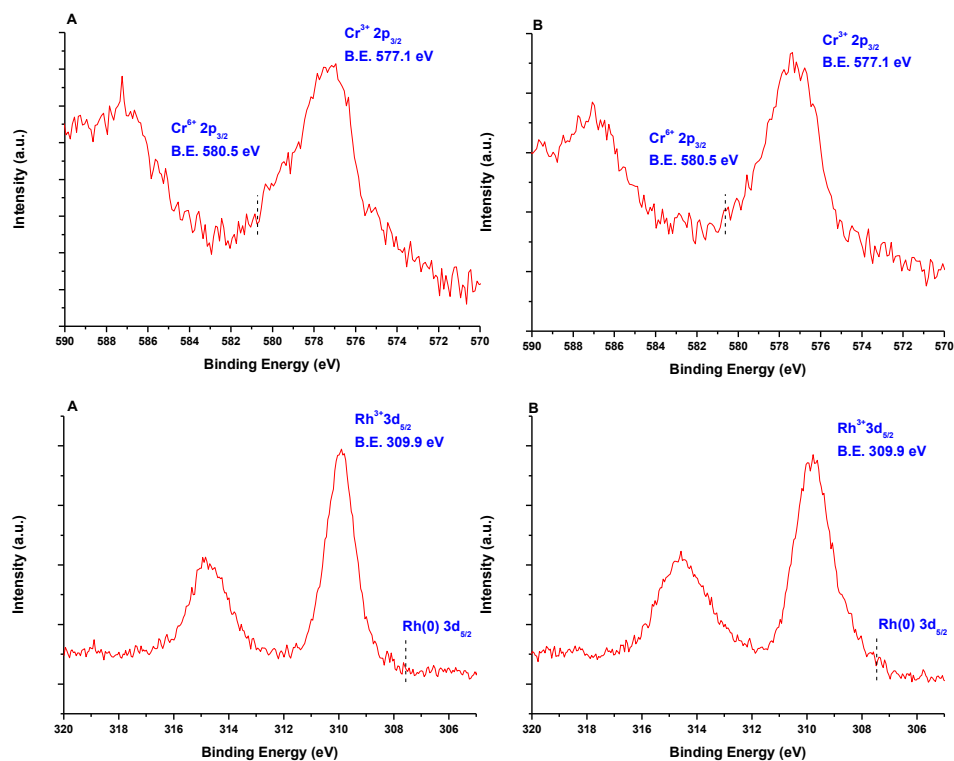


Figure 4.4: HR-XPS spectra of Cr 2p and Rh 3d regions of (a) fresh and (b) used supported $(\text{Rh}_{2-y}\text{Cr}_y\text{O}_3)/(\text{Ga}_{1-x}\text{Zn}_x)(\text{N}_{1-x}\text{O}_x)$ mixed oxide photocatalysts.

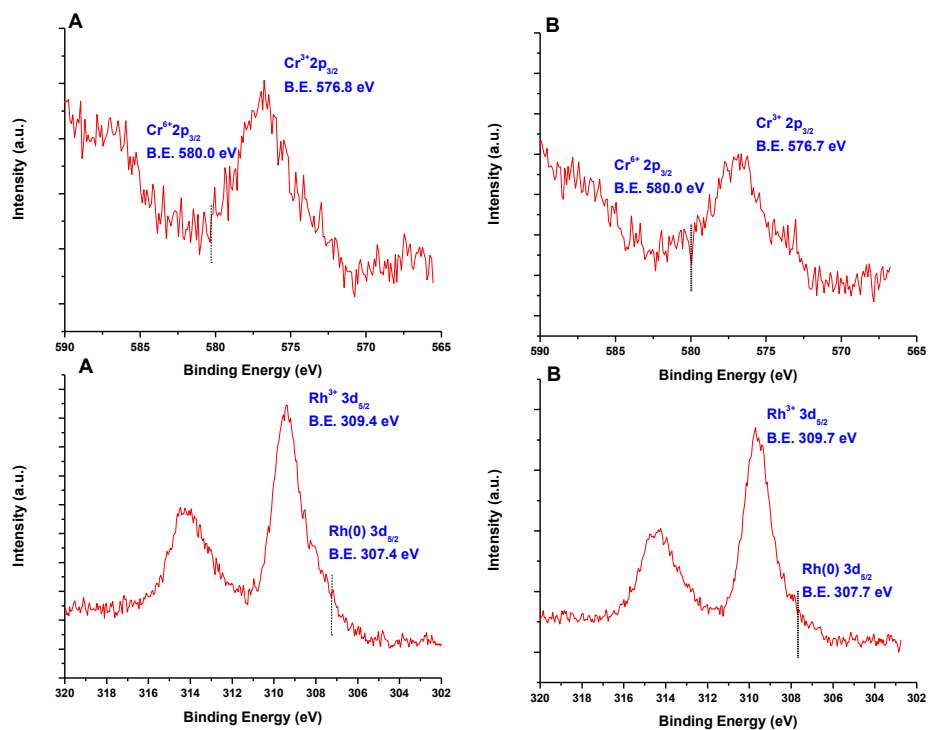


Figure 4.5: HR-XPS spectra of Cr 2p and Rh 3d regions of (a) fresh and (b) used (Rh/Cr₂O₃)/(Ga_{1-x}Zn_x)(N_{1-x}O_x) photocatalysts.

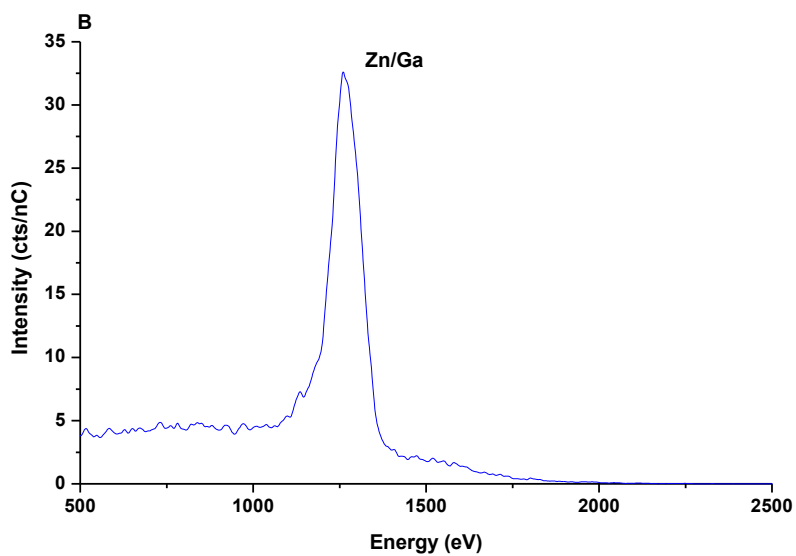
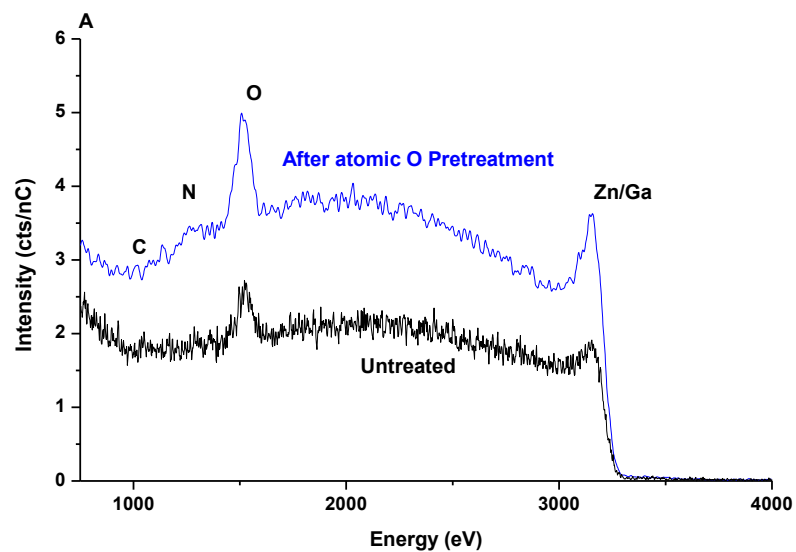


Figure 4.6: HS-LEIS spectra for $(\text{Ga}_{1-x}\text{Zn}_x)(\text{N}_{1-x}\text{O}_x)$ photocatalyst using (a) He^+ ion gas and (b) Ne^+ ion gas.

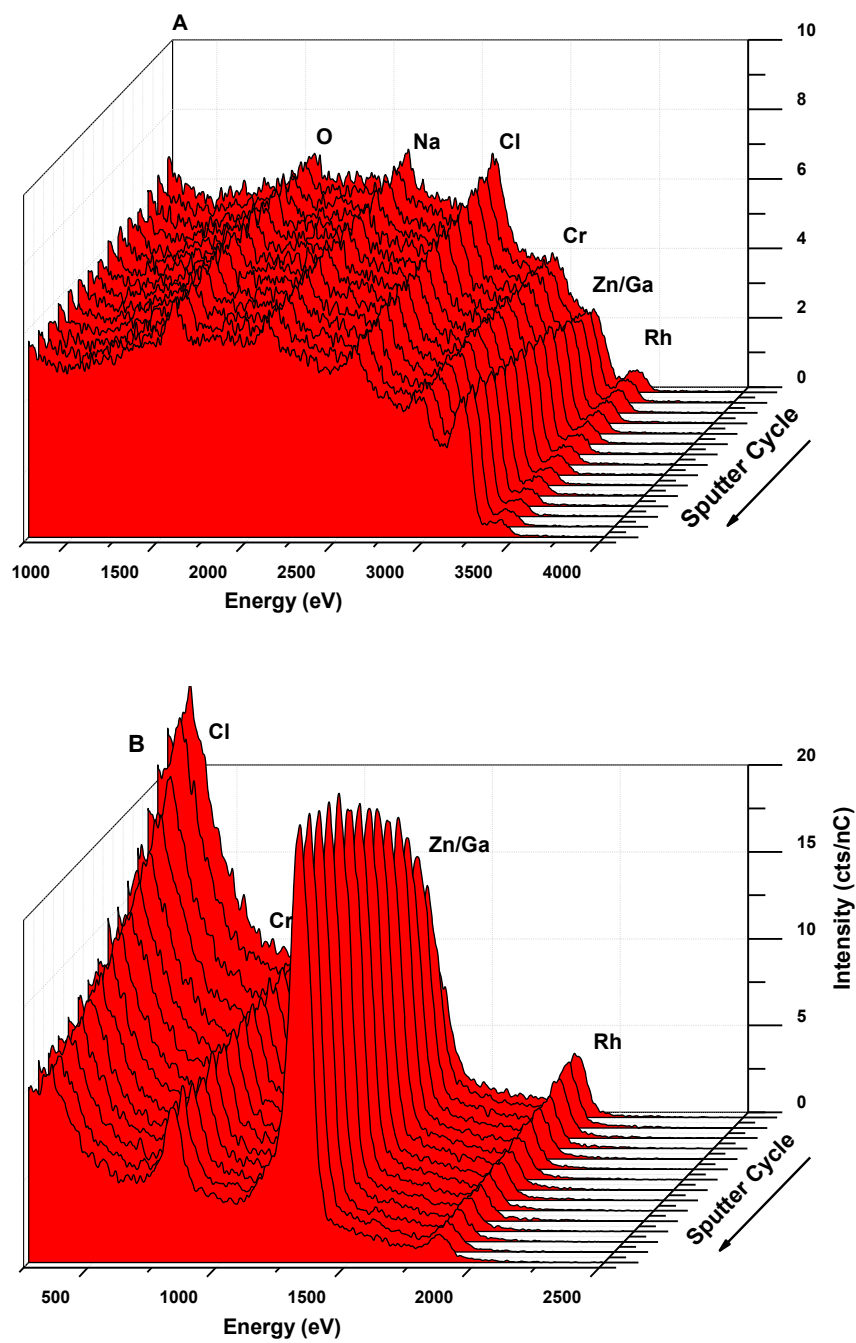


Figure 4.7: HS-LEIS Depth Profile for the fresh $(\text{Rh}_{2-y}\text{Cr}_y\text{O}_3)/(\text{Ga}_{1-x}\text{Zn}_x)(\text{N}_{1-x}\text{O}_x)$ photocatalyst using (a) He^+ ion gas and (b) Ne^+ ion gas.

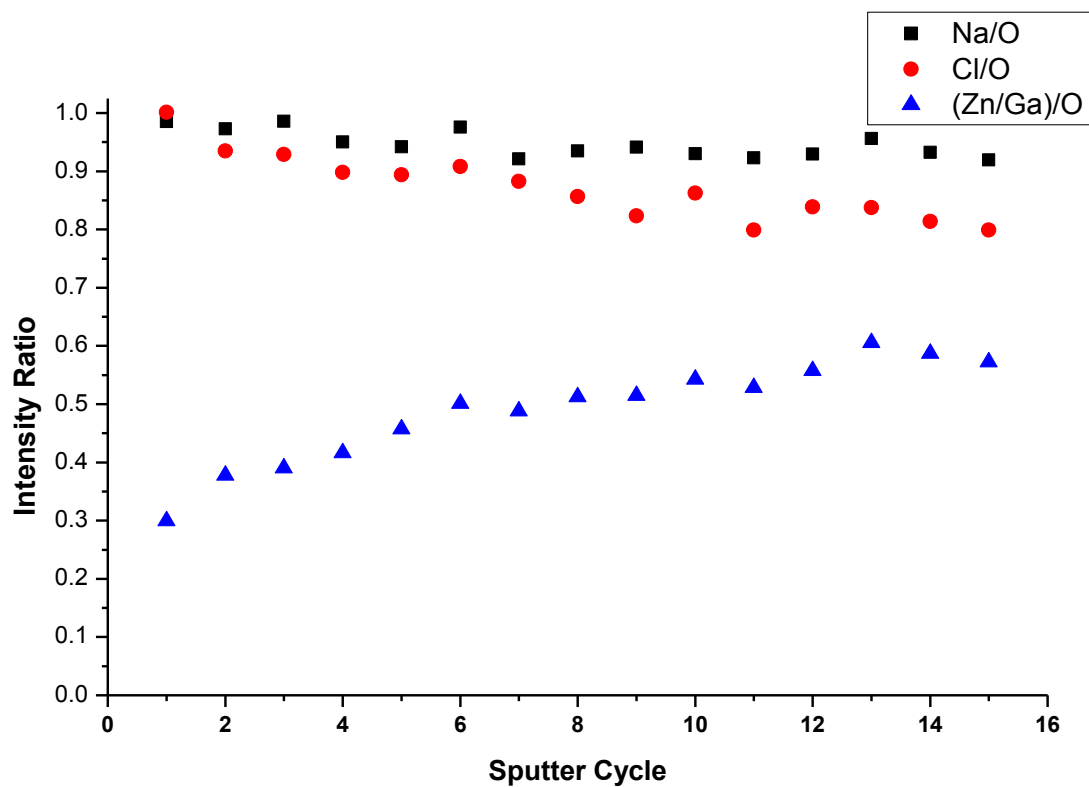


Figure 4.8: HS-LEIS depth profile intensity ratios of elements/oxygen for the fresh $(\text{Rh}_{2-y}\text{Cr}_y\text{O}_3) / (\text{Ga}_{1-x}\text{Zn}_x)(\text{N}_{1-x}\text{O}_x)$ photocatalyst using He^+ ion gas.

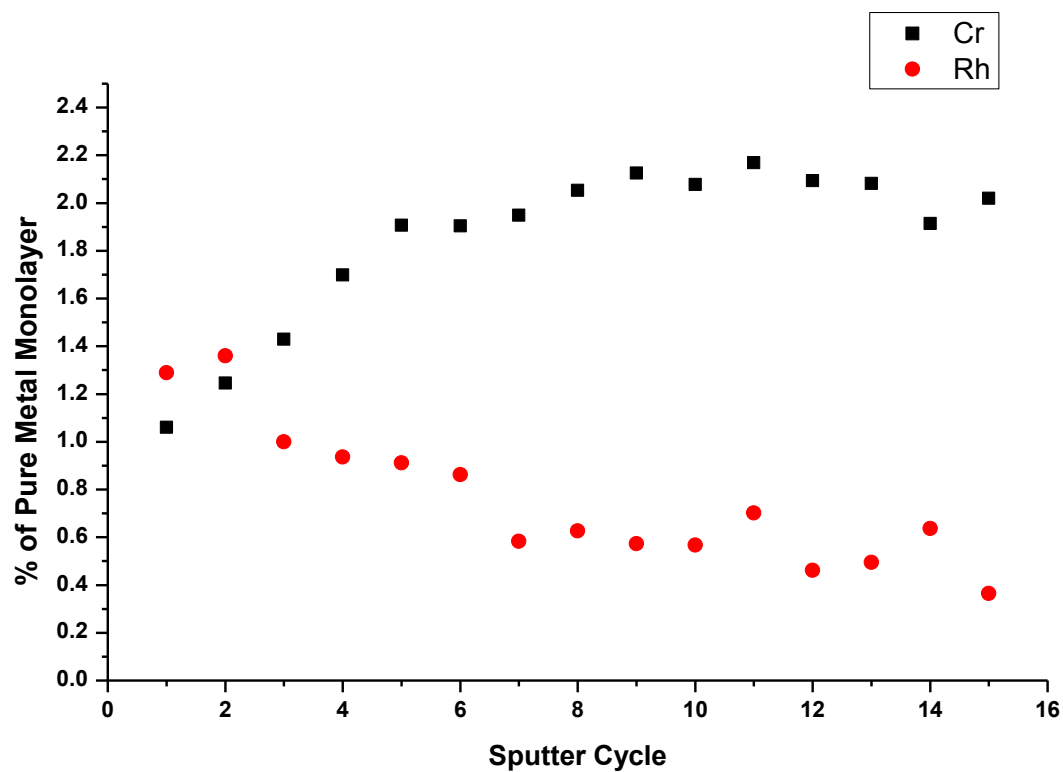


Figure 4.9: HS-LEIS Depth Profile of Cr and Rh for the fresh ($\text{Rh}_{2-y}\text{Cr}_y\text{O}_3$)

$/(\text{Ga}_{1-x}\text{Zn}_x)(\text{N}_{1-x}\text{O}_x)$ photocatalyst using Ne^+ ion gas.

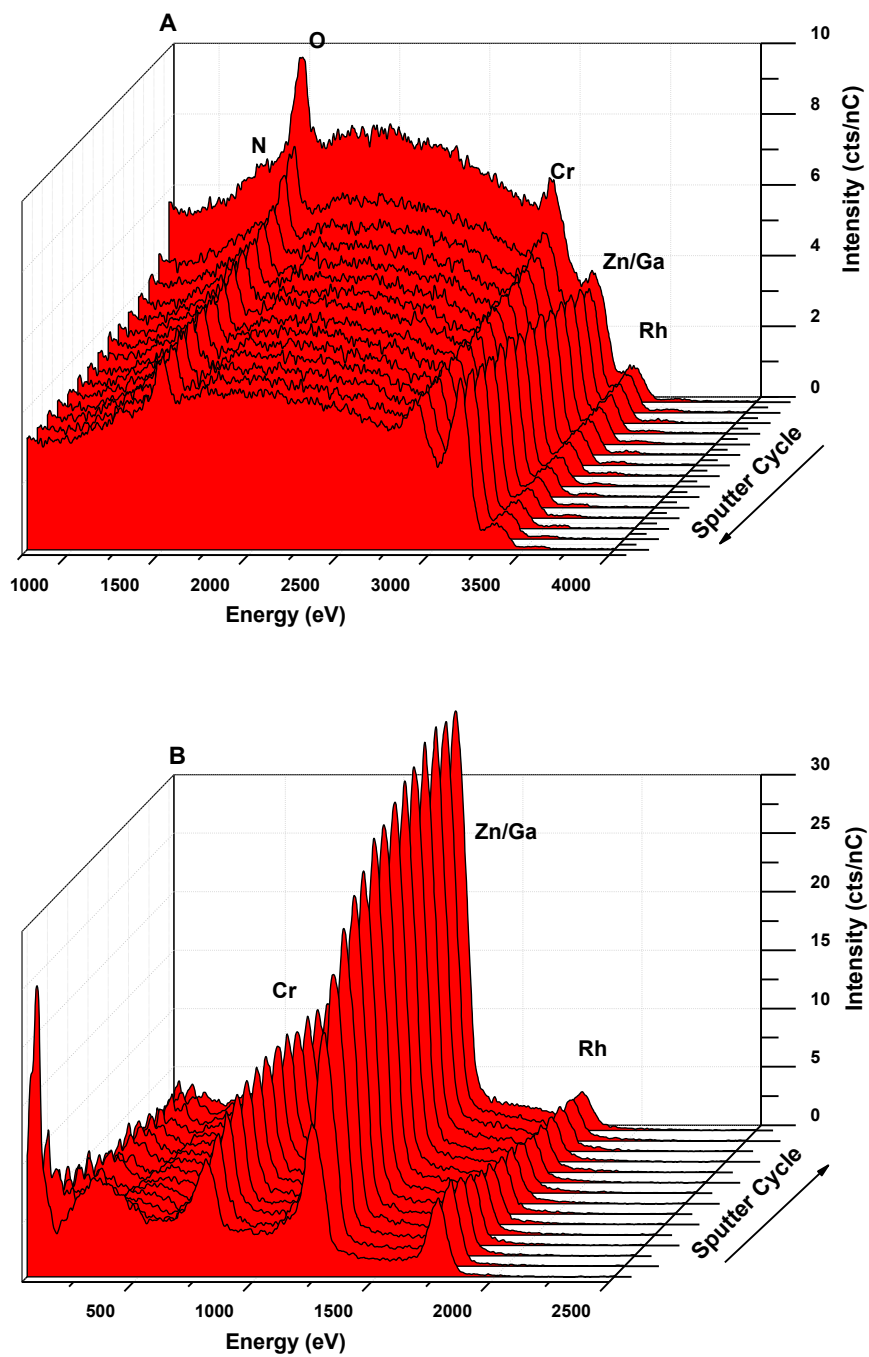


Figure 4.10: HS-LEIS Depth Profile for the used supported ($\text{Rh}_{2-y}\text{Cr}_y\text{O}_3$)

$/(\text{Ga}_{1-x}\text{Zn}_x)(\text{N}_{1-x}\text{O}_x)$ photocatalyst using (a) He^+ ion gas and (b) Ne^+ ion gas.

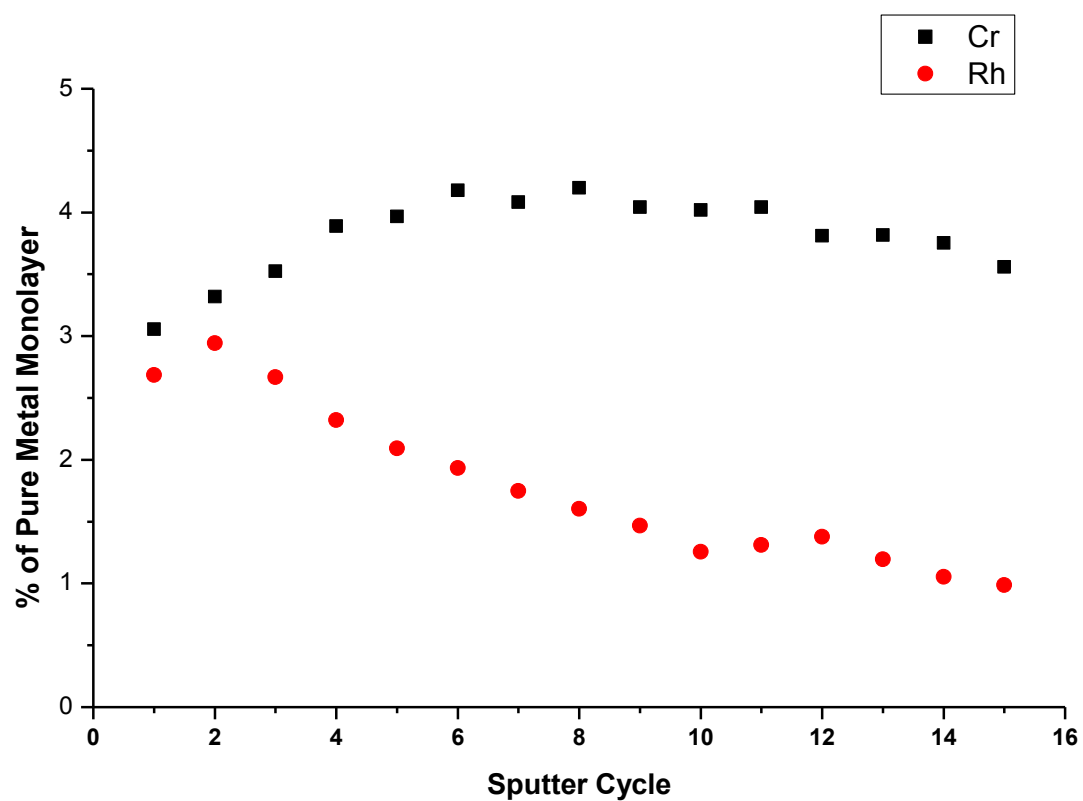


Figure 4.11: HS-LEIS Depth Profile of Cr and Rh for used supported ($\text{Rh}_{2-y}\text{Cr}_y\text{O}_3$)

$/(\text{Ga}_{1-x}\text{Zn}_x)(\text{N}_{1-x}\text{O}_x)$ photocatalyst using Ne^+ ion gas.

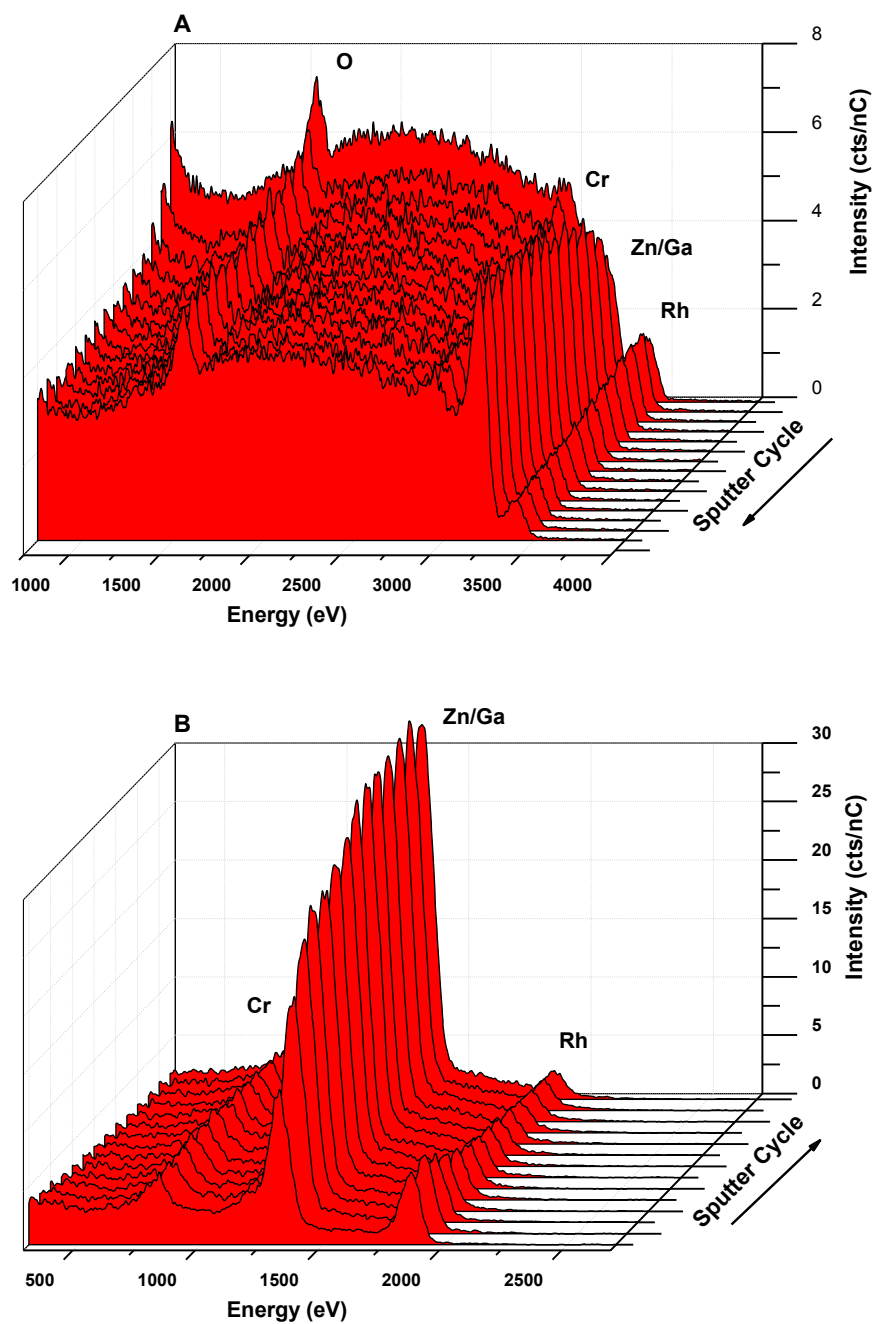


Figure 4.12: HS-LEIS Depth Profile for the fresh supported (Rh/Cr₂O₃)

/((Ga_{1-x}Zn_x)(N_{1-x}O_x) core/shell photocatalyst using (a) He⁺ ion gas and (b) Ne⁺ ion gas.

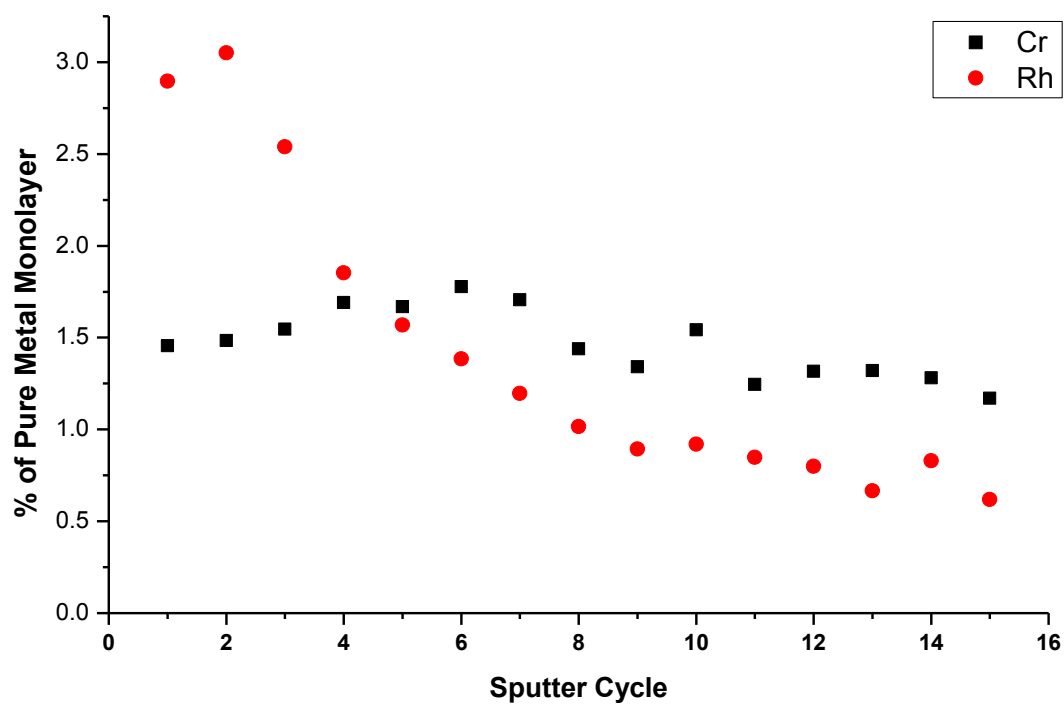


Figure 4.13: HS-LEIS Depth Profiles of Cr and Rh for the fresh supported (Rh/Cr₂O₃)/(Ga_{1-x}Zn_x)(N_{1-x}O_x) core/shell photocatalyst using Ne⁺ ion gas.

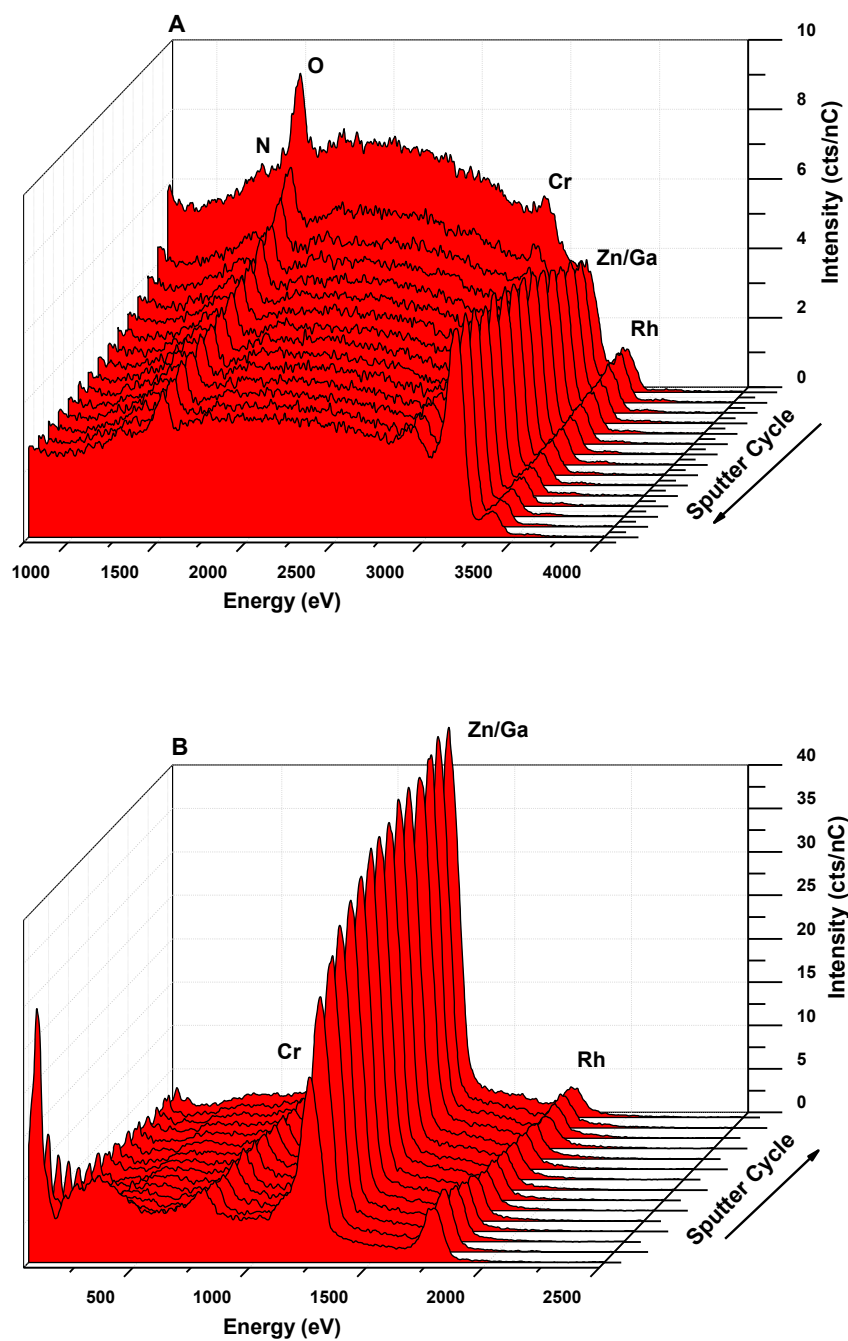


Figure 4.14: HS-LEIS Depth Profile for the used supported (Rh/Cr₂O₃)

/ (Ga_{1-x}Zn_x)(N_{1-x}O_x) core/shell photocatalyst using (a) He⁺ ion gas and (b) Ne⁺ ion gas.

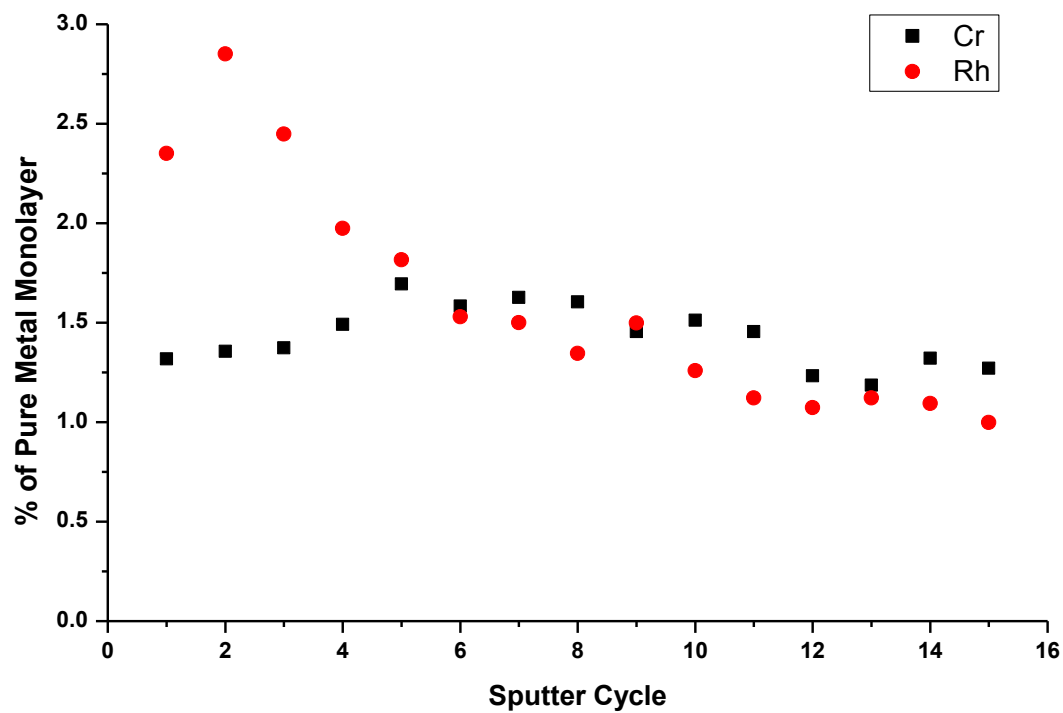


Figure 4.15: HS-LEIS Depth Profiles for Cr and Rh for the used supported (Rh/Cr₂O₃)/(Ga_{1-x}Zn_x)(N_{1-x}O_x) core/shell photocatalyst using Ne⁺ ion gas.

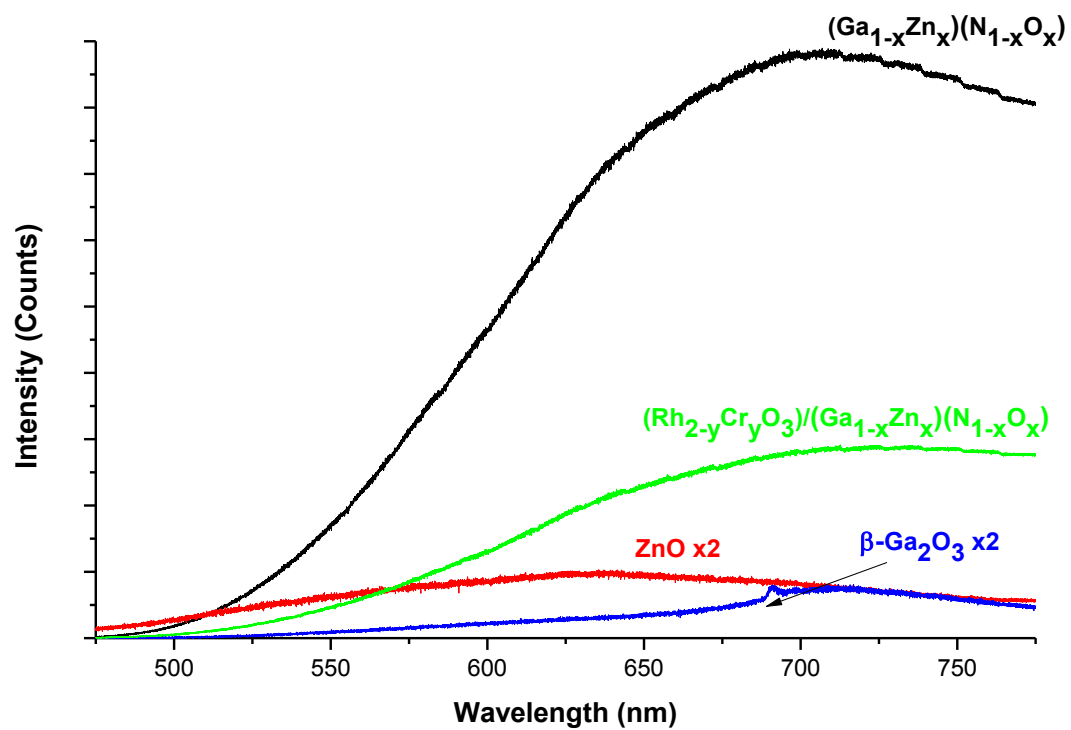


Figure 4.16: PL spectra of bulk $\beta\text{-Ga}_2\text{O}_3$, ZnO and oxynitride catalysts at 400 nm excitation.

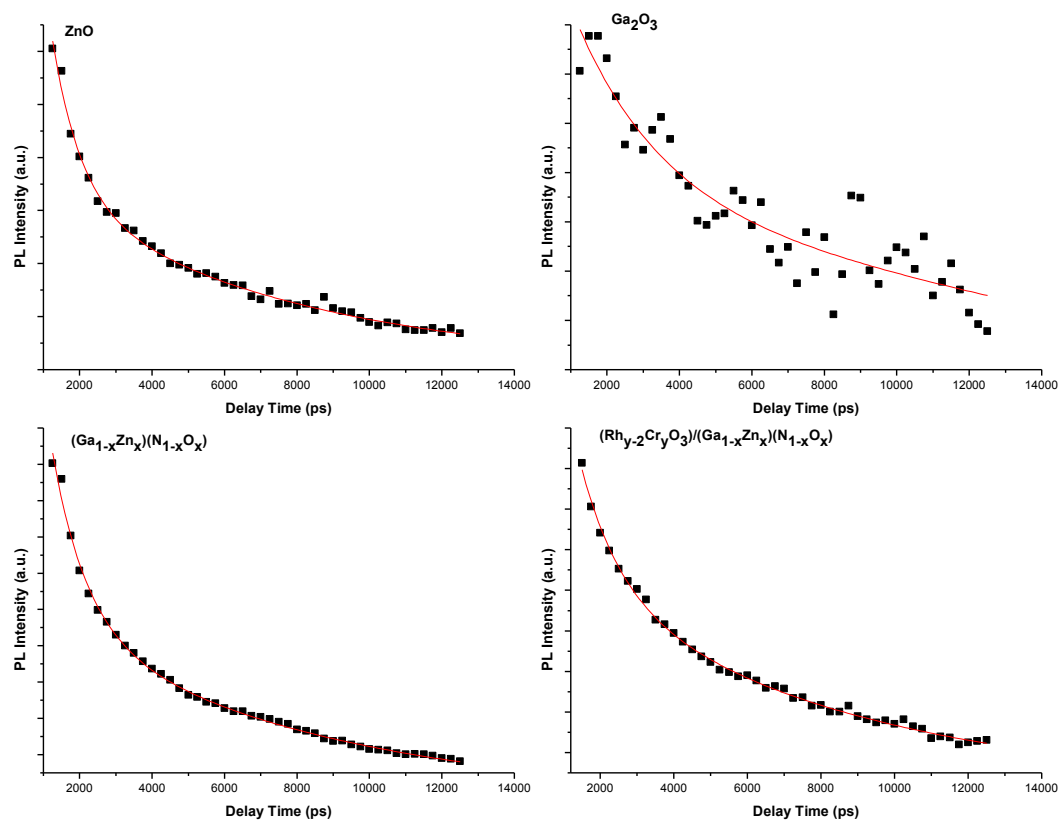


Figure 4.17: PL decay curves for the photocatalysts.

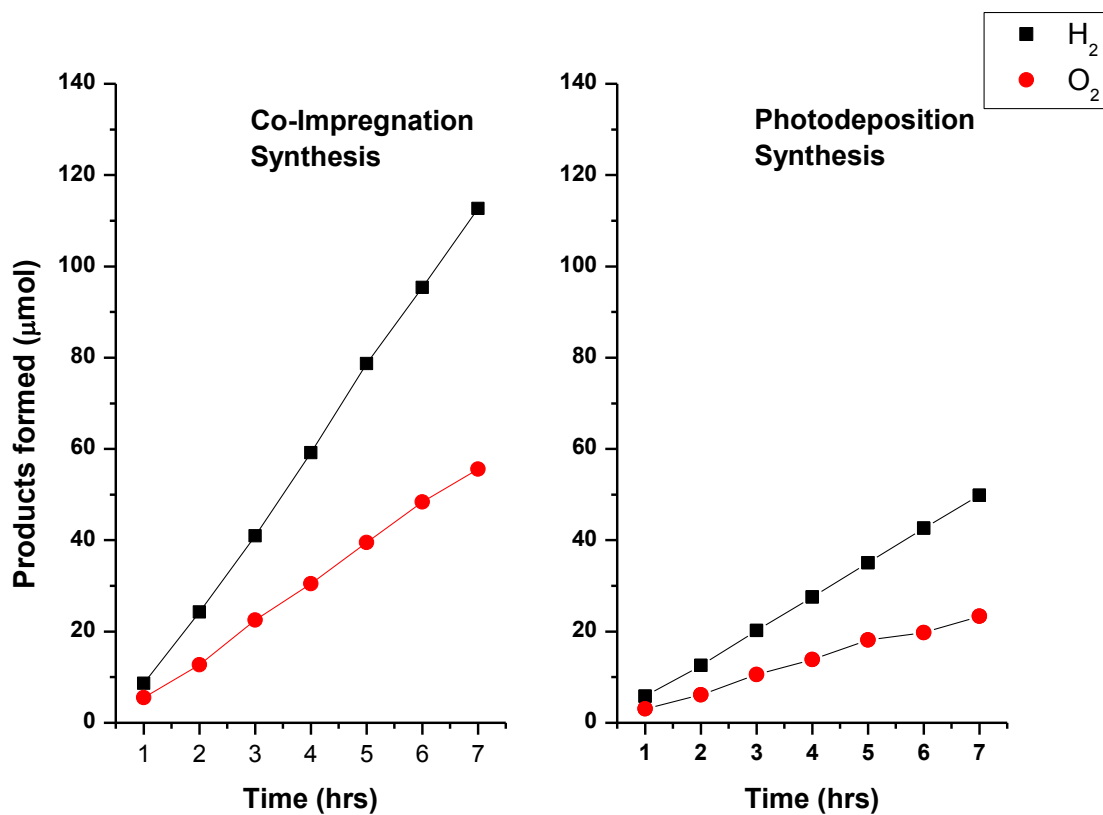


Figure 4.18: Comparison of Photocatalytic Water Splitting Activity ($\lambda > 400$ nm).

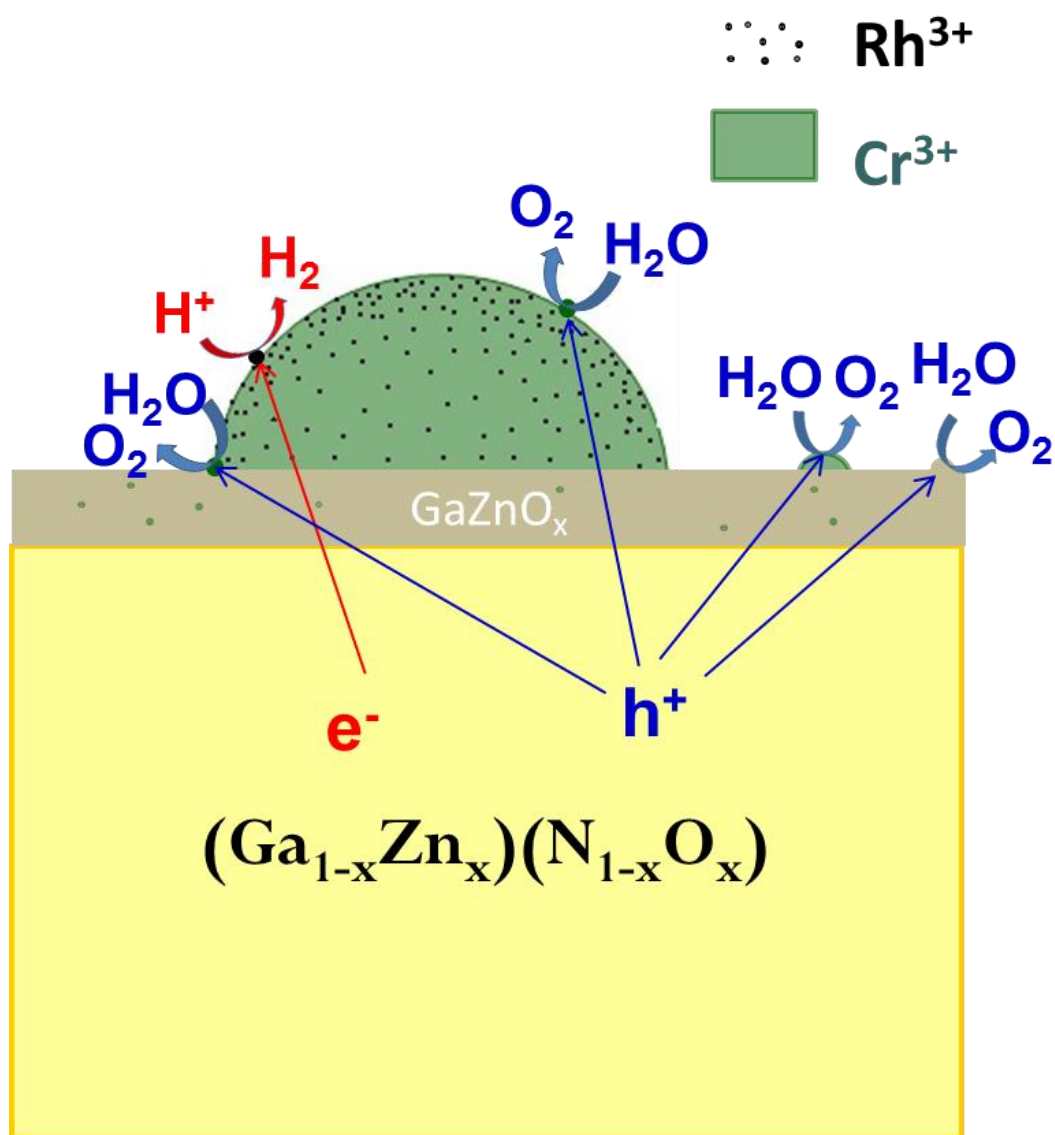


Figure 4.19: Schematic Model of Rh-Cr NPs for Co-Impregnation Synthesis Method.

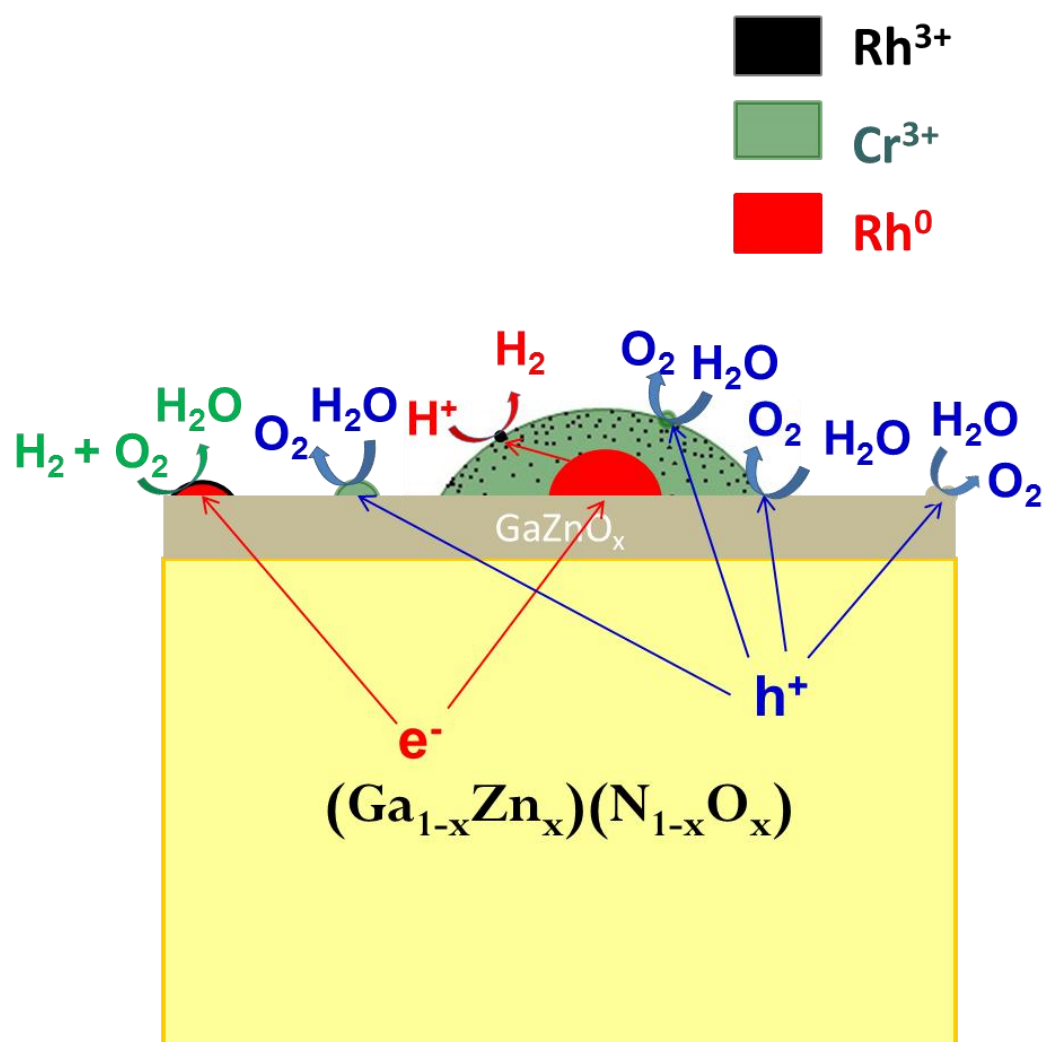


Figure 4.20: Schematic Model of Rh-Cr NPs for Photodeposition Synthesis Method.

CHAPTER 5

Investigating the Surface Nature of TaON Photocatalysts

Abstract

Bulk TaON and supported RuO₂/TaON photocatalysts used in Z-scheme photocatalytic water splitting were synthesized and characterized for their bulk and surface characteristics. The bulk properties of these photocatalysts were determined with Raman and UV-vis spectroscopy and show that the molecular and electronic structures, respectively, of the TaON support are not perturbed by the deposition of the RuO₂. For the first time, the surface properties of these photocatalysts were determined using High Resolution-XPS (HR-XPS) and High Sensitivity-Low Energy Ion Scattering (HS-LEIS) spectroscopy. The High Sensitivity-LEIS and HR-XPS surface measurements reveal that the outermost surface layers of TaON are present as a TaO_x thin film and that the deposited RuO₂ is present as dissolved Ru⁺⁴ cations in the tantalum oxide layers. These new structural insights of the surface region of supported RuO₂/TaON photocatalysts demonstrate that the photoactive catalytic sites for O₂ evolution are dissolved Ru⁺⁴ cations in the tantalum oxide thin film and not RuO₂ nanoparticles as previously proposed for this photocatalytic system.

5.1 Introduction

In recent years, the use of oxynitride materials for photocatalytic water splitting has garnered much attention due to their response to visible light irradiation [1]. Bulk oxynitride materials with d^0 electronic configuration: LaTiO_2N [2], CaNbO_2N [3], CaTaO_2N [4], SrTaO_2N [4], BaTaO_2N [4], TaON [5-7], $\text{Y}_2\text{Ta}_2\text{O}_5\text{N}_2$ [8] and $\text{TiN}_x\text{O}_y\text{F}_z$ [9] have been found to be able to evolve H_2 and O_2 in the presence of sacrificial reagents under visible light irradiation. Unlike bulk oxynitride materials with d^{10} electronic configuration, $(\text{Ga}_{1-x}\text{Zn}_x)(\text{N}_{1-x}\text{O}_x)$ [10-14] and $(\text{Zn}_{1+x}\text{Ge})(\text{N}_2\text{O}_x)$ [15], the bulk oxynitrides with d^0 electronic configuration cannot photocatalytically split pure water into H_2 and O_2 without sacrificial reagents. The main interest in studying the d^0 bulk oxynitrides is in their use as part of a two component Z-Scheme photocatalyst system [16]. Pt/TaON [17], $\text{Pt/CaTaO}_2\text{N}$ [18] and $\text{Pt/BaTaO}_2\text{N}$ [18] have been found to work as the H_2 evolution component with Pt/WO_3 as the O_2 evolution component using IO_3^-/I^- as the shuttle redox mediator in a Z-scheme system. The most active Z-scheme photocatalyst system ($\text{Pt/ZrO}_2/\text{TaON}$ with Pt/WO_3) has an optimized quantum yield of 6.3% at $\lambda > 420 \text{ nm}$ [19] that is higher than any single component photocatalyst system. There is still much research that can be done to improve the photoactivity for Z-scheme systems since this is a more recently developed technology. Thus, the study of advanced, novel d^0 bulk oxynitride materials is essential for the future design of more efficient Z-scheme systems.

One of the more recently discovered Z-scheme systems involves combining supported Pt/ZrO₂/TaON with supported RuO₂/TaON using IO³⁻/I⁻ as the shuttle redox couple [20, 21]. It was proposed that supported Pt/ZrO₂/TaON acts as the H₂ evolution photocatalysts while supported RuO₂/TaON acts as the O₂ evolution photocatalyst. Scanning electron microscopy (SEM) images of the supported RuO₂/TaON photocatalyst showed featureless RuO₂ nanoparticles on the TaON support and have been attributed to the greatly increased O₂ evolution for the system. From these observations it was hypothesized that the RuO₂ NPs are the catalytic active sites for O₂ evolution, although surface characterization was not performed to substantiate the proposed photocatalysis model.

The present study will focus on one half of a Z-scheme photocatalyst system to determine the surface nature of the supported RuO₂/TaON photocatalyst. Information about the surface region (~1-3nm) and outermost atomic layer (~0.3 nm) of the supported RuO₂/TaON photocatalyst system will be acquired by characterization with high-resolution X-ray photoelectron spectroscopy (HR-XPS) and high-sensitivity low energy ion scattering (HS-LEIS) spectroscopy, respectively. Complementary bulk molecular and electronic structural information about the TaON support phase and influence of the addition of the deposited RuO₂ NPs upon the TaON phase properties will be acquired with *in situ* optical spectroscopic characterization (Raman and UV-vis, respectively).

5.2 Experimental

5.2.1 Catalyst Synthesis

The bulk TaON phase was prepared by heating Ta₂O₅ powder (Rare Metallic, 99.9%) in a quartz reactor tube under flowing NH₃ (100 ml/min) and N₂ (1 ml/min) gases that were bubbled through water at 1123 K for 10 hrs [7]. The TaON was mixed in an evaporating dish with an aqueous solution of the (NH₄)₂RuCl₆ (Aldrich) precursor yielding 0.5 wt.% Ru [20]. This suspension was then placed over a water bath and continuously stirred with a glass rod until complete evaporation of water. The powder was then collected and calcined in air at 623 K for one hour.

5.2.2 Raman Spectroscopy

The Raman spectra for the photocatalyst were performed on a Lab Ram-HR Raman spectrometer (Horiba-Jobin Yvon) equipped with visible (532 nm) laser excitation and utilizing a confocal microscope (Olympus BX-30) for focusing the laser on the catalyst sample. The 532nm visible laser excitation was generated by Nd:YAG laser (10 mW) with the scattered photons directed into a single monochromator and focused onto a UV-sensitive liquid-N₂ cooled CCD detector (Horiba-Jobin Yvon CCD-3000V) having a spectral resolution of $\sim 2 \text{ cm}^{-1}$ for the given parameters. About 5-10 mg of the catalyst was placed into a high temperature *in situ* cell (Linkam TS-1500) with a quartz window and the spectrums were obtained under ambient conditions. The spectral acquisition time employed was 5 scans of 5 seconds/scan for each spectrum. System calibration was verified using a silica reference standard line at 520.7 cm^{-1} .

5.2.3 UV-vis NIR Diffuse Reflectance Spectroscopy (DRS)

Ultra Violet-visible-Near Infrared (UV-vis-NIR) diffuse reflectance spectroscopy was utilized to obtain the optical edge energy, E_g , values for the photocatalysts. Spectra were obtained using a Varian Cary 5E UV-vis spectrophotometer with a diffuse reflectance attachment (Harrick Praying Mantis Attachment, DRA-2). The finely ground powder catalyst samples (~20 mg) were loaded into an *in situ* cell (Harrick, HVC-DR2) and measured in the 200-800 nm spectral region with a magnesium oxide reflectance standard used as the baseline. A filter (Varian, 1.5ABS) was employed to minimize the background noise. A magnesium oxide white reflectance standard baseline was collected under ambient conditions. Determination of the Kubelka-Munk function, $F(R_\infty)$, was obtained from the UV-vis DRS absorbance and processed with Microsoft Excel software. The edge energy was determined by finding the intercept of the straight line in the low-energy rise of a plot of $[F(R_\infty)hv]^{1/n}$, where $n = 0.5$ for the direct allowed transition versus hv , where hv is the energy of the incident photon [22-24].

5.2.4 High Sensitivity-Low Energy Ion Scattering (HS-LEISS)

Spectroscopy

Analysis of the outermost surface layer of the photocatalysts was obtained on the Qtac¹⁰⁰ HS-LEIS Spectrometer (ION-TOF) equipped with a highly sensitive double toroidal analyzer, 3000 times higher sensitivity than conventional LEIS spectrometers, which allows for static depth profiling. The photocatalyst samples were first gently cleaned with atomic oxygen to remove surface hydrocarbon

contamination from the atmosphere prior to being transferred inside the analysis chamber. The HS-LEIS spectra were taken using 4000 eV $^4\text{He}^+$ with 10994 pA current as an ion source. For depth profiling, the surface was sputtered by Ar^+ gas at 1000 eV at a sputter yield of 1×10^{15} ions/cm².

5.2.5 High Resolution X-ray Photoelectron (HR-XPS) Spectroscopy

The HR-XPS spectra of the photocatalysts were obtained on a Scienta ESCA 300 spectrometer equipped with a 300 mm hemispherical electrostatic analyzer and a monochromatic Al K α X-ray source with energy of 1486.6 eV generated from a rotating anode. This allows for improved chemical selectivity by narrowing the spectral peaks of elements and greatly reducing the spectral background signal compared to conventional XPS spectrometers. Each spectrum was calibrated using a binding energy (BE) value of 285.0 eV for carbon in the C1s region. For depth profiling, the surface was sputtered ~ 30 Å for each cycle with Ar^+ gas at 1500 eV. The atomic concentration ratios were calculated by correcting the measured peak area ratios with relative sensitivity factors employed in the Casa XPS software version 2.3.15.

5.3 Results and Discussion

5.3.1 Bulk Characteristics of TaON Photocatalysts

5.3.1.1 Bulk Molecular Structure

The Raman spectra for Ta₂O₅ and the TaON photocatalysts are presented in Figure 1. The Raman spectrum of the bulk Ta₂O₅ starting material is characteristic of

the crystalline Ta₂O₅(L) phase [25]. The strongest Raman band in the spectrum of the Ta₂O₅(L) phase occurs at 100 cm⁻¹ and originates from the bulk lattice photon mode along with a second bulk lattice mode at 199 cm⁻¹. The Raman bands at 256 and 338 cm⁻¹ have been assigned to bridging Ta-O-Ta and TaO₆ bending modes, respectively. The bands at 489, 631, 708 and 848 cm⁻¹ are assigned to bridging Ta-O-Ta symmetric stretching, Ta-O symmetric stretching, bridging Ta-O-Ta antisymmetric stretching and higher order Ta-O symmetric stretching modes, respectively.

The detailed vibrational assignments for bulk TaON are currently not available in the literature. The Raman band at 259 cm⁻¹, however, can be assigned to the bridging Ta-O-Ta bending mode. The Raman bands at 125 and 175 cm⁻¹ can also be assigned to transverse acoustic and longitudinal acoustic phonon modes of TaN_x (0.94 ≤ x ≤ 1.37) [26]. The TaN_x also contains a broad optical phonon mode at 550 cm⁻¹ which was not able to be detected for the TaON. The vibrational spectrum of TaON demonstrates that the synthesized TaON phase is not just a physical mixture of the Ta₂O₅ and TaN phases and is an oxynitride material. The Raman spectrum of bulk TaON was not perturbed by the deposition of the Ru precursor and its oxidation to RuO₂. The vibrations of crystalline RuO₂ (characteristic Raman bands at 528, 646, and 716 cm⁻¹[27]) are not present in the Raman spectrum of the supported RuO₂/TaON photocatalyst against the strong bands from the TaON support phase. Thus, the bulk molecular structure of the TaON support phase is essentially unperturbed by the deposition of RuO₂ component.

5.3.1.2 Bulk Electronic Structure

The optical band gap (E_g) values of bulk Ta_2O_5 , TaON and 0.5% Ru/TaON were determined with UV-vis DRS are listed in Table 1. The obtained E_g values are in agreement with the values reported in the literature for these bulk phases [28]. The deposition of Ru and its oxidation to RuO_2 do not have a significant effect on the band gap of the bulk TaON photocatalyst.

5.3.2 Surface Atomic Composition of TaON photocatalysts

5.3.2.1 Outermost Surface Layer (~0.3 nm)

The outermost surface layer (~0.3 nm) and layers below the surface of the bulk TaON photocatalyst were analyzed with dynamic HS-LEIS employing a He^+ ion gas source after atomic O pretreatment and the results are presented in Figure 2. The HS-LEIS depth profile only reveals the presence of O and Ta on the surface with no signal for the N. Although it is difficult to obtain good elemental sensitivity for low mass elements like N without the use of $^3He^+$ as the gas ion source [29], the complete absence of N from the outermost surface layers suggests that this region became oxidized by exposure to the ambient environment. The HS-LEIS depth profile reveals that the signal for O is strongest on the outermost surface layer and decreases with depth while the signal for Ta increases with depth. The spectra for the TaON before atomic O treatment and after are compared in Figure 3. The treatment was found to increase signal intensity but did not affect the surface composition of the TaON photocatalyst. Thus, the outermost surface layers of bulk TaON do not contain any detectable N, are enriched in O and depleted in Ta.

The HS-LEIS depth profiles for the supported 0.5% RuO₂/TaON photocatalysts are presented in Figure 4. Surprisingly, no Ru is detected on the outermost surface layers and only the Ta and O signals are detected. The amount of RuO₂ in the photocatalyst is approximately an order of magnitude above the HS-LEIS detection limit (500 ppm). Furthermore, deposition of the Ru on the TaON support should lead to its greater concentration on the outermost surface. The lack of a HS-LEIS Ru signal suggests that most of the Ru species are diffusing into the bulk lattice of the TaON support during the calcination step at 623K.

5.3.2.2 Surface Region (~1-3 nm)

The XPS survey spectra of the surface region (~1-3 nm) for the TaON photocatalysts are presented in Figure 5 and the atomic compositions (calculated from the HR-XPS region) are reported in Table 2. The surface region of the bulk TaON photocatalyst consists only of Ta, O, and N with no contaminants detected (e.g., Cl from the (NH₄)₂RuCl₆ precursor). The O/N~2, O/Ta > 1 and N/Ta~0.6 atomic ratios demonstrate that the surface region is enriched in O and depleted in N, which is in agreement with the HS-LEIS findings. Unlike HS-LEIS, Ru species are able to be detected in the surface region with HR-XPS. The deposition of 0.5% RuO₂ on the TaON support did not greatly affect the surface region Ta, O and N atomic compositions. The composition of 0.5% RuO₂/TaON with depth profiling is also compared in Table 2 and indicates increased concentrations of Ta with decreased concentrations of O and N. The concentration of Ru was found to increase with the first 2 sputter cycles and the concentration was found to decrease afterwards. The

increasing surface concentrations of Ta and Ru and the decreasing surface concentrations on O and N are consistent with the HS-LEIS analysis revealing that O is surface enriched and that Ta and Ru are surface depleted and become more concentrated below the outermost surface layers. The initial increase in concentration of Ru with depth is consistent with the scenario that Ru has diffused into the subsurface lattice of the bulk TaON support. The decrease in concentration with further depth profiling indicates that it not uniformly distributed in the bulk phase and Ru is localized beneath the surface layer.

The HR-XPS spectra of the Ru 3d region for the unspattered and spattered supported RuO₂/TaON samples are compared in Figure 6. The Ru 3d_{5/2} binding energy indicates that Ru⁴⁺ cations predominate in the supported RuO₂/TaON photocatalysts. The HR-XPS spectra of the Ta 4f region for the unspattered and spattered supported RuO₂/TaON samples are also compared in Figure 7. The position of Ta 4f binding energies on the surface indicate that only Ta⁵⁺ oxidized species are present. However with depth profiling, the Ta⁵⁺ 4f bands decrease in intensity and a shoulder appears at a lower binding energy. This shift is indicative of reduced Ta and is consistent with the presence of greater Ta-N interaction beneath the surface layer [30]. The broad nature of the Ta 4f doublet bands suggests that both Ta-O and Ta-N interactions are present in the bulk.

5.3.2.3 Surface Nature of TaON Photocatalysts

The HS-LEIS analysis showed that Ta and O were the only elements present on the outermost surface layer. The position of the HR-XPS Ta 4f binding energies

show that Ta is in an oxidized state on the surface layer and there exist a TaO_x outer layer for the photocatalyst. Depth profiling revealed that the chemical state of the Ta changes from exclusively TaO_x to a combination of TaO_x and TaN_x which confirms that TaO_x is surface enriched and that TaON is the bulk state. The deposited Ru was proposed to be concentrated on the surface, however the lack of a Ru signal in the HS-LEIS spectra shows that is not the case. HR-XPS confirmed that Ru is not surface enriched and it is mostly concentrated below the surface region. The schematic for the surface of the photocatalyst is shown in Figure 8.

5.3.3 Structure-Photoactivity Relationships

The new insights indicate the supported RuO₂/TaON photocatalyst system is a much more complex material than was previously proposed with RuO₂ NPs deposited on the external surface of the TaON support with the RuO₂ NPs the catalytic photoactive sites proposed to be responsible for O₂ evolution [20]. Rather than RuO₂ NPs being the catalytic photoactive sites for O₂ evolution, it appears that the Ru⁺⁴ sites dissolved in the TaON support surface region, which is enriched with O and depleted in N, are responsible for O₂ evolution. Higher RuO₂ loadings on the TaON support were found to significantly decrease the photoactivity and may indeed be related to formation of RuO₂ NPs that are not photoactive. The function of the bulk TaON support is to supply visible light excited photoelectrons that can be utilized by the Ru⁺⁴ catalytic active sites, in the oxygen rich oxynitride TaON surface region, to evolve O₂ during photodecomposition of H₂O. The new surface insights are changing

our models about how complex semiconductor photocatalysts function and will guide the development of advanced photocatalytic materials.

5.4 Conclusions

The bulk molecular and electronic structures of the TaON phase are not affected by the deposition of RuO₂ on the TaON support. For the first time, the natures of the surface region of TaON and supported RuO₂/TaON photocatalysts have been determined. The outermost surface layers primarily consist of TaO_x phase and is depleted in N. The RuO₂ component is not present as NPs decorating the TaON support as previously concluded, but the Ru⁴⁺ cations are dissolved in the TaO_x outer layers and absent from the outermost surface layer. The new surface insights are changing our models about how complex semiconductor photocatalysts function and will guide the development of advanced photocatalytic materials.

Acknowledgements

This research was financially supported by the Department of Energy grant: DOE-FG02-93ER14350. Thanks to A. Xiong, Dr. J. Kubota and Professor K. Domen at the University of Tokyo for their assistance with the synthesis of the TaON photocatalysts. The assistance of Dr. A. Miller and R. Pafchek at Lehigh University in obtaining and interpreting the HR-XPS and HS-LEIS data is also gratefully acknowledged

References

- [1] K. Maeda, K. Domen, "New Non-Oxide Photocatalysts Designed for Overall Water Splitting under Visible Light." *J. Phys. Chem. C*, **111**, 7851, (2007).
- [2] A. Kasahara, K. Nukumizu, G. Hitoki, T. Takata, J.N. Kondo, M. Hara, H. Kobayashi, and K. Domen, "Photoreactions on LaTiO₂N under Visible Light Irradiation." *J. Phys. Chem. A*, **106**, 6750, (2002).
- [3] G. Hitoki, T. Takata, U.N. Kondo, M. Hara, H. Kobayashi, and K. Domen, "(Oxy)nitrides as new photocatalysts for water splitting under visible light irradiation." *Electrochemistry (Tokyo, Jpn.)*, **70**, 463, (2002).
- [4] D. Yamasita, T. Takata, M. Hara, J.N. Kondo, and K. Domen, "Recent progress of visible-light-driven heterogeneous photocatalysts for overall water splitting." *Solid State Ionics*, **172**, 591, (2004).
- [5] G. Hitoki, T. Takata, J.N. Kondo, M. Hara, H. Kobayashi, and K. Domen, "An oxynitride, TaON, as an efficient water oxidation photocatalyst under visible light irradiation (1 ? 500 nm)." *Chem. Commun. (Cambridge, U. K.)*, 1698, (2002).
- [6] M. Hara, J. Nunoshige, T. Takata, J.N. Kondo, and K. Domen, "Unusual enhancement of H₂ evolution by Ru on TaON photocatalyst under visible light irradiation." *Chem. Commun. (Cambridge, U. K.)*, 3000, (2003).

- [7] M. Hara, T. Takata, J.N. Kondo, and K. Domen, "Photocatalytic reduction of water by TaON under visible light irradiation." *Catal. Today*, **90**, 313, (2004).
- [8] M. Liu, W. You, Z. Lei, G. Zhou, J. Yang, G. Wu, G. Ma, G. Luan, T. Takata, M. Hara, K. Domen, and C. Li, "Water reduction and oxidation on Pt-Ru/Y₂Ta₂O₅N₂ catalyst under visible light irradiation." *Chem. Commun. (Cambridge, U. K.)*, 2192, (2004).
- [9] K. Maeda, Y. Shimodaira, B. Lee, K. Teramura, D. Lu, H. Kobayashi, and K. Domen, "Studies on TiN_xO_yF_z as a Visible-Light-Responsive Photocatalyst." *J. Phys. Chem. C*, **111**, 18264, (2007).
- [10] K. Maeda, K. Teramura, D. Lu, N. Saito, Y. Inoue, and K. Domen, "Roles of Rh/Cr₂O₃ (Core/Shell) Nanoparticles Photodeposited on Visible-Light-Responsive (Ga_{1-x}Zn_x)(N_{1-x}O_x) Solid Solutions in Photocatalytic Overall Water Splitting." *J. Phys. Chem. C*, **111**, 7554, (2007).
- [11] K. Maeda, K. Teramura, D. Lu, T. Takata, N. Saito, Y. Inoue, and K. Domen, "Characterization of Rh-Cr Mixed-Oxide Nanoparticles Dispersed on (Ga_{1-x}Zn_x)(N_{1-x}O_x) as a Cocatalyst for Visible-Light-Driven Overall Water Splitting." *J. Phys. Chem. B*, **110**, 13753, (2006).

- [12] K. Maeda, K. Teramura, D. Lu, N. Saito, Y. Inoue, and K. Domen, "Noble-metal/Cr₂O₃ core/shell nanoparticles as a co-catalyst for photocatalytic overall water splitting." *Angew. Chem., Int. Ed.*, **45**, 7806, (2006).
- [13] K. Maeda, K. Teramura, and K. Domen, "Effect of post-calcination on photocatalytic activity of (Ga_{1-x}Zn_x)(N_{1-x}O_x) solid solution for overall water splitting under visible light." *J. Catal.*, **254**, 198, (2008).
- [14] K. Maeda, K. Teramura, N. Saito, Y. Inoue, and K. Domen, "Improvement of photocatalytic activity of (Ga_{1-x}Zn_x)(N_{1-x}O_x) solid solution for overall water splitting by co-loading Cr and another transition metal." *J. Catal.*, **243**, 303, (2006).
- [15] Y. Lee, H. Terashima, Y. Shimodaira, K. Teramura, M. Hara, H. Kobayashi, K. Domen, and M. Yashima, "Zinc germanium oxynitride as a photocatalyst for overall water splitting under visible light." *J. Phys. Chem. C*, **111**, 1042, (2007).
- [16] R. Abe, "Development of a New System for Photocatalytic Water Splitting into H₂ and O₂ under Visible Light Irradiation," *Bull. Chem. Soc. Jpn.*, **84**, 1000, (2011).
- [17] R. Abe, T. Takata, H. Sugihara, and K. Domen, "Photocatalytic overall water splitting under visible light by TaON and WO₃ with an IO₃⁻/I⁻ shuttle redox mediator." *Chem. Commun. (Cambridge, U. K.)*, 3829, (2005).

- [18] M. Higashi, R. Abe, K. Teramura, T. Takata, B. Ohtani, and K. Domen, "Two step water splitting into H₂ and O₂ under visible light by ATaO₂N (A = Ca, Sr, Ba) and WO₃ with IO³⁻/I⁻ shuttle redox mediator." *Chem. Phys. Lett.*, **452**, 120, (2008).
- [19] K. Maeda, M. Higashi, D. Lu, R. Abe, and K. Domen, "Efficient Nonsacrificial Water Splitting through Two-Step Photoexcitation by Visible Light using a Modified Oxynitride as a Hydrogen Evolution Photocatalyst." *Zhonghua Jianyan Yixue Zazhi*, **32**, 5858, (2009).
- [20] K. Maeda, R. Abe, and K. Domen, "Role and Function of Ruthenium Species as Promoters with TaON-Based Photocatalysts for Oxygen Evolution in Two-Step Water Splitting under Visible Light" *The Journal of Physical Chemistry C*, **115**, 3057, (2011).
- [21] M. Higashi, R. Abe, A. Ishikawa, T. Takata, B. Ohtani, and K. Domen, "Z-scheme overall water splitting on modified-TaON photocatalysts under visible light ($\lambda < 500$ nm)." *Chem. Lett.*, **37**, 138, (2008).
- [22] P. Kubelka, F. Munk, *Z. Tech. Phys.*, **12**, 593, (1931).
- [23] X. Gao, I.E. Wachs, "Investigation of Surface Structures of Supported Vanadium Oxide Catalysts by UV-vis-NIR Diffuse Reflectance Spectroscopy." *J. Phys. Chem. B*, **104**, 1261, (2000).

- [24] W.N. Delgass (Ed.), *Spectroscopy in heterogeneous catalysis*, Academic Press:New York, 1979.
- [25] Y. Chen, J.L.G. Fierro, T. Tanaka, and I.E. Wachs, "Supported Tantalum Oxide Catalysts: Synthesis, Physical Characterization, and Methanol Oxidation Chemical Probe Reaction," *The Journal of Physical Chemistry B*, **107**, 5243, (2003).
- [26] M. Stoehr, C.-. Shin, I. Petrov, and J.E. Greene, "Raman scattering from epitaxial TaN[sub x] (0.94=x=1.37) layers grown on MgO(001) " *J. Appl. Phys.*, **101**, 123509, (2007).
- [27] A.V. Korotcov, Y. Huang, K. Tiong, and D. Tsai, "Raman scattering characterization of well-aligned RuO₂ and IrO₂ nanocrystals " *J. Raman Spectrosc.*, **38**, 737, (2007).
- [28] T. Takata, G. Hitoki, J.N. Kondo, M. Hara, H. Kobayashi, and K. Domen, "Visible-light-driven photocatalytic behavior of tantalum-oxynitride and nitride." *Res. Chem. Intermed.*, **33**, 13, (2007).
- [29] H. BRONGERSMA, M. DRAXLER, M. DERIDDER, and P. BAUER, "Surface composition analysis by low-energy ion scattering" *Surface Science Reports*, **62**, 63, (2007).

[30] W. Chun, A. Ishikawa, H. Fujisawa, T. Takata, J.N. Kondo, M. Hara, M. Kawai, Y. Matsumoto, and K. Domen, "Conduction and Valence Band Positions of Ta₂O₅, TaON, and Ta₃N₅ by UPS and Electrochemical Methods " *The Journal of Physical Chemistry B*, **107**, 1798, (2003).

Catalyst	E _g (eV)
Ta ₂ O ₅	4.1
TaON	2.8
0.5%Ru/TaON	2.8

Table 5.1: Uv-vis DRS Edge Energy Values for Tantalum-based Photocatalysts.

	TaO N	Ru/TaON Surface	Ru/TaON 30 Å	Ru/TaON 60 Å	Ru/TaON 90 Å	Ru/TaON 120 Å
Element	Atom ic %	Atomic %	Atomic %	Atomic %	Atomic %	Atomic %
Ta 4f	37.26	35.62	43.77	45.14	45.93	46.92
O 1s	40.40	41.89	35.57	35.68	36.12	36.36
N 1s	22.33	21.65	19.73	18.18	17.07	16.07
Ru 3d 5/2	0.00	0.84	0.93	1.00	0.88	0.65

Table 5.2: HR-XPS Surface Region Atomic Composition of TaON Photocatalysts.

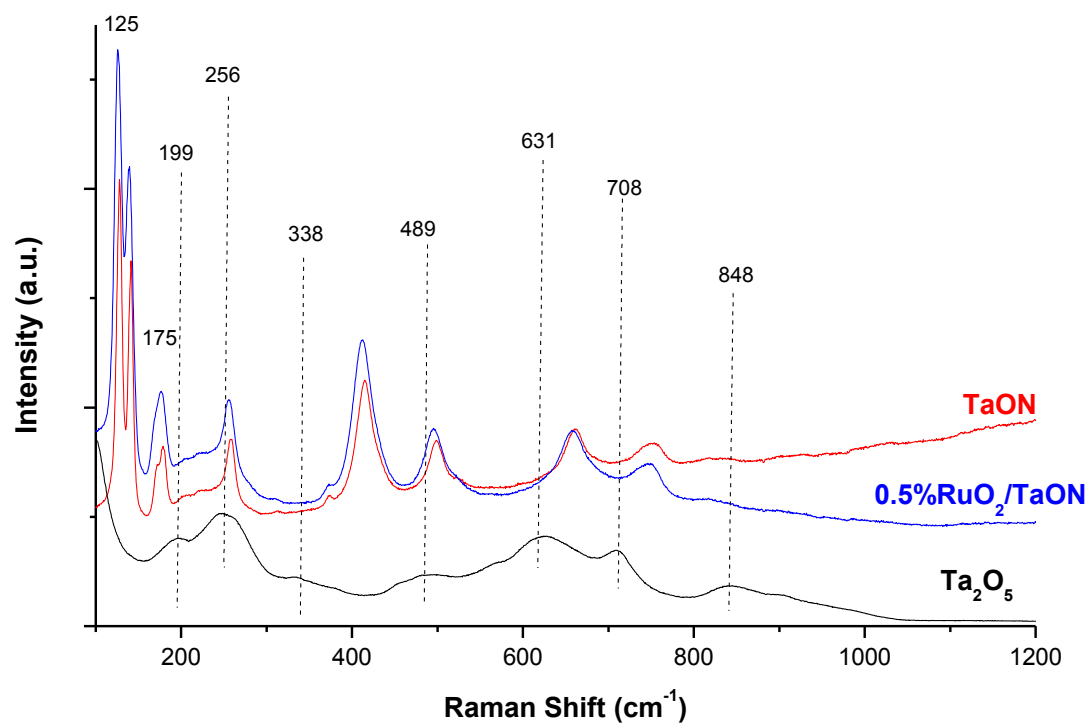


Figure 5.1: Raman Spectra of Tantalum-based Photocatalysts (532 nm).

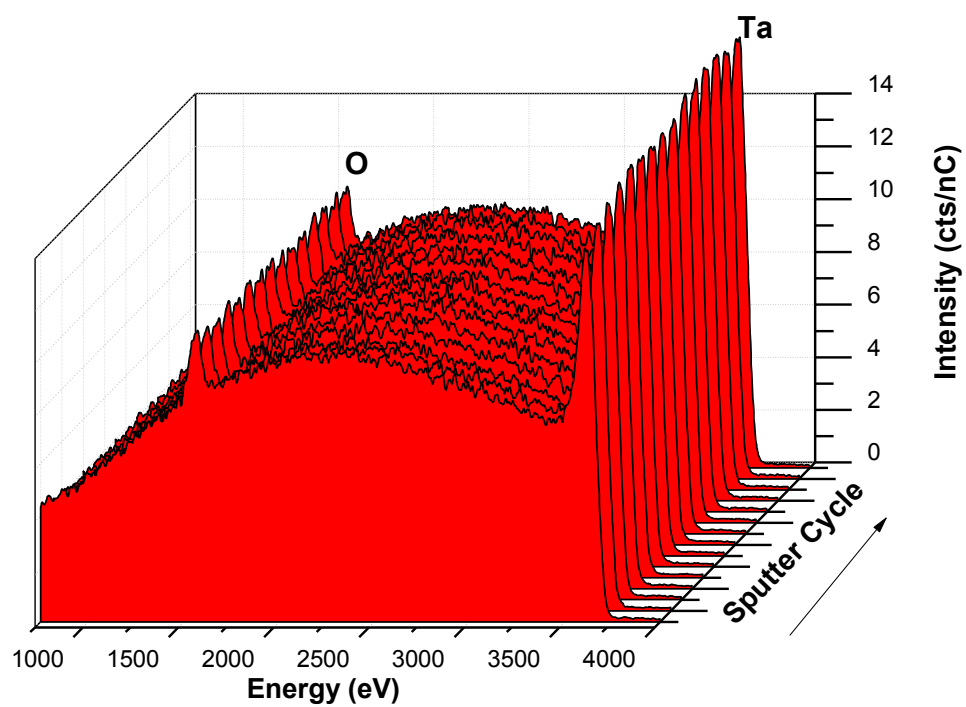


Figure 5.2: HS-LEIS Depth Profile of the Bulk TaON Photocatalyst.

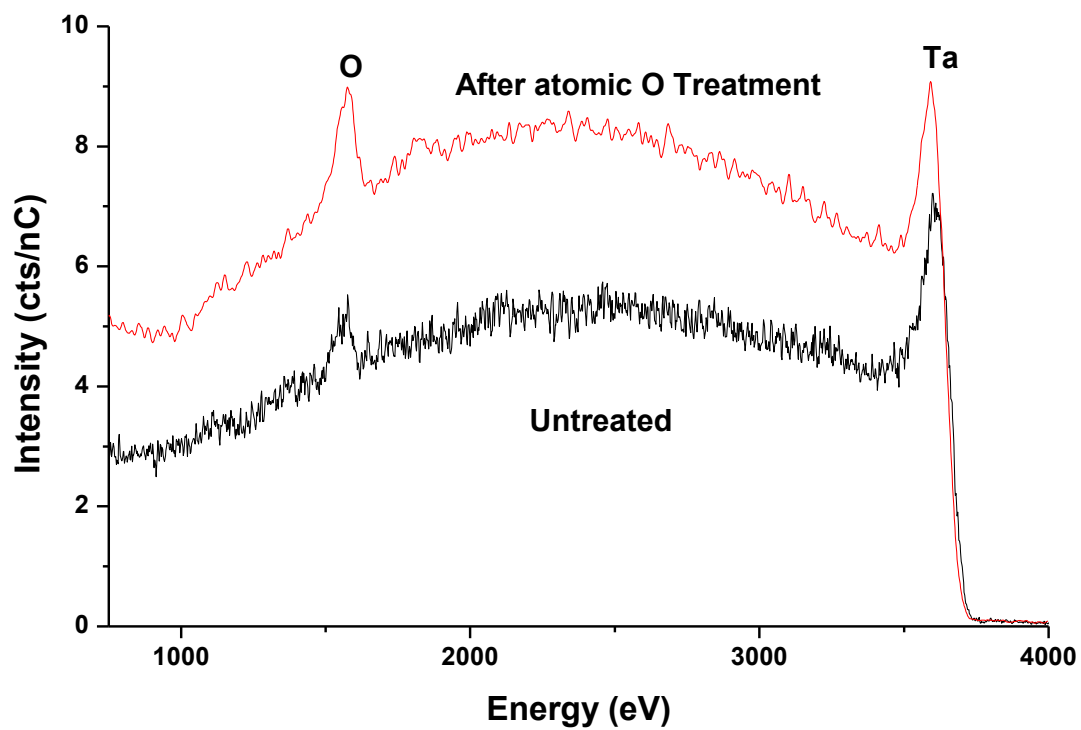


Figure 5.3: HS-LEIS spectra of Bulk TaON Photocatalyst Before and After Atomic O Pretreatment.

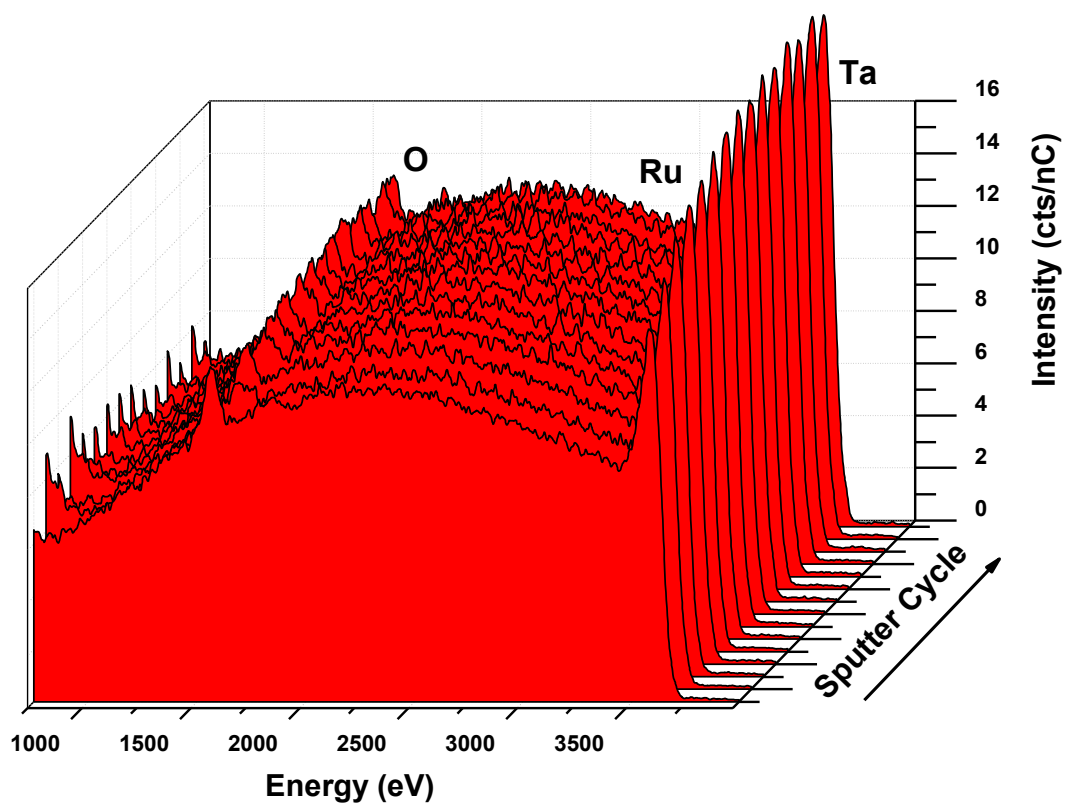


Figure 5.4: HS-LEIS Depth Profile of the Supported RuO₂/TaON Photocatalyst.

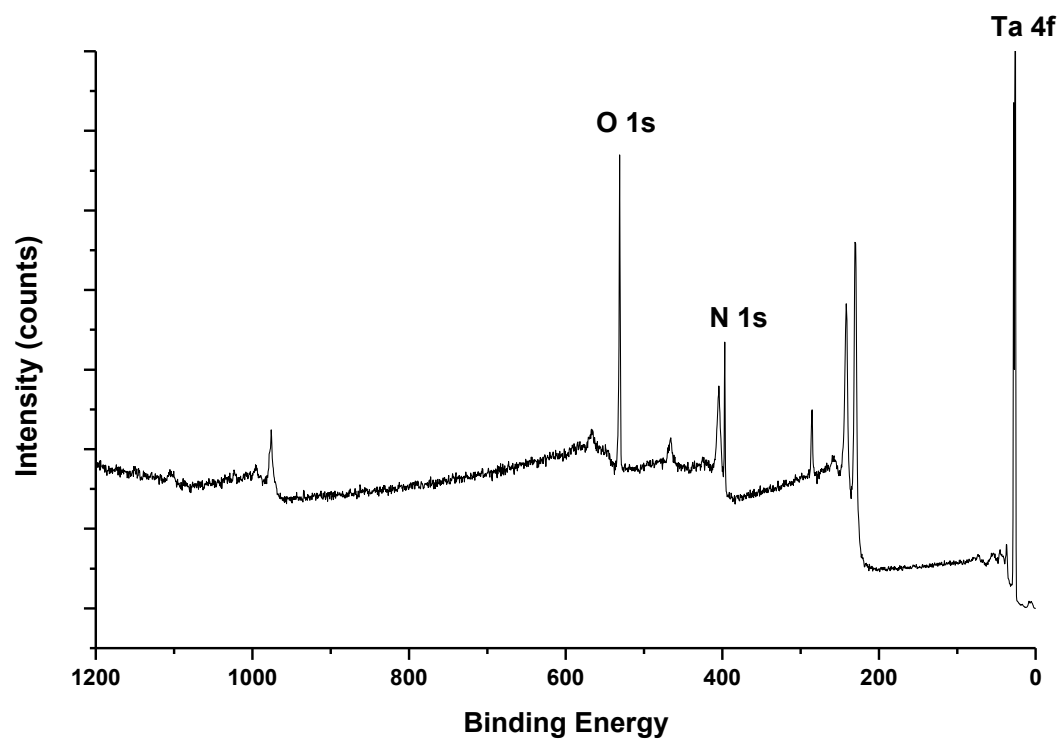


Figure 5.5: XPS Survey Spectra of Bulk TaON.

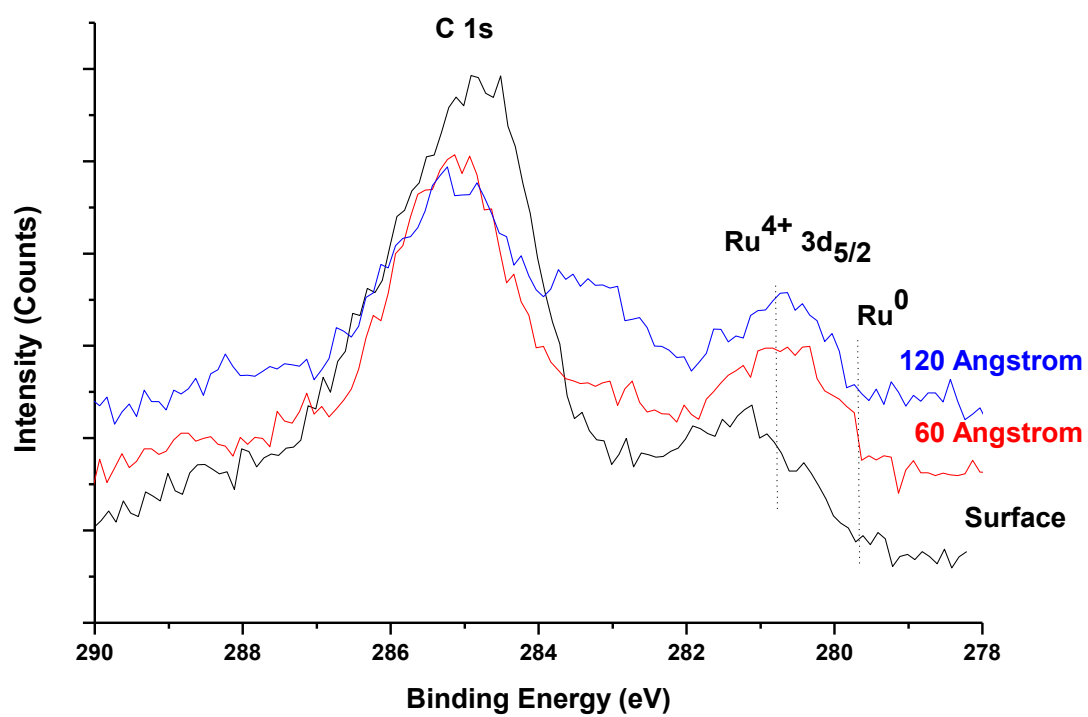


Figure 5.6: HR-XPS surface analysis of Rh 3d region for supported 0.5% RuO₂/TaON photocatalysts.

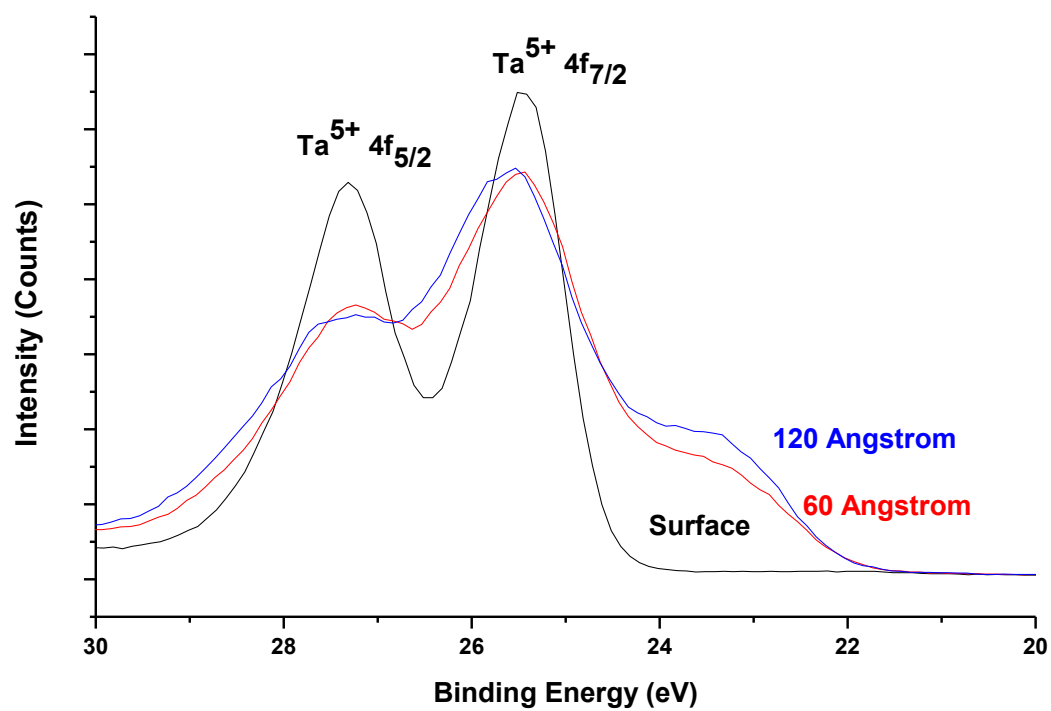


Figure 5.7: HR-XPS surface analysis of Ta 4f region for supported 0.5% RuO₂/TaON photocatalysts.

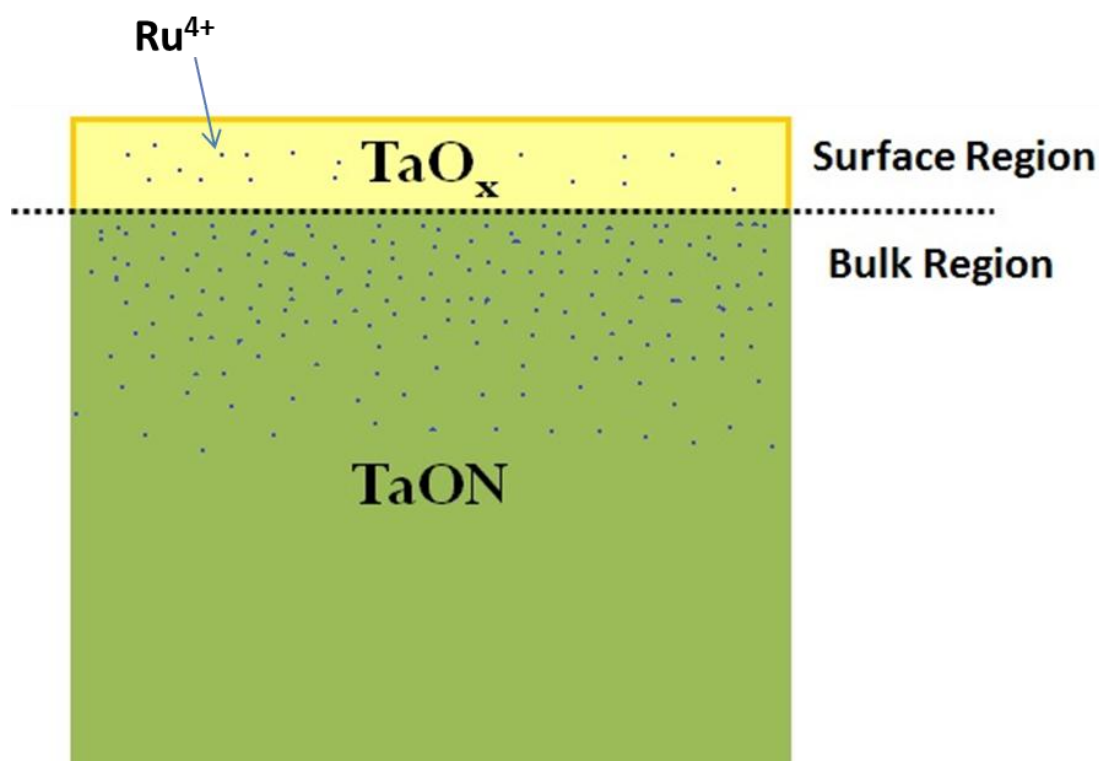


Figure 5.8: Schematic Model for the Surface Region of the Supported 0.5% RuO_2/TaON photocatalyst.

CHAPTER 6

Conclusions and Future Studies

6.1 Conclusions

Much progress has been achieved over the past 40 years in discovering advanced materials that are capable of photocatalytic water splitting. Unfortunately, the progress in the fundamental scientific understanding of these advanced photocatalytic materials has significantly lagged. One of the major issues with previous studies of the semiconductor photocatalysts has been the focus on utilizing bulk characterization techniques and attempting to correlate photocatalyst bulk structural properties with the corresponding photoactivity. Photocatalysis is a process that involves both bulk (electron/hole generation), diffusion of the electrons/holes to the surface and reaction of H_2O with excited electrons and holes at the surface to produce H_2 and O_2 . Although bulk characterization techniques effectively elucidate bulk molecular and electronic structures of complex semiconductor photocatalytic systems, the catalytic reactions between the electrons/holes and water take place on the outermost surface layer and further progress in photocatalysis will come from surface characterization studies that will provide new insights. Only by correlating surface properties with photoactivity can realistic photocatalytic models be developed. The fundamental

bulk/surface structure–photoactivity relationships for a few of the more interesting photocatalyst systems were investigated in this dissertation and the main conclusions for each chapter are summarized below.

Chapter 2

The most active photocatalyst under UV irradiation (0.2%NiO/NaTaO₃:2%La) was studied in this chapter to determine the effect of the La₂O₃ and NiO species on photoactivity. The addition of both La₂O₃ and NiO did not cause any change in the bulk molecular and electronic structure of the NaTaO₃. HR-XPS and HS-LEIS spectroscopy revealed that the NiO and La₂O₃ promoters are surface segregated on the bulk NaTaO₃ phase. La₂O₃ was found to be a surface structural promoter, stabilizing the NaTaO₃ particles and increases the surface area by a factor ~10. The specific photoactivity was found not to be enhanced by the La₂O₃. NiO was found to act as efficient electron traps preventing electron/hole recombination in the bulk and helping to facilitate surface migration for photocatalysis. This leads to the enhancement of photoactivity by a factor of 10¹-10² in the presence or absence of the La₂O₃ promoter. These new findings brings into question the validity of the previously accepted model for the NiO/NaTaO₃:La photocatalyst where a synergistic interaction of NiO preferentially self-assembling at nanostep structures created by the doped La₂O₃ was responsible for the enhanced photoactivity. The importance of normalizing photocatalytic activity by unit surface area was emphasized as well since the accepted practice of normalizing by unit mass is not fundamentally meaningful.

Chapter 3

The fundamental bulk/surface structure – photoactivity relationship was investigated on bulk GaN and supported (Rh_{2-y}Cr_yO₃)/GaN photocatalysts. Raman and UV-vis spectroscopy was able to show that the bulk structure of the GaN phase was not perturbed by the (Rh_{2-y}Cr_yO₃) NPs. The surface of the GaN phase was found to be altered in the surface region: GaN → GaO_xN_y → GaO_x. The (Rh_{2-y}Cr_yO₃) NPs were found to consist of Rh³⁺ and Cr³⁺ species both found on the outermost surface layer. The addition of (Rh_{2-y}Cr_yO₃) assisted in the transfer of photoexcited electrons to the surface promoting the photocatalytic surface reaction. Thus, it was determined that Rh³⁺ is responsible for enhanced H₂ and Cr³⁺, GaO_x or at their contact points are the possible sites for O₂ production.

Chapter 4

Two different methods for the preparation of Rh-Cr NPs on (Ga_{1-x}Zn_x)(N_{1-x}O_x) were compared to determine surface/photoactivity relationships. (Rh_{2-y}Cr_yO₃) NPs on (Ga_{1-x}Zn_x)(N_{1-x}O_x) were found to consist of Rh⁺³ surface active sites for the generation of H₂ with Cr⁺³, GaZnO_x or at their contact points as the possible surface active sites for the generation of O₂ similar to (Rh_{2-y}Cr_yO₃) NPs on GaN. Rh⁺³ and Cr⁺³ were also found to be the dominant surface species for the (Rh/Cr₂O₃)/(Ga_{1-x}Zn_x)(N_{1-x}O_x) with trace amounts of Rh⁰ on the surface. The presence of the exposed metallic Rh⁰, which catalyzes the back reaction, was found to be responsible for the ~50% less H₂/O₂ production for the (Rh/Cr₂O₃)/(Ga_{1-x}Zn_x)(N_{1-x}O_x). PL spectroscopy was also able to show that the Rh-Cr NPs affected the recombination of electron/holes in the bulk

(Ga_{1-x}Zn_x)(N_{1-x}O_x) by increasing the lifetime of excited electrons and the population of these long lived electrons so they can be collected at the surface and harnessed for photocatalytic water splitting. These new insights were used to propose new modified models for the photocatalyst systems.

Chapter 5

The surface nature of bulk TaON and RuO₂/TaON photocatalysts was the focus of investigation for this chapter. The bulk molecular and electronic structure was found to not be perturbed by the addition of RuO₂. Analysis of the outermost surface layer revealed only the presence of TaO_x. Depth profiling with HR-XPS was able to show that concentration of Ru⁴⁺ increased with sputtering showing that most of the Ru⁴⁺ was diffusing into the bulk and were not surface enriched. The presence of the dissolved Ru⁴⁺ in the bulk was proposed to be responsible for enhanced activity for the RuO₂/TaON photocatalysts. A new model was then developed for the RuO₂/TaON photocatalyst from the surface analysis.

6.2 Future Studies

In the past, the lack of utilizing surface characterization techniques has led to proposed photocatalytic models based on bulk structure that has hindered the progress in development of fundamental photocatalytic models that can guide the design of advanced photocatalytic materials. The hypothesis of this research proposal is that only when bulk and surface characterization techniques are combined can fundamental structure-photoactivity relationships be established for complex, multicomponent

photocatalysts. The methodology for determining fundamental structure-photoactivity relationships in this dissertation can thus be applied to other photocatalyst systems to help in the scientific understanding of how photocatalyst function. The insights gained can then be applied in designing more efficient photocatalyst systems. For example, the conclusions from this study show that the synthesis of $(\text{Rh}/\text{Cr}_2\text{O}_3)/(\text{Ga}_{1-x}\text{Zn}_x)(\text{N}_{1-x}\text{O}_x)$ can be improved by the modification of the GaZnO_x surface by adding metal oxide dopants/other known metal oxide active sites and by exchange Cr_2O_3 with other transition metal promoters.

Critical surface information can be obtained with HS-LEIS and HR-XPS characterization that are able to determine the atomic composition and chemical state of the surface of the photocatalysts, however the signal from these characterization techniques are averaged over a large raster size. The elements present on the surface are able to be quantified but these techniques do not give information on how the elements are distributed on the surface. Additional information about the distribution of the various elements in the complex photocatalysts can come from electron microscopy with the use of STEM-EELS and STEM-HAADF that is able to provide atomic resolution.

The main drawback to HS-LEIS and HR-XPS, as well as electron microscopy, is that these characterization techniques require the measurements to be performed in ultrahigh vacuum and, thus, are unable to operate during photocatalysis with condensed water. The application of *in situ* ATR-IR and transient ATR-IR spectroscopy allows analysis of photocatalysts at the solid/liquid interphase during

photocatalysis with condensed water as long as the photocatalyst possesses a high surface area (number of surface sites). ATR-IR spectroscopy can provide information about aqueously dissolved and adsorbed reactants and products, adsorbed intermediates, byproducts, and spectators. Such fundamental studies can help to determine the most abundant reactive intermediate on the surface and identify the rate-determining-step for the photocatalytic process. This will provide the much needed surface kinetics of the different bond making and bond breaking chemical steps and their sequence under the photocatalytic process. The low surface area for most promising photocatalyst systems, however, will make it quite challenging to obtain measurable signals. If such measurements become successful in the future, then the knowledge gained will significantly assist in advancing the scientific foundation for the photocatalytic water splitting surface reactions. Such fundamental information about the mechanism for water splitting is severely lacking in the literature and only such experiments will help to clarify the photocatalysis process by semiconductor materials.

Photocatalytic water splitting is still a developing technology and the science behind the photocatalytic process is still not fully understood. A little over 10 years ago, photocatalytic water splitting with the use of visible light was still considered to be a “dream reaction”. The advances made in the past decade have demonstrated that there are several photocatalyst systems that are capable for photocatalytic water splitting using visible light. The next challenge is to increase the efficiency of these visibly activated photocatalyst systems so that the process can become commercially

viable. An efficient photocatalysis process has the potential to help address global energy and environmental problems, and be the ultimate source of sustainable green energy. Establishing this fundamental foundation is critical for the rational design of future photocatalyst systems.

VITAE

Education

Ph.D., Chemical Engineering, Lehigh University 2006-2013

Dissertation Title: *Fundamental Characterization Studies of Advanced Photocatalytic Materials*

Advisor: Israel E. Wachs

B.S., Chemical Engineering, Lehigh University 2002-2006

Research Experience

Research Assistant, Lehigh University 2006-2013

- Synthesized and characterized supported Pt/ZrO₂/SiO₂ and WO₃/ZrO₂/SiO₂ by controlling ZrO₂ nano-domain size for methanol oxidation reactions.
- Synthesized and characterized supported TiO₂/SiO₂, MO_x/TiO₂/SiO₂, and Ta₂O₅/SiO₂ for photocatalytic water splitting reactions.
- Surface characterized UV-light activated bulk mixed Tantalum photocatalysts to determine the nature of the catalytic active sites.
- Collaborated with a research group at the University of Tokyo for surface characterization and improved catalyst design of visible light activated bulk mixed oxide photocatalysts.
- Teaching Assistant for Chemical Engineering Lab I, Chemical Equilibria in Aqueous Systems and Transport Processes (graduate-level).

Undergraduate Student Researcher, Lehigh University 2005-2006

- Opportunity for Student Innovation Program on examining small-scale fluids systems.
- Designed mm-scale fluid systems using PDMS polymer utilizing electro-osmosis for fluid flow.
- Velocity profiles and pressure drop properties were examined to compare electro-osmosis and pressure driven flow for running small-scale chemical reactions.

Research Intern, Mallinckrodt Baker, Phillipsburg, NJ Summer 2005

- Worked in clean room environment to develop sample preparation methods for reduced analysis time of contaminants in acids and organic solvents.

- Developed experimental protocol for microwave evaporation for trace metal analysis.
- Performed trace metal analysis of acids and organic solvents for contamination using ICP-OES and ICP-MS.

Student Researcher, South Dakota School of Mines and Technology,
Rapid City, SD Summer 2003

- Research Experience for Undergraduates on pretreatment of biomass for enhanced ethanol production.
- Processed the breakdown of lignocellulosic materials into fermentable sugars for ethanol production.
- Ran simultaneous saccharification and fermentation reactions in flask batch reactor analyzing product composition with HPLC.

Professional Affiliations

Tau Beta Pi Engineering Honors Society, American Institute of Chemical Engineers, American Chemical Society, Catalysis Club of Philadelphia, and New York Catalysis Society

Publications

“Determination of a Structure-Photocatalytic Relationship for Water Splitting on Well-Defined TiO₂ Nanodomains,” C.A. Roberts, A.A. Puretzky, S.P. Phivilay and I.E. Wachs (in preparation).

“Influence of Oxide Support Domain Size on the Characteristics of Supported Metal and Metal Oxide Nanophases,” S.P. Phivilay, W. Zhou, E.I. Ross-Medgaarden, C.J. Kiely, and I.E. Wachs (in preparation).

Selected Presentations

“Design and Characterization of Photocatalysts for Solar Powered Hydrogen Generation,” S.P. Phivilay, C.A. Roberts, A. Puretzky, A. Xiong, J. Kubota, K. Maeda, K. Domen and I.E. Wachs, Lehigh University Chemical Engineering Student Seminar, Bethlehem, PA (March 30, 2012).

“Fundamental Surface Structure-Photoactivity Relationships of Tantalum-based Photocatalysts,” S.P. Phivilay, X. Yang, G.F. Liu, B. Koel, and I.E. Wachs, The 22nd NAM Meeting, Detroit, MI (June 6, 2011).

“Fundamental Surface Structure-Photoactivity Relationships of Advanced Photocatalysts,” S.P. Phivilay, C.A. Roberts, X. Yang, G.F. Liu, B. Koel, and I.E. Wachs, The 241th ACS National Meeting, Anaheim, CA (March 30, 2011).

“Fundamental Surface Structure-Photoactivity Relationships of Advanced Photocatalysts,” S.P. Phivilay, C.A. Roberts, and I.E. Wachs, Gordon Research Conference student poster competition, New London, NH (June 27 - July 2, 2010).

“Fundamental Surface Structure-Photoactivity Relationships of Advanced Photocatalysts,” S.P. Phivilay, C.A. Roberts, and I.E. Wachs, The 239th ACS Annual meeting, San Francisco, CA (March 21-24, 2010).

“The Structure-Photocatalytic Activity Relationships of $\text{TiO}_2/\text{SiO}_2$ Nanocatalysts”, S.P. Phivilay and I.E. Wachs, Catalysis Club of Philadelphia student poster competition, Claymont, DE (March 19, 2009).

“The Structure-Photocatalytic Activity Relationships of $\text{TiO}_2/\text{SiO}_2$ Nanocatalysts”, S.P. Phivilay and I.E. Wachs, Spring Symposium of the Catalysis Society of Metropolitan New York student poster competition, Princeton, NJ (March 18, 2009).

“Influence of ZrO_2 Nanoligands on the Catalytic Performance of Supported $\text{Pt}/\text{ZrO}_2/\text{SiO}_2$ Catalysts”, S.P. Phivilay, W. Zhou, C. Kiely, and I.E. Wachs, AIChE Annual Meeting, Philadelphia, PA (Nov 16-21, 2008).